

# Developments in Photoacoustic-Ultrasound Tomography

by

Quinn Barber

A thesis submitted in partial fulfillment of the requirements for the  
degree of

Master of Science  
in  
Biomedical Engineering

Department of Electrical and Computer Engineering  
University of Alberta

© Quinn Barber, 2017

# Abstract

For cancer research, a powerful imaging modality for both preclinical (where the focus is on imaging small animals) and clinical (where the focus is on imaging human subjects) applications should be inexpensive, portable, non-invasive, safe, and capable of measuring a myriad of information. Furthermore, scalability between small and large subjects will allow this modality to be easily utilized for both preclinical and clinical applications. An emerging multimodality system that fits these criteria is photoacoustic-ultrasound tomography. Ultrasound tomography where ultrasound waves are transmitted through a target and then received can provide not only morphological image, but due to its geometry, it can also provide quantitative information such as acoustic speed-of-sound and attenuation within a target. Photoacoustic tomography where short light pulses are used to produce ultrasound signal - can provide other quantitative information based on optical parameters, such as optical absorption, and is capable of molecular imaging. Both modalities are easily scalable, non-invasive, portable, and use nonionizing radiation. Combining these two modalities may provide a powerful medical imaging system for both preclinical and clinical applications. This thesis focuses on the development of this type of system. The first focus of this

thesis is to improve the scalability of photoacoustic tomography by implementing a novel illumination technique, where a small-area illumination is scanned across a large-area target. This is in replacement of the conventional method of illumination the whole large-area target at once. By scanning a small-area illumination beam, the signal-to-noise ratio (SNR) of any photoacoustic tomography system can be maximized, regardless of the illumination power used. The second focus is on improving SNR for ultrasound tomography without reducing its high-resolution capabilities. Ultrasound tomography techniques are inherently low-SNR, and the techniques to mitigate this problem tend to rely on sacrificing resolution, or necessitating an enormous amount of data to be collected. Our technique avoids both adverse effects, providing images with high SNR and high resolution for any amount of data collected. The final focus of this thesis is to develop novel reconstruction techniques to measure and visualize ultrasound scattering anisotropy. Scattering anisotropy where the scattered signal intensity is dependent on angular direction is caused by many different scatterer parameters, such as the geometry of the scatterer, and its material composition. The first novel reconstruction technique involves measuring the direction of fibre-like scattering objects. These objects will produce high scattering intensities orthogonal to their direction, and low scattering intensities parallel to their direction. By measuring signal intensities from many angles around the target (of which ultrasound tomography is uniquely capable), the direction of the fibre-like structures can be estimated and visualized. Applications of this visualization may be for fibre-orientation imaging, or to measure extracellular matrix reorganization caused by malignant tumours in breast

cancer. The second novel reconstruction technique exploits the fact that the level of anisotropy for spherical scatterers depends on their compressibility and density. Compressibility will produce isotropic, monopole scattering whereas density will produce anisotropic, dipole scattering. The novel reconstruction technique utilizes this difference and can produce compressibility- and density-weighted images, able to differentiate highly compressible targets from highly dense targets. These types of images may be impactful for breast cancer diagnosis with respect to imaging breast microcalcifications small calcium deposits in breast tissue that are used to detect early signs of breast cancer. Ultimately, by improving the scalability and effectiveness for photoacoustic and ultrasound tomography, and by introducing new quantitative parameters that can be imaged by ultrasound tomography, this thesis hopes to improve the strength and capacity of photoacoustic-ultrasound tomography systems for medical imaging for cancer research.

# Preface

This thesis is an original work by Quinn M. Barber.

Some work in this thesis derives for collaboration with some lab members working under Dr. Zemp. Chapters 1, 2, and 7 are original work done by Quinn M. Barber.

Chapter 3 has been published as: Barber, Quinn, Tyler Harrison, and Roger J. Zemp. "Blanket illumination vs scanned-mosaicking imaging schemes for wide-area photoacoustic tomography." SPIE BiOS. International Society for Optics and Photonics, 2015. Tyler Harrison helped develop initial reconstruction techniques and modifications to scripts necessary for data gathering through the Verasonics acquisition system used. I was responsible for running simulations, developing reconstruction algorithms, system schematic development, data collection, and manuscript writing. Roger J. Zemp was the supervisory author involved with conceptional development and manuscript preparation.

Chapter 4 has been published as: Barber, Quinn, and Roger J. Zemp. "Ultrasound Scattering Anisotropy Visualization with Ultrasound Tomography." IEEE Transactions on Ultrasonics, Ferroelectrics, and Frequency Control (2016). I was responsible for developing reconstruction techniques, experimental data collection, and writing the manuscript. Roger J. Zemp was the supervisory author involved with conceptional development and manuscript preparation.

Chapter 5 has been published as: Barber, Quinn, and Roger J. Zemp. "S-sequence enhanced synthetic aperture ultrasound scattering tomography." Ultrasonics Symposium (IUS), 2016 IEEE International. IEEE, 2016.

I was responsible for developing reconstruction techniques, experimental data collection, and writing the manuscript. Roger J. Zemp was the supervisory author involved with conceptual development and manuscript preparation.

Chapter 6 contains work that has been recently submitted for publishing. I was responsible for developing reconstruction techniques, experimental data techniques, and writing the manuscript. Roger J. Zemp was the supervisory author involved with conceptual development and manuscript preparation.

# Acknowledgments

I gratefully acknowledge the funding support of the Natural Sciences and Engineering Research Council of Canada, the Canadian Institutes of Health Research, the Canadian Cancer Society, the Government of Alberta, and the University of Alberta.

I would also like to thank my supervisor, Dr. Roger Zemp, and my colleagues that helped with my research in both personal and professional ways (listed in no particular order): Tyler Harrison, Robert Paproski, Wei Shi, Tarek Kaddoura, Ben Greenlay, Ryan Chee, Min Choi, Kevan Bell, Kibria Chowdhury, David Egolf, Chris Ceroci, Mohammed Maadi, Afshin Kashani, Parsin Hajireza, Pradyumna Kedarisetti, Henry Brausen, John Wood, Erick Ochoa, Erika Lloyd, Dillon St. Jean, Eric Den Haan, Laura Hocevar, Adriana Hernandez.

Furthermore, I would like to thank my supervisory committee and the staff from Electrical and Computer Engineering and the Faculty of Graduate Studies and Research for the support in completing my studies.

Finally, I would like to thank my family and friends, for whose love and support I am forever grateful.

# Contents

<b>Abstract</b>	<b>ii</b>
<b>Preface</b>	<b>v</b>
<b>Acknowledgments</b>	<b>vii</b>
<b>List of Symbols</b>	<b>xvi</b>
<b>Glossary of Terms</b>	<b>xviii</b>
<b>1 Introduction</b>	<b>1</b>
1.1 Motivation . . . . .	1
1.2 Key Contributions . . . . .	3
1.3 Layout of Thesis . . . . .	5
<b>2 Background</b>	<b>6</b>
2.1 Ultrasound Imaging . . . . .	6
2.2 Photoacoustic Imaging . . . . .	8
2.2.1 The photoacoustic effect . . . . .	8
2.2.2 Photoacoustic Imaging: Microscopy and Tomography	10
2.3 Ultrasound Tomography . . . . .	16
2.3.1 Reflection-based Ultrasound Tomography . . . . .	17
2.3.2 Transmission-based Ultrasound Tomography . . . . .	20
2.4 Ultrasound Anisotropy . . . . .	27

<b>3</b>	<b>Blanket Illumination vs Scanned-Mosaicking Imaging Schemes for Wide-Area Photoacoustic Tomography</b>	<b>30</b>
3.1	Introduction . . . . .	30
3.2	Theory . . . . .	32
3.3	Simulations . . . . .	33
3.4	Experimental Results . . . . .	35
	3.4.1 Methods and Materials . . . . .	35
	3.4.2 Experimental Results . . . . .	36
3.5	Conclusion . . . . .	37
<b>4</b>	<b>S-sequence Enhanced Synthetic Aperture Ultrasound Scattering Tomography</b>	<b>39</b>
4.1	Introduction . . . . .	39
4.2	Theory: S-Sequence Encoding . . . . .	41
4.3	Methods and Materials . . . . .	43
4.4	Results . . . . .	45
	4.4.1 Resolution . . . . .	45
	4.4.2 SNR improvement . . . . .	47
	4.4.3 PAUS Composite Imaging . . . . .	50
4.5	Conclusion . . . . .	50
<b>5</b>	<b>Ultrasound Scattering Anisotropy Visualization with Ultrasound Tomography</b>	<b>52</b>
5.1	Introduction . . . . .	52
5.2	Methods and Materials . . . . .	55
5.3	Results . . . . .	57
	5.3.1 Resolution . . . . .	57
	5.3.2 Anisotropy Visualization . . . . .	59
5.4	Conclusion . . . . .	61
<b>6</b>	<b>Compressibility and Density Weighting for Ultrasound Tomography Imaging</b>	<b>63</b>
6.1	Introduction . . . . .	63
6.2	Theory . . . . .	65

6.2.1	Compressibility and Density Decoupling . . . . .	65
6.2.2	Numerical Integration . . . . .	69
6.2.3	Limited-view Consideration . . . . .	70
6.3	Methods and Materials . . . . .	72
6.4	Results . . . . .	73
6.4.1	Simulation . . . . .	73
6.4.2	Resolution . . . . .	76
6.4.3	Wire Experiments . . . . .	77
6.4.4	Phantom Experiments . . . . .	79
6.5	Discussion . . . . .	83
6.6	Conclusion . . . . .	84
<b>7</b>	<b>Conclusion</b>	<b>86</b>
	<b>Bibliography</b>	<b>90</b>

# List of Tables

3.1	Imasonic Ring Transducer specifications . . . . .	35
4.1	CNR of red kernels in Fig. 4.4 . . . . .	49
5.1	FWHM in $\mu m$ of Wires in Fig. 5.2 . . . . .	59
5.2	ROI Calculations for Fig. 5.5 . . . . .	60
6.1	Contrast values for Wire Experiments, see Equation 6.22 . . .	78
6.2	Contrast values for scattering phantom, see Equation 6.22 . .	82
6.3	CSR values for scattering phantom, see Equation 6.23 . . . .	82
6.4	Normalized contrast values for scattering phantom, see Equation 6.24 . . . . .	83

# List of Figures

2.1	Melanoma growth monitoring in <i>in vivo</i> mouse ear. Adapted by permission from Macmillan Publishers Ltd: Nature Protocols [140], copyright 2010. . . . .	12
2.2	a) Photoacoustic Tomography slices of a mouse <i>in vivo</i> . b,c,d include abdominal, thoracic, and head cross-sections respectively with <i>ex vivo</i> images for comparison. Reprint with permission from [100]. . . . .	14
2.3	Schematic of ring-array transducer. . . . .	18
2.4	A reflection-mode, sound-speed, attenuation, and fusion-mode image of a breast from Duric <i>et al.</i> using ray-based reconstruction. Fusion image consists of a composite of all three images. Reprint with permission from [24] . . . . .	21
2.5	A comparison of two sound speed reconstruction algorithms in simulations. (A) true model, (b) waveform tomography, (c) ray-based, (d) b-a residual image. Reprint with permission from [70] . . . . .	25
3.1	Comparing the diffused laser beam technique (left) with the scanned-mosaicked beam technique (right) for a ring transducer.	31
3.2	Fluence distribution for pencil beam with radii 0.01 cm (left), 0.5 cm (centre), and 2.5 (right). . . . .	33

3.3	Monte-Carlo results for signal gain measured as a ratio between a small spot size vs a large spot size (2.5 cm radius). Values were measured at the edge of the small spot radius (left) and at the centre of both spot radii (right) at different depths. The dashed line denotes when the gain of the small spot size is larger than that of the large spot size . . . . .	34
3.4	Schematic of experiment. . . . .	35
3.5	Image of transducer in use. . . . .	36
3.6	Hair phantom images with a diffuse beam (left) and SM beam (right). . . . .	37
3.7	SNR comparison for diffused and SM beam at two depths. . .	38
3.8	SNR for diffused beam with respect to the amount of averaging. This is compared to the unaveraged SM beam. . . . .	38
4.1	Schematic of UST and PAT system. . . . .	41
4.2	FWHM's of STA- and S-Sequence wire targets from both UST and B-Mode Linear Imaging. Scale bar is equal to 0.5 mm. .	46
4.3	PAT resolution cross-sections with their respective point spread functions. Scale bar is equal to 0.25 mm . . . . .	47
4.4	Noise kernels (blue) and CNR kernels (red) used for SNR and CNR calculation for wire experiment (left) and phantom experiment (right). Scale bar is equal to 5mm (left) and 10mm (right). . . . .	48
4.5	STA-UST (left) and S-Sequence UST (right) on wire targets, with a dynamic range of 50 dB for both images. Scale bar equal to 5 mm . . . . .	48
4.6	Ultrasound Tomographic images of wire phantom using (left) STA reconstruction and (right) S-Sequence reconstruction with a dynamic range of 50 dB for both images. Scale bar is equal to 5mm. . . . .	49

4.7	Ultrasound (left), photoacoustic (right), and photoacoustic/ultrasound (centre) composite tomographic images of hair phantom. Red colormap signifies photoacoustic data and greyscale colormap signifies ultrasound data. Scale bar equal to 5 mm. . . . .	50
5.1	(Left) A plot of intensity with respect to transmit angle for a pixel in the iron filing experiment described below, seen in Fig 5.5. (Right) Images of the aforementioned pixel at two angles with a $90^\circ$ difference. Length bars are 0.5 mm long. . .	57
5.2	Wire Placements within the Ring Transducer for Resolution Measurement. . . . .	58
5.3	UST VS Synthetic Aperture Backscatter Image with a linear transducer. Scale bars are equal to 0.5 mm in length. . . . .	58
5.4	A) Iron filing phantom encased with a gelatin medium within ring-array transducer. B) UST image of iron filings. Scale bar indicates 1 cm. . . . .	59
5.5	Anisotropy vector field plot image superimposed onto UST image. Scale bar indicates 5 mm. . . . .	60
5.6	Wire target in gelatin, and the UST image corresponding to this target. Scale bar is 1 cm long. Boxed areas on the right image correspond to the zoomed in images in Fig. 5.7. . . . .	61
5.7	Anisotropic visualization of a Copper Wire in Gelatin. Scale bar is equal to length of 1 mm. . . . .	61
6.1	(Left) Schematic of Ring-Array Transducer. (Right) Scattering profiles of compressibility contrasted ultrasound scatterer (top), and density-weighted contrast scatterer (bottom) . . .	65
6.2	Simulation of large compressibility (left) and density scatterer (right) using a limited $256^\circ$ transducer. Compressibility-weighted image is found on top, and density-weighted image is found on the bottom. . . . .	74

6.3	Simulation of large compressibility (left) and density scatterer (right) using a full 360° transducer. Compressibility-weighted image is found on top, and density-weighted image is found on the bottom. . . . .	75
6.4	Simulation of two inclusions with randomly placed compressibility (left) and density (right) scatterers placed within each inclusion. Compressibility-weighted image is found on top, and density-weighted image is found on the bottom. . . . .	76
6.5	Aluminum wire imaged with compressibility-weighting (left) and density weighting (right). Scale bar is 0.5 mm . . . . .	77
6.6	UST image of nylon (left), cotton (centre), and steel (right) wires using both compressibility weighting (top) and density weighting (bottom). Envelope-detection was implemented on A-scans. Scale bar equals 5 mm. . . . .	78
6.7	Experimental set-up with scattering phantom placed within a water bath. . . . .	80
6.8	UST image of nylon (left) and steel (right) wires within a cornstarch scattering medium, with compressibility weighting (top) and density weighting (bottom) performed. Scale bar equals 1 mm. . . . .	81

# List of Symbols

Below is a list of frequently used symbols and their general meaning. This list is incomplete, however can be used as a quick reference for the reader.

- $p_0$ : Pressure
- $\Gamma$ : Grueneisen parameter
- $\Phi$ : Fluence, or energy per area, of light.
- $\mu_a$ : Absorption coefficient
- $\mu'_s$ : Reduced scattering coefficient
- $\beta$ : Thermal coefficient of volume expansion
- $\kappa$ : Isothermal compressibility, defined as the inverse bulk modulus of a material
- $\rho$ : Density
- $C_v$ : Specific heat capacity at constant volume.
- $C_P$ : Specific heat capacity at constant pressure.
- $H$ : The heating function (amount of thermal energy that is converted to heat per unit volume per unit time).
- $c$ : Speed of sound
- $k$ : Wavenumber

- $\lambda$ : Wavelength
- $\sigma$ : Variance, measured as the standard deviation.
- $\mu$ : Mean
- $\tau$ : Time-delay
- $I$ : Matrix denoting a reconstructed image.

# Glossary of Terms

Below is a collection of frequently used terms that may not be defined every time they are used. This is an incomplete list, however is provided as an aid to the reader.

- Anisotropic scattering: Ultrasound scattering whose signal intensity is dependent on the angle at which the scattering occurs.
- ANSI: the American National Standards Institute, a non-profit organization that oversees the development of safe, standard practices.
- Aperture encoding: In ultrasound imaging, this denotes choosing a specific collection of ultrasound elements in a transducer array to transmit at one time.
- A-scan: The signal from a single ultrasound transducer element as a function of time.
- Chromophore: An atom or group of atoms whose presence is responsible for the colour of a compound.
- CT: Computed Tomography, a tomographic imaging modality based on measuring transmitted x-rays.
- CNR: Contrast-to-Noise Ratio, a metric to evaluate the quality of an image.
- DAS: Delay-and-sum, an ultrasound image reconstruction technique.
- Fluence: The energy per unit area of an imaging beam.

- FWHM: Full-width Half-maximum, a calculation that can be used to measure resolution.
- *in vivo*: From Latin, inside the body.
- Isotropic scattering: Ultrasound scattering whose signal intensity is independent on the angle at which the scattering occurs.
- Microcalcification: Small calcium deposits that form in breast tissue.
- MPE: Maximum permissible exposure of light before tissue damage.
- MRI: Magnetic Resonance Imaging
- Multimodality: Exhibiting more than one modality (or type of imaging ability) for an imaging system.
- NIR: Near-infrared light, with wavelength from around 700 nm to 2500 nm.
- Nd:Yag laser: Neodymium-doped yttrium aluminum garnet crystal-based solid-state laser that can produce high-powered single-wavelength laser light.
- OPO: Optical parametric oscillator, laser equipment that allows one to tune (or vary) the wavelength of a laser beam.
- PAM: Photoacoustic microscopy, a photoacoustic imaging technique based off of a tightly-focused light beam.
- PAT: Photoacoustic tomography, a photoacoustic imaging technique based off of tomographic reconstructions.
- Photoacoustic Imaging: An imaging modality based-off of the photoacoustic effect, where light absorption creates propagating acoustic waves.
- Resolution: An value defined by the smallest distance between two objects that can be distinguished in a certain image.

- SM: Scanned mosaic, a technique that scans a small laser spot across an object.
- SNR: Signal-to-noise ratio, a metric to evaluate the clearness of an image.
- TOF: Time-of-flight: How long it takes for a particle to travel from one place to another.
- Tomography: An imaging system that creates 2D image 'slices' - usually involves circular detector geometries. Examples are CT and MRI.
- Transport mean free path: The average path length of a photon before it interacts (i.e., scatters or is absorbed) with something.
- Ultrasound array: An ultrasound transducer made up of more than one ultrasound element.
- Ultrasound element: A single piezoelectric or capacitive device capable of measuring pressure changes due to acoustic waves.
- Ultrasound imaging: An imaging modality based-off of transmitting acoustic waves and measuring the reflection of these waves to create images.
- Ultrasound transducer: Ultrasound imaging equipment that can measure pressure changes due to travelling acoustic waves.
- UST: Ultrasound Scattering Tomography.
- Voxel: The smallest possible volume to image (like a pixel in 3D).

# Chapter 1

## Introduction

### 1.1 Motivation

Medical imaging systems for application to cancer research fall into two major categories: preclinical and clinical imaging. Preclinical imaging concerns itself with imaging small animal subjects, such as mice and rats. It can be used for applications such as imaging metastasis, imaging therapy response, imaging cancer phenotypes, imaging blood supply and hypoxia and hyperoxia of the tumour and surrounding vasculature, as well as measuring metabolism and determining particular gene expression profiles [17,40,66,95]. The focus of clinical cancer imaging is generally of two parts: screening for early detection, and monitoring the efficacy of treatments. Powerful imaging system for both preclinical and clinical imaging should provide structural information, for example density measurements, oxygen saturation in hemoglobin, and vasculature mapping, as well as functional information, for example quantitative measurements of biomarkers and ability to phenotype tumours [17, 19, 40, 66, 89, 95]. Furthermore, developing an imaging system that is easily scalable would provide one system capable of both preclinical and clinical applications.

One important clinical imaging application is for breast cancer detection, diagnosis, and monitoring. Breast cancer is the most common cancer for women in the world, with more than 400 000 patients dying worldwide

per year [28]. Conventionally, breast cancer imaging is achieved through x-ray mammography. This modality, however, uses ionizing radiation, that may increase the risk of cancer for those regularly scanned [21]. It is also limited in the information it produces, only producing a density map of the breast. Furthermore, mammography has difficulty imaging highly dense breast tissue causing false-negatives in diagnosis [114], such as those in premenopausal women. Ultrasound imaging has served as an adjunct to this modality [63,126]. Ultrasound is fast, cheap, portable, and non-ionizing. Conventional ultrasound, however, is highly user dependent, and produces images with lower spatial resolution than those from x-ray mammography. Microcalcification (small calcium deposits in breast tissue) serve as a sign for early detection of cancer. Their size, shape, and pattern within breast tissue can be used to determine the possibility of precancerous cells within the breast [81,84]. Ultrasound is theoretically able to image these microcalcifications, however they are difficult to differentiate from the background scatter of the tissue [83]. However, research is still being done to allow ultrasound imaging to be used exclusively for microcalcification detection [3,35]. Magnetic Resonance Imaging (MRI) is another promising modality for breast cancer imaging, however MRI is expensive, unable to be portable, and necessitates long scan-times which can be uncomfortable for patients [63,126].

This thesis discusses developments of novel photoacoustic-ultrasound tomography systems. These systems are scalable and multimodality, potentially satisfy the preclinical and clinical needs discussed above. As will be discussed, ultrasound scattering tomography will provide significant resolution enhancements over standard B-mode imaging while permitting deep tissue imaging. Moreover, converse to conventional ultrasound, it is much less dependent on the user. Ultrasound tomography has also been used to provide quantitative information such as speed-of-sound and ultrasound attenuation maps. These have been used to approximate the density of breast lesions: an important variable to measure the malignancy of a tumour [23,69,142]. We will present novel capabilities for visualization of scattering anisotropy, which could prove impactful for microcalcification imaging as well as visualizing extracellular matrix reorganization caused by aggres-

sive tumours, which can be an early sign of malignant tumours, and can cause resistances to certain cancer treatments [75, 86]. These ultrasound tomography developments are co-developed with photoacoustic tomography capabilities, which may provide missing functional and molecular imaging capability toolsets. For example, photoacoustic tomography is capable of imaging hemoglobin oxygen saturation and neoangiogenesis, crucial parameters for predicting the aggressiveness of tumour growth [61]. These functional capabilities could also enable early prediction of therapeutic outcomes and individualized treatment plans. Coupled with targeted contrast agents, photoacoustic tomography has the potential for discriminating molecular biomarkers, useful for estimating risk of cancer growth, screening, determining prognoses, and monitoring individualized therapies. [41, 88, 124]. At the preclinical stage, the molecular and functional capabilities of photoacoustic tomography may provide unprecedented multiplexed imaging capabilities for evaluating gene expression patterns with the use of genetically encoded reporters [29, 47, 124].

Preclinical and clinical systems of this nature have already seen commercial development, for photoacoustic tomography [85], and photoacoustic-ultrasound tomography systems [79, 80]. The main goal of this thesis, however, is to contribute to the scalability of photoacoustic systems, the high resolution capabilities of ultrasound tomography, and the unique ability for ultrasound tomographic systems to measure and visualize ultrasound scatter anisotropy. The following section will discuss these key contributions in detail.

## 1.2 Key Contributions

As previously introduced, the main goal of this thesis is to introduce a multimodality photoacoustic-ultrasound tomography system developed. This system consists of a limited-view ultrasound ring array transducer coupled with a Nd:Yag laser capable of producing NIR and visible light. This system can produce both photoacoustic and ultrasound tomographic images concurrently.

The first contribution demonstrates a strategy for scalable photoacoustic imaging over a large area (Chapter 3). Photoacoustic signal is proportional to the fluence (energy per area) of the illumination. For photoacoustic tomography, one conventional approach to illumination is to diffuse a laser pulse over the entire imaging area. The maximum allowable exposure for laser light, set by ANSI [46], permits  $20 \text{ mJ/cm}^2$  for 532 nm light, and around  $100 \text{ mJ/cm}^2$  for near-infrared (NIR) light. Reaching this ANSI limit is important to maximize the available signal-to-noise ratio of the photoacoustic signal. Depending on the photoacoustic set-up used, reaching this ANSI limit may be impossible for large areas. We propose a scanned-mosaic illumination scheme that scans an illumination with a much smaller area across the desired image target. This will allow any laser system to reach the ANSI limit for any size of imaging area producing high signal-to-noise (SNR) images faster than what could be achieved with averaging.

The second contribution is the development of a photoacoustic-ultrasound tomography imaging system. This system is capable of producing composite photoacoustic-ultrasound tomographic images. The ultrasound tomography submodality can produce images with isotropic resolution that matches the half-wavelength diffraction limit of the transducer. The delay-and-sum technique conventionally used for ultrasound tomography reconstruction allows for this high resolution at a cost to SNR. Therefore, we implement a spatial-encoding technique called S-Sequence that improves SNR of the images without degradation of the resolution.

The final contribution of this thesis is to utilize this system to develop novel reconstruction techniques to visualize anisotropic ultrasound reflection and scattering. A scattered signal is defined as anisotropic when the intensity of the signal is dependent on the direction in which it scatters. Anisotropic scattering can be caused by the scatterer's size, shape, and structural composition, specifically its density and compressibility contrast to the surroundings in which it is suspended. As described before, this information may be useful for medical applications [37, 115]. Ultrasound tomographic systems are uniquely capable of measuring this anisotropy for a large span of angles around the imaging target, however utilizing this modal-

ity for anisotropy measurements has only just begun [37]. In this thesis, two novel anisotropy visualization methods are introduced: one that focuses on anisotropy caused by the geometry of the scatterer (Chapter 5), and the other that focuses on anisotropy caused by the density and compressibility components of radially-symmetric scatterers (Chapter 6). Due to the high resolution capabilities of the system introduced, it is capable of accurately visualizing this scatter anisotropy. The two reconstruction methods are introduced, developed, and experimentally validated with phantom imaging experiments.

### **1.3 Layout of Thesis**

This thesis is organized as follows: Chapter 2 will provide background information, providing historical background in photoacoustic and ultrasound tomography and giving context to the research conducted for this thesis. Chapter's 3-5 are borrowed from individual publications [4-6]. Chapter 6 will detail work that is in the process of publication. Finally, Chapter 7 will serve as a conclusion of the work described in this thesis, highlighting future work that can be achieved with the system introduced.

## Chapter 2

# Background

### 2.1 Ultrasound Imaging

Ultrasound imaging has become an indispensable clinical imaging modality due to its comparative low-cost, portability, non-invasiveness and safety. Ultrasound imaging is regularly used to image internal organs like the heart and eyes, to visualize blood flow, to create elastography images, and to help diagnose breast cancer [9, 18, 23]. Furthermore, other non-imaging applications of ultrasound include high-intensity focused ultrasound to deliver heat or agitation to specific parts of the body (for applications such as kidney stone destruction) [26], and penetrating the blood brain barrier to allow higher concentrations of chemotherapy to target brain tumours [44].

Generally, conventional ultrasound imaging involves sending out sound waves at MHz frequencies and receiving the resulting echoes. These echoes are caused by two different physical effects: reflection and scattering [18]. Reflection is caused by a sudden change in acoustic impedance, which is a parameter defined by the material's density and sound speed. This is comprised of information about the structural components of the tissue being imaged. Scattering, on the other hand, is caused by the interaction of our transmitted ultrasound pulse and small ultrasound scatterers within the tissue. The physical properties of this scatterer will determine both the strength of the scattered signal and the anisotropy of this signal (i.e.,

the variable intensity of scattered signal with respect to angular direction around the scatterer).

Ultrasound pulses are transmitted and received by ultrasound transducers, made up of either a single element or an array of piezoelectric or capacitive elements [18]. These arrays come in many shapes: linear arrays, curved array, ring arrays, two dimensional arrays, or bowl-shaped and cylindrical arrays. Different transducers will allow for the capture of unique images. For example, ring shaped arrays allow for a full  $360^\circ$  view, and two dimensional arrays can quickly produce 3D imaging without mechanical scanning. Another way to create different kinds of images is to choose a fitting transmit pulse sequence. For example, ultrasound can be focused to a small focal region within the image, either by utilizing curved arrays, an ultrasound lens, or by delaying transmitted pulses from certain elements so that they all sum constructively at the focus region. Signal in this focal region will have a large intensity, thus increasing the image's signal-to-noise Ratio (SNR). Furthermore, this focal region can be scanned throughout the imaging region to create a 2D or 3D image. For linear arrays, multiple focal points can be transmitted at once, increasing imaging speed while reducing image quality due to interference between focal zones. Multi-element array transducers can also use a transmit sequence called synthetic aperture, where only one element is used to transmit at a time (discussed in depth in section 2.3.1). This reduces the total amount of power, however increases image resolution due to the precise knowledge of where the pulse is transmitted and received. Finally, by using specific transmit sequences and reconstruction techniques, ultrafast ultrasound imaging is possible, capable of imaging at more than ten thousand frames per second, opening up real-time, noninvasive ultrasound applications for functional brain imaging, cardiac electrophysiology, and imaging mechanical properties of tumours [111].

The frequency and length of transmitted ultrasound pulses also affect the quality of images created. Like most wave-based imaging modalities, the frequency of the emitted wave determines the maximum resolution capability of the system. Similar to Abe's diffraction limit in optics [18], an ultrasound system's resolution is limited to half its wavelength, or in other

words, half the ratio between the target’s speed of sound and the centre frequency of the pulse emitted. Ultrasound attenuation, however, is also related to frequency: higher frequencies will attenuate more than lower ones in tissue [18]. Thus, increasing the frequency of the emitted pulse will increase resolution, but at a cost to penetration depth. Pulse length also affects resolution. Specifically, for linear array transducers, axial resolution (resolution with respect to the normal of the transducer’s surface) is related to the transducer’s impulse response [18]. Thus, by reducing the bandwidth of the emitted pulse, axial resolution can be improved. Longer, chirped pulses (similar to those developed for sonar and radar [93]) have recently been utilized, for the longer pulse has more energy per pulse than the shorter, thus increasing the images SNR without having as much of an effect on axial resolution [13]. This, however, relies on more complex reconstruction schemes and system capabilities [13, 93].

With the knowledge of the specific position of elements in the array, along with speed-of-sound estimates, ultrasound images can be reconstructed.

## 2.2 Photoacoustic Imaging

### 2.2.1 The photoacoustic effect

Photoacoustic imaging relies on what is called the photoacoustic effect, first discovered by Alexander Graham Bell in 1880 [8]. When short laser pulses are absorbed by optically absorbing targets, the light is converted to heat, causing a quick thermoelastic expansion. This expansion creates pressure waves that propagate through the imaging target; waves that can be received by the ultrasound array transducers discussed previously.

The strength of an induced photoacoustic signal can be described by the local pressure rise caused by illumination ( $p_0(r)$  at point  $r$ ), which can be described as [7]:

$$p_0(r) = \Gamma(r)\Phi(r, \mu_a, \mu'_s)\mu_a(r) \quad (2.1)$$

where  $\Gamma = \frac{\beta}{\kappa\rho C_v}$  is the Grueneisen parameter, a dimensionless parameter

that describes the vibrational effects that a volume change will produce, which is defined by the thermal coefficient of volume expansion ( $\beta$ ), isothermal compressibility ( $\kappa$ ), and the specific heat capacities at constant volume ( $C_v$ );  $\mu_a$  is the optical absorption coefficient;  $\mu'_s$  is the reduced optical scattering coefficient; and  $\Phi$  is the fluence (energy over area) distribution of the illumination.

To produce a quality photoacoustic signal, the light pulse used must be short. Specifically, laser pulse duration must be shorter than both the acoustic and thermal confinement time [123]. Physically, acoustic confinement time defines the amount of time it takes for the pressure wave to propagate out of a voxel (the smallest possible volume to image) during illumination. Similarly, the thermal confinement time defines the amount of time for the induced temperature change to diffuse out of this voxel. Voxel size is determined by the ultrasound transducer used: transducers with higher frequency will produce smaller voxels, as described previously. However, for typical ultrasound transducers, acceptable pulse times for photoacoustic imaging must be shorter than 100 ns [130].

Moreover, photoacoustic imaging is generally done by using light with a single wavelength. As seen in Equation 2.1, the strength of a photoacoustic signal is a function of optical absorption, which is a function of wavelength. Different optical absorbers (or chromophores) have different, specific optical absorption spectra. When imaging a target with many different chromophores (like soft tissue), using one specific wavelength can facilitate the imaging of a specific chromophore, providing clearer or more functional images.

Under these two assumptions, the induced acoustic wave propagation can be described as:

$$\left(\nabla^2 - \frac{1}{c^2} \frac{\partial^2}{\partial t^2}\right)p(\mathbf{r}, t) = -\frac{\beta}{C_P} \frac{\partial H(\mathbf{r}, t)}{\partial t} \quad (2.2)$$

where  $c$  is the speed of sound, and  $H(\mathbf{r}, t)$  is the heating function (i.e., the thermal energy converted to heat per unit volume per unit time) [123].

### 2.2.2 Photoacoustic Imaging: Microscopy and Tomography

Although the photoacoustic effect was discovered more than a century ago, the photoacoustic imaging modality began to grow only after the development of ultrasound transducers, lasers, and higher computational power [7]. In the last few decades, however, this new imaging modality has seen tremendous growth, both in research and preclinical settings.

What makes photoacoustic imaging so attractive is that it allows for optical imaging at depths far beyond the optical diffusion limit, a term that is usually equated with the transport mean free path of a photon within the medium (around  $1mm$  in soft tissue) [125]. Previous optical imaging techniques fall into two different categories: those which provide high resolution but demand minimal photon scattering (such as in microscopy), or those that image deeper within tissue with a sacrifice of resolution (such as in tomographic set-ups). More specifically, optical microscopy (such as confocal and fluorescent microscopy) can provide resolutions at sub-micron lengths, however must assume a small amount of scattering, and thus cannot penetrate tissue more than  $\sim 1mm$ . In comparison, optical tomography imaging modalities (such as diffuse optical tomography) can image as deep as centimetres, but can achieve resolutions of only around one third of the imaging depth [124]. Photoacoustic imaging differs from its optical counterparts by collecting optical information through ultrasound waves instead of reflected or transmitted photons. Because the scattering of ultrasound in tissue is about 1000x less than that of optical scattering, photoacoustic modalities offer high resolution images at depths that can reach up to 7 cm [124, 130]. Additionally, this resolution can be easily scaled to image biological structures from sub-micron to sub-millimetre sizes [124].

There is a risk in damaging tissue through laser exposure. ANSI has set out maximum permissible exposure (MPE) for different animal tissues, such as the skin or the eye [46]. Fortunately for photoacoustic imaging, the conversion efficiency from temperature to pressure is high enough to allow adequate SNR at the MPE levels for both skin and eye tissue [68].

Photoacoustic imaging can be split into two main categories: photoa-

oustic microscopy (PAM) and photoacoustic tomography (PAT), which now will be discussed in detail.

### **Photoacoustic Microscopy**

Photoacoustic microscopy involves simultaneously focusing both the optical illumination and the ultrasonic detection, done so confocally to maximize sensitivity. PAM uses single-element ultrasound transducers. This allows for resolutions scalable between the sub-micrometre to the millimetre regime [68,137]. PAM can be split into two categories, each denoted by which focal zone minimizes resolution. Optical Resolution PAM (OR-PAM) denotes smaller optical focal zones, whereas Acoustic Resolution PAM (AR-PAM) denotes smaller acoustic focal zones.

Similar to optical microscopy, OR-PAM involves focusing the excitation laser beam to a diffraction-limited spot. An optical-acoustic beam combiner is used to align optical excitation and ultrasonic detection coaxially and confocally [124,137]. Because the attainable size of the acoustic focal zone is much larger than the optical zone, resolution is determined by optical parameters (specifically, the wavelength and the numerical aperture of the optical objective lens). Therefore, sub-micron lateral resolutions can be achieved. For example, a lateral resolution of 220 *nm* with a maximum imaging depth of 100  $\mu\text{m}$  was attained by Zhang C *et al.* using a 532 *nm* wavelength and a numerical aperture of 1.23 [140] (see Figure 2.1). Akin to optical microscopy, optical diffusion severely limits the depth of imaging of OR-PAM to  $\sim 1\text{mm}$ . OR-PAM has been used to image single organelles [140], DNA and RNA in a cell nuclei without exogenous chromophores [134], as well as microvasculature in mouse ears, brains, and eyes [137].

For conventional AR-PAM, laser light is focused around the ultrasound transducer through a conical lens, providing a ring-shaped illumination (i.e., dark-field illumination). This allows for easier positioning of the ultrasound transducer and avoids stimulating chromophores on the surface of the sample, which would obfuscate the final image [137]. Acoustic focusing can be done through the addition of a concave acoustic lens. Lateral resolution for

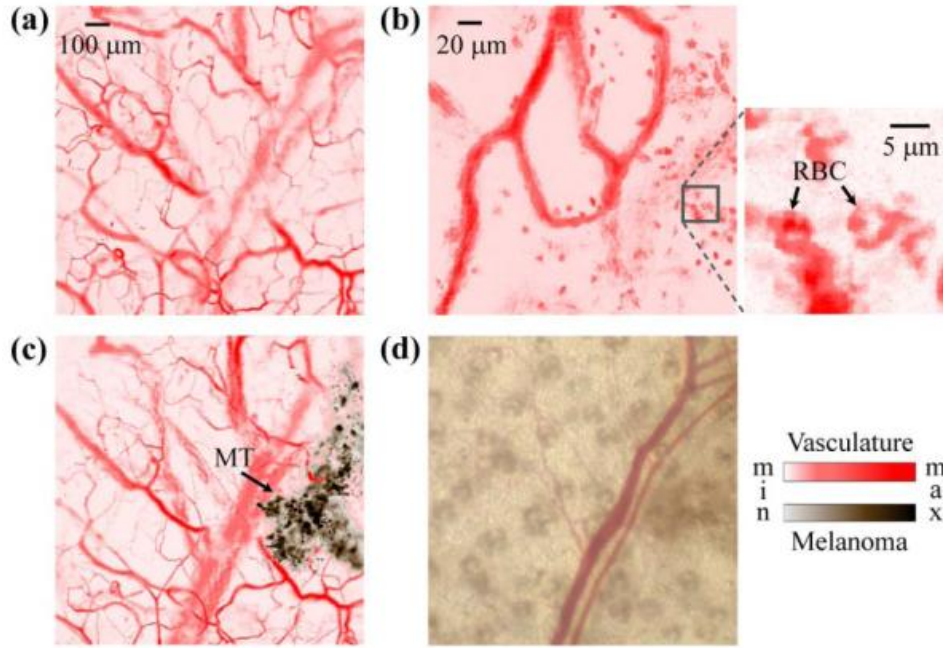


Figure 2.1: Melanoma growth monitoring in *in vivo* mouse ear. Adapted by permission from Macmillan Publishers Ltd: Nature Protocols [140], copyright 2010.

AR-PAM is determined by the wavelength of the resultant PA signal and the numerical aperture of the ultrasound transducer. Dark-field AR-PAM can achieve resolutions of  $45 \mu m$  [77]. Although this is two orders of magnitude larger than OR-PAM, its maximum imaging depth is 3 mm. This increase in depth is possible because AR-PAM does not rely on minimizing the size of its optical focal zone, and instead of governed by its acoustic focus. Application examples of AR-PAM include imaging human microvasculature in deep dermis [27], and monitoring growth of melanoma tumors in a mouse brain [108].

To create 2D or 3D images, the PAM system has to be scanned across the tissue being imaged. For a 2D image, mechanical scanning of 1 Hz/mm has been achieved [78]. Due to the importance of real-time imaging for clinical use, other methods have been developed [137], for example Yao *et al.*

producing 3-mm length OR-PAM image at 400 Hz using a water-immersible MEMS scanning mirror [135].

### **Photoacoustic Tomography**

In contrast with PAM, PAT relies on unfocused, full field illumination of the imaging target. Choosing an appropriate wavelength of light (such as near infrared (NIR) light, which is minimally absorbed by water and tissue [68]), light can penetrate deeply within tissue, diffusing throughout the imaging target. The resulting ultrasound waves are then acquired by an array of broad-band ultrasound elements. Due to the deep penetration of light, and the low-scattering of ultrasound in tissue, PAT can image up to 7 cm in depth [124]. Similar to ultrasound, axial and lateral resolution for PAT systems is generally determined by the centre frequency and bandwidth of the transducer used [124].

In the early days of PAT, a single element transducer was scanned across the target, however nowadays ultrasound array transducers are primarily used [7]. Unlike PAM, PAT also relies on reconstruction algorithms to create images. These algorithms have been derived in similar methods to other imaging modalities such as ultrasound and CT, and will be discussed in depth in the following section.

The array transducers used come in a variety of different geometries, such as linear [31, 133], circular [30, 127], and bowl-shaped [57, 65], to name a few. Linear arrays are the most versatile, easily applied to the outside of the tissue. However, due to the nature of some reconstruction algorithms, their limited view can cause lower resolutions and side-lobe artifacts. In contrast, full-view array transducers are able to detect photoacoustic signal from all directions (within the imaging plane), providing images that do not suffer from missing boundaries [131]. These geometries, however, can only image targets that fit within the transducer itself, reducing their versatility.

As mentioned previously, PAT is easily scalable, able to reach high spatial resolutions at larger depths by adjusting the centre frequency and bandwidth to suite the application. For large areas, however, scalability can become

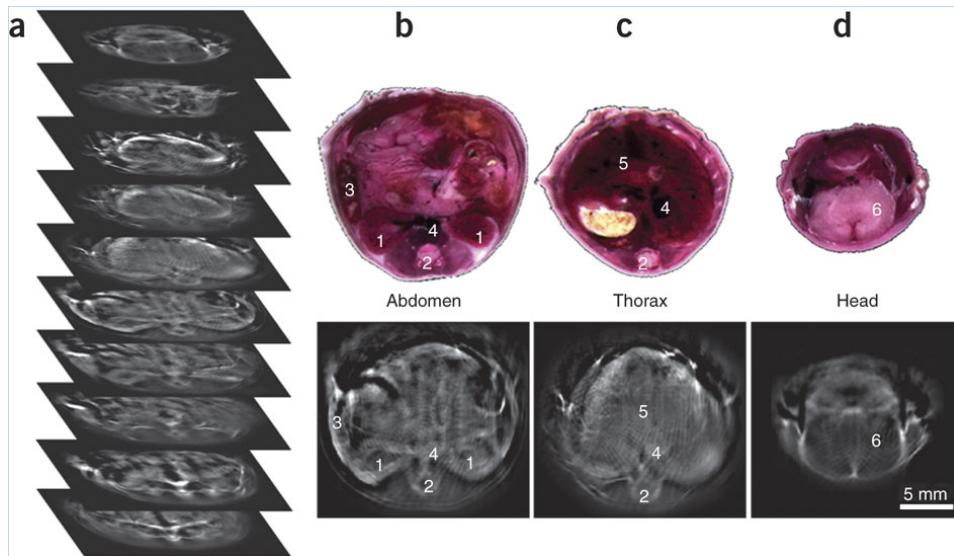


Figure 2.2: a) Photoacoustic Tomography slices of a mouse *in vivo*. b,c,d include abdominal, thoracic, and head cross-sections respectively with *ex vivo* images for comparison. Reprint with permission from [100].

difficult. As shown in Equation 2.1, the strength of a photoacoustic signal is dependent on the fluence of the illumination, or in other words the energy per area deposited on the target. For a blanket-illumination, where the imaging target is 'blanketed' with light, larger areas necessitate higher laser energies to produce the same signal magnitude. For certain photoacoustic set-ups (especially considering lower laser outputs from optical parametric oscillator (OPO) or dye lasers, and energy losses through inefficient fibre bundles or optical components), producing high enough laser energies to match ANSI limits may provide difficult, limiting scalability of the system. In this thesis, we discuss a scanned-mosaic method to mitigate this problem (Chapter 3).

Photoacoustic tomography has been applied to fields such as vascular biology, oncology, neurology, and cardiology, to name a few. These applications have been reviewed extensively in the works cited here [7, 68, 124].

## Photoacoustic Tomography Reconstruction Techniques

The most simple PAT reconstruction technique borrows from the delay-and-sum algorithm for ultrasound images. For a point in the imaging plane, the distance between the point and each element in the array transducer can be calculated. These distances can be converted into time delays using the speed of sound of the imaging medium. Applying the time delays to the signals from each element and summing the results will form an approximation of the initial photoacoustic signal at this specific point. Repeating for all points in the imaging plane will result in the final image. Although this method is conceptually intuitive and easy to implement, there has been development into other reconstruction algorithms that are more accurate, and less computationally demanding. A few general examples will be given, however many others can be found in the reviews cited here [7, 62].

One alternative is filtered backprojection, which can reconstruct exact initial photoacoustic signals for certain array geometries, specifically spherical, cylindrical, and planar [129]. Similar to delay-and-sum, this method essentially backprojects the measured photoacoustic data from each element in time through the imaging plane. This backprojected signal is not just the pressure measured by the element (as it is for delay-and-sum), but includes the time derivative of the pressure signal and is weighted by the solid angle of the element in question. Furthermore, the backprojection term can be filtered to remove the impulse responses from the element. This method is also quite computationally demanding, however has been implemented for many full-view PAT experiments [59, 65]. This method assumes a closed array geometry, thus limited-view PAT set-ups (such as those using linear arrays), will suffer from artifacts (such as side-lobe degradation) [128].

Other reconstruction methods that have been developed rely on forward models that simulate the physics of acoustic propagation. One example, typically called time-reversal methods, uses a numerical acoustic propagation model 'backwards' to reproduce the propagation of photoacoustic signal from the element to the initial emission spot (in other words, it replays what happened backwards in time) [7]. This method can be applied to any ar-

ray geometries, and can also accommodate heterogeneities in the medium’s speed of sound (where the algorithms mentioned previously assumed it to be homogeneous). Time-reversal methods, however, rely on fast, accurate propagation models, increasing the implementation complexity of this method.

Model-based inversion relies on a forward model that simulates detected photoacoustic signal for an estimate of chromophore position within the imaging field. By comparing the simulated signal with the measured data, the position of the imaging targets can be iteratively shifted until the difference between simulation and measurement is minimized. Rosenthal *et al.* describe a fast model-based inversion technique that gains speed by reducing generality [102]. Specifically, with the knowledge of array geometries and impulse function of the elements, an inverse matrix independent of measured data can be pre-computed, allowing for real-time reconstruction.

### 2.3 Ultrasound Tomography

Conventional ultrasound utilizes linear (or curved) array transducer geometries. One of the suppositions guaranteed by these geometries is that the signals received will only be the reflected or scattered transmitted waves. In the 1970s, Greenleaf *et al.* proposed to create tomographic images with ultrasound, influenced by CT imaging (Computerized Tomography with x-rays) [33]. They proposed that, like CT, the non-reflected ultrasound waves could be used to measure information such as acoustic speed of sound, attenuation, and absorption [34]. These parameters could be desirable in a clinical setting, for example in breast cancer imaging. They demonstrated that the speed of sound and attenuation of acoustic waves could accurately differentiate benign and malignant masses in the breast [34]. To accomplish this, the set-up utilized by Greenleaf *et al.* consisted of only two single-element ultrasound transducers scanned around the imaging target [34]. Following Greenleaf, ways of obtaining these transmission parameters were studied by a few other groups [2, 16, 73]. Although their results were promising, research into ultrasound tomography stagnated mainly due to the fact that the amount of computational power necessary to collect, process, and recon-

struct the data acquired needed to be much higher than what was currently available, especially for real-time imaging. Furthermore, many concluded that, for this imaging modality to be clinically useful, they would require fast scanning or imaging equipment, operator-independence, and preferably, multi-modal capabilities [23].

Since then, significant progress has been made both in computational power and in available hardware for ultrasound imaging. Furthermore, there has been increased development of full-view array transducers used in PAT, which could be easily utilized for an ultrasound tomography experiment. These full-view array transducers can provide the necessary speed and operator-independence mentioned previously. These factors, in part, have influenced a resurgence in research towards ultrasound tomography.

With ultrasound tomography, both reflection and transmission information can be gathered. In the most broad sense, reflection information can be used to create morphological images, similar to those of conventional ultrasound, whereas transmission information can produce quantitative images of acoustic speed of sound and attenuation. In the next sections, the developments of these two types of images will be discussed separately, however it is important to note that the tomographic systems examined tend to acquire and reconstruct both types of information simultaneously.

### **2.3.1 Reflection-based Ultrasound Tomography**

Reconstruction reflection information for ultrasound tomography borrows its algorithms from conventional ultrasound. However, the specific array geometries necessary for ultrasound tomography limit the type of transmit sequences that can be used. For reflection-mode ultrasound tomography, the most common ultrasound technique implemented is called synthetic-aperture [110]. In geophysics, this reconstruction technique better known as Kirchoff migration [23]. This technique consists of transmitting a pulse on one element at a time while receiving signal from all elements in the array. Thus, where the pulse begins and ends is known. For each pixel in the image, distances can then be calculated between it and both the

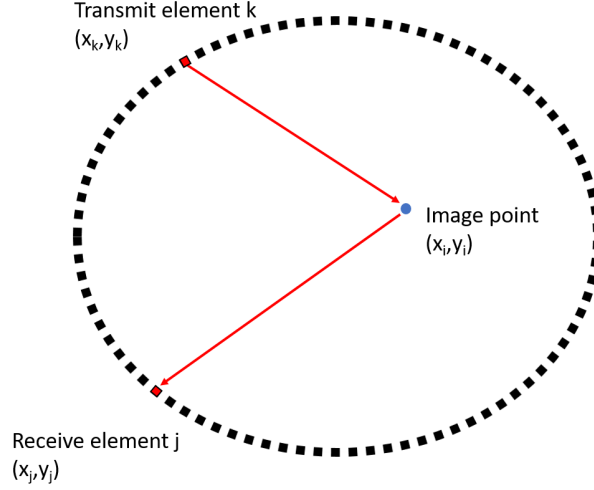


Figure 2.3: Schematic of ring-array transducer.

transmit and receive element. Assuming a constant speed of sound, these distances can be converted to time-delays. Like in delay-and-sum for PAT, each received signal is delayed and summed for every pixel, forming a final reflection-mode image.

Specifically, for transmitting element  $k$  at position  $(x_k, y_k)$  and receiving element  $j$  at position  $(x_j, y_j)$ , the resulting A-scan for this transmit-receive pair will be labeled  $A_{k,j}(t)$ . To create a DAS image  $I(x, y)$ , A-scans are time-delayed and summed coherently for all transmit-receive pairs at every position  $(x, y)$ . For a point  $(x_i, y_i)$ , a time delay  $\tau_{i,j,k}$  for a specific transmit-receive pair  $(j, k)$  can be calculated as

$$\tau_{i,j,k} = \frac{1}{c_0} \left( \sqrt{(x_i - x_k)^2 + (y_i - y_k)^2} + \sqrt{(x_i - x_j)^2 + (y_i - y_j)^2} \right) \quad (2.3)$$

To calculate the value of pixel at point  $(x_i, y_i)$ , the DAS algorithm can be formulated as:

$$I(x_i, y_i) = \sum_k \sum_j A_{j,k}(t = \tau_{i,j,k}) \quad (2.4)$$

The power of delay-and-sum lies in this fact: Let us assume there is a scattering or reflecting target at point  $(x_p, y_p)$ . When the image point  $(x_i, y_i)$  corresponds with a this target point  $(x_i = x_p, y_i = y_p)$ , the delayed A-scan signals from all transmit-receive pairs will sum constructively. In other words,  $\tau_{i,j,k} = \tau_{p,j,k}$  for all  $j, k$ . When an image point does not correspond to a target point,  $\tau_{i,j,k} = \tau_{p,j,k}$  may still hold for a small number of  $j, k$ . Therefore, the resulting pixel value  $I(x_i, y_i)$  will not constructively add up for all  $j, k$ , leaving a much smaller pixel value. After summation, the final image values will correspond to the target positions, and a reflection-mode UST image can be created.

Usually in conventional ultrasound, an envelope of the received signal from each element (called an A-scan) is used for reconstruction. This removes the oscillations of each pulse signal (in other words, removing phase information), producing smoother imaging results. It has been shown that imaging the envelope of the A-scans for ultrasound tomography will produce high SNR images, but will reduce the resolution. By imaging the raw A-scan data, resolution will be increased at the expense of echo texture and SNR [23, 110].

One large hurdle for synthetic aperture based ultrasound is the intrinsically low SNR. Because only one element is used for transmission, the total pressure output per event is low. This can be mitigated by incoherent compounding [80], or simply by increasing the amount of elements in your transducer [110]. Incoherent compounding will fundamentally worsen the theoretical resolution of the system [80], preventing diffraction-limited resolution to be achieved. Moreover, as the amount of elements in the ultrasound array increase, so does the required computational power, necessitating either long wait times [110] or implementation of GPUs [11]. In Chapter 4, this thesis will introduce a spatial-encoding technique that produces increased SNR for a synthetic aperture tomographic system while retaining the diffraction-limited resolution capabilities of the system. This is done with

a standard ring array transducer with 256 elements (an order of magnitude less than for Stotzka *et al.* [110]).

For a circular array transducer, ultrasound reflection tomography has been developed by Mercep *et al.* in conjunction with their preclinical PAT infrastructure, creating photoacoustic and ultrasound images of mouse cross-sections [79, 80]. It has also been developed by Duric *et al.* in conjunction with their ultrasound transmission tomography set-up [23] for the purpose of human breast cancer imaging [142].

At Forschungszentrum Karlsruhe, a large, cylindrical array transducer has been created, able to create 3D ultrasound tomographs [74]. This transducer has 384 transmitting elements and 1536 receiving elements, and is able to rotate to six unique positions. An ellipsoidal backprojection algorithm, similar in theory to synthetic aperture, has been developed for this new geometry [107]. Due to the high volume of elements, they have compared the application of GPU- and FPGA-based accelerations to their system [11, 12]. They have also developed deconvolution methods for reconstruction [109], and phase aberration corrections [105, 106]. This system has recently been used in clinical research for breast cancer [32, 104].

### 2.3.2 Transmission-based Ultrasound Tomography

Generally, transmission tomography computes specific physical parameters by comparing the original transmitted wave with the final received wave. Many different reconstruction techniques have been developed to transform this transmission data into images mapping speeds-of-sound and attenuation. A few major ones will be explained in this section.

#### Ray-based Reconstruction

Ray-based reconstruction basically models the path of ultrasound pulses as rays stretching from their transmit element to the receiving element. As the pulse travels along this path, the speed-of-sound and attenuation along this path will affect the wave's time-of-flight (TOF) and amplitude, respectively. Under this framework, the Karmanos Cancer Institute have

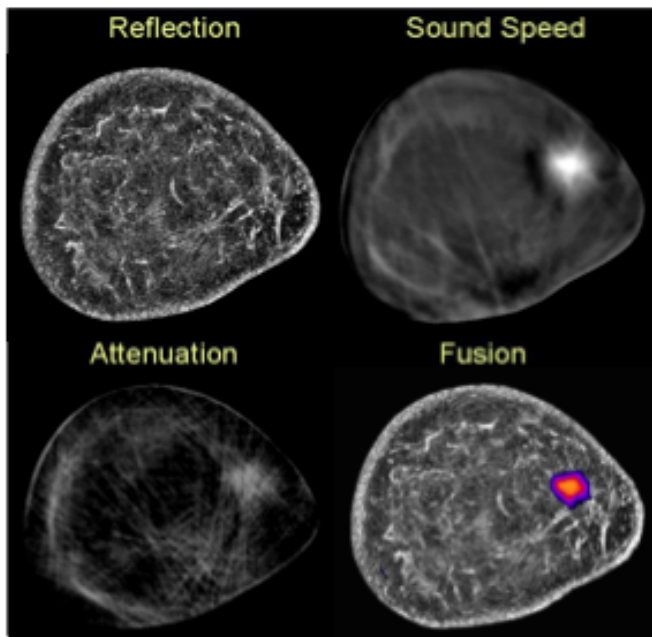


Figure 2.4: A reflection-mode, sound-speed, attenuation, and fusion-mode image of a breast from Duric *et al.* using ray-based reconstruction. Fusion image consists of a composite of all three images. Reprint with permission from [24]

developed speed-of-sound and attenuation reconstruction methods for ultrasound tomography [23], which will be described in detail in the following paragraphs. It has been implemented in their CURE (Computed Ultrasound Risk Evaluation) ultrasound tomography system.

The arrival time to a receive element of an transmitted pulse from element can be calculated by taking the ratio of the distance between the two elements and the speed-of-sound along the path. By measuring the deviations of measured arrival times, the speed-of-sound can be obtained through inversion.

This can be implemented as follows [23, 69]: Let the amount of transmit/receive element pairs equal  $N$ . Let the total amount of rectangular grid elements in the imaging field equal  $M$ . The TOF for one transmit/receive pair ( $T_i$ ) can be calculated by summing the lengths of this ray's path through

each grid element ( $l_{i,j}$ ) multiplied by the inverse of the speed-of-sound of each element ( $b_j$ ), which is:

$$T_i = \sum_{j=1}^M l_{i,j} b_j \quad (2.5)$$

It is difficult, however, to accurately measure  $T_i$  with the precision necessary. Instead, a difference of arrival time between the inhomogenous medium in question and a medium with a homogenous speed-of-sound ( $b_j = b_0$  for all  $j$ , corresponding to a TOF =  $T_0$ ) is used. This can be expressed as follows [23]:

$$\begin{aligned} T_i - T_0 &= \sum_{j=1}^M l_{i,j} (b_j - b_0) \\ \Delta T_i &= \sum_{j=1}^M l_{i,j} \Delta b_j \end{aligned} \quad (2.6)$$

This can be converted into a matrix equation:

$$\delta \mathbf{T} = \mathbf{L} \delta \mathbf{B} \quad (2.7)$$

where  $\delta \mathbf{T}$  is an Nx1 matrix,  $\mathbf{L}$  is an NxM matrix, and  $\delta \mathbf{B}$  is an Mx1 matrix. By using a least-squares algorithm,  $\delta \mathbf{B}$  can be obtained and converted into a speed-of-sound image.

One major oversight of this algorithm is that it assumes that the pulse rays are straight, or in other words, it neglects refraction [69]. Because speed-of-sound differences cause refraction, Li *et al.* amended their reconstruction by adding to it a bent-ray algorithm [69]. This algorithm calculates the TOF by solving the eikonal equation [69], using the  $b_j$  value calculated by the first algorithm and deconstructing it into its Cartesian components ( $b_x$  and  $b_y$ ). The pulse can then be backprojected from receive element to transmit element with respect to speed of sound inhomogeneities. This is done by implementing Klimes' grid travel-time tracing technique [53]. For each grid element, a directional vector  $G = -(b_x, b_y)$  is used to trace the

pulse's path through the element. At the boundary of the grid element, this direction vector is updated. This is repeated until the path hits a transmit element. By iterating between these two algorithms, a speed-of-sound image can be created that includes refraction.

Attenuation information can be obtained using a similar approach. Instead of TOFs, however, the change complex energy of the pulses is used. This change is between the energy of the pulse travelling through water ( $E_W$ ) and the same energy through the imaging target ( $E_R$ ). These energies can be used to calculate the effective attenuation (relative to water) [69]. The calculation of these three terms can be seen in Equation 2.8 and 2.9.

$$E_W = \int_{t_1}^{t_2} |W(t)|^2 dt \quad (2.8)$$

$$E_R = \int_{t_1}^{t_2} |R(t)|^2 dt$$

$$C = \int_{ray} a_0 dl = \log_{10}\left(\frac{E_W}{E_R}\right)/f_n \quad (2.9)$$

where  $W(t)$  and  $R(t)$  and the enveloped pulses for water and the target respectively,  $t_1$  and  $t_2$  are the times where the pulse snippet begins and ends,  $f_n$  is the Nyquist frequency of the system, and  $a_0$  is the attenuation at each point on the ray's path. Equation 2.9 can be converted into a familiar equation [23, 69]:

$$C_i = \sum_{j=1}^M l_{i,j} a_{0,j} \quad (2.10)$$

which can be used to calculate  $a_{0,j}$  and then form an attenuation image using the same methods as described previously.

Duric *et al.* implemented these reconstruction algorithms, along with reflection-mode algorithms mentioned in the previous section, with a ultrasound tomography system consisting of a 256 element, 360° ring transducer [23]. This set-up has been used clinically for breast cancer imaging

research, able to clearly visualize lesions in the breast due to the increased sound speeds within the lesions [69,90], as seen in Figure 2.4.

### **Wave-based Reconstruction**

Ray-based reconstruction techniques are robust, rapid, and relatively easy to implement [96]. This is, in part, due to certain assumptions that must be made, such to avoid the effects of diffraction, guided-waves, and other acoustic modes caused by heterogeneities in the imaging plane [96]. Waveform-based reconstructions, that use complex acoustic wave models to iteratively compare simulated solutions to measured ones, can fully account for any heterogeneities included in the specific model used. The trade-off, of course, is that as the complexity of the model increases, the computational power must also increase, slowing down reconstruction times drastically [91].

Pratt *et al.*, using the CURE system previously discussed, were able to reconstruct breast phantom images with waveform-based algorithms, highlighting improvements of resolution compared with the ray-based algorithms mentioned previously [96]. To improve reconstruction times, Li *et al.* implemented GPU-based algorithms, finding an increase of speed of about 2.5x [70]. Ozmen *et al.* compared a few different waveform reconstruction algorithms with a ray-based algorithm on simulated breast data. Their algorithms included those based on Born inversion (both using a filtered backprojection approach and a conjugate gradient scheme), and contrast source inversion and compared the resulting speed-of-sound images [91].

### **Multi-band Reconstruction**

Ultrasound attenuation in tissue is frequency-dependent. This dependency is characteristic of the attenuating material. Therefore, measurements of attenuation and different frequencies may be utilized for tissue differentiation. As shown previously, ultrasound tomography can be used to measure attenuation. With this in mind, Kim *et al.* developed an ultrasound tomography system that measures attenuation at multiple frequencies in hopes of powerful and specific tissue differentiation [48]. This system consists of

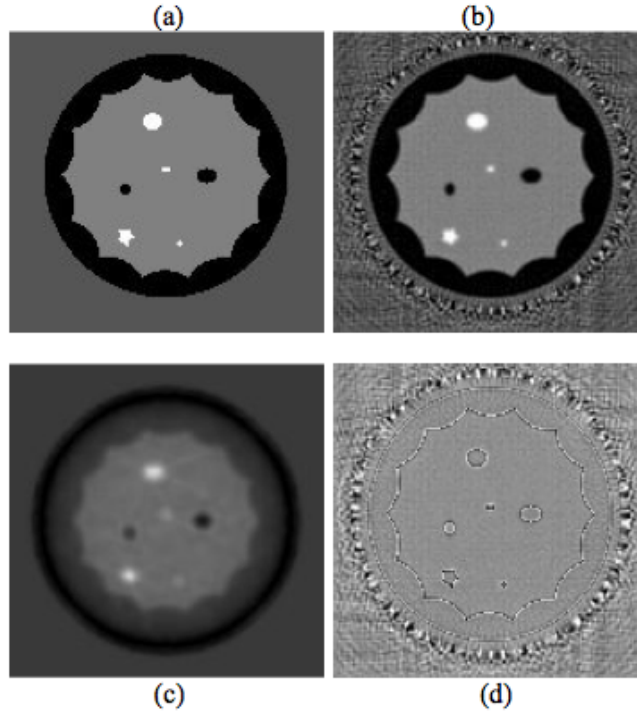


Figure 2.5: A comparison of two sound speed reconstruction algorithms in simulations. (A) true model, (b) waveform tomography, (c) ray-based, (d) b-a residual image. Reprint with permission from [70]

two linear bands of elements facing toward each other, attached to stages that can move them around the centre and up and down. Therefore, the position of each element can be described using its elevational position ( $z$ ), its angular position ( $\theta$ ) and its azimuthal position along each linear array ( $x$ ). Only transmission data is obtained for their experiments.

Their reconstruction method relies on the fact that frequency-dependent attenuation for one voxel can be described as the ratio between the frequency spectrum that enters a voxel and the forward-propagating frequency that leaves the voxel [51]. This ratio can be described as an attenuation transfer function specific to each voxel. When an ultrasound pulse travels through a collection of voxels, its total transfer function can be understood as the product of the transfer functions for each individual voxel. Therefore, the

total attenuation ( $A_t(f)$ ) along this path can be described as [51]:

$$A_t(f) = \log \left| \frac{Y_t(f)}{Y_r(f)} \right| \quad (2.11)$$

where  $Y_t(f)$  and  $Y_r(f)$  are the frequency-domain of the transmitted and received pulses, respectively.  $Y_t(f)$  is difficult to measure, thus Kim *et al.* normalized Equation 2.12 by subtracting from it the total attenuation of a water-only measurement ( $A_w(f)$ ) (i.e., data collected without a target inside the imaging cavity). Therefore, their final frequency-dependent attenuation measurement  $A(f)$  for a transmit/receive pair for position  $(x, \theta, z)$  is [51]:

$$\begin{aligned} A(x, \theta, z, f) &= A_t(x, \theta, z, f) - A_w(f) \\ &= \log \left| \frac{Y_t(f)}{Y_r(x, \theta, z, f)} \right| - \log \left| \frac{Y_t(f)}{Y_w(f)} \right| \\ &= -\log \left| \frac{Y_r(x, \theta, z, f)}{Y_w(f)} \right| \end{aligned} \quad (2.12)$$

This ultrasound tomography set-up is analogous to that of a CT set-up (where x-rays are transmitted through a target, received on the other side, and both transmit and receive elements are rotated around the target), except that CT only uses one frequency. The same reconstruction algorithm (filtered backprojection, based on inverting the Radon transform function) can thus be used to create a final image for each frequency considered, providing multispectral frequency information for each pixel in the image [48, 51].

This system uses an 8 MHz centre frequency with a 50% fractional bandwidth, however Kim *et al.* have observed adequate SNR from signals with frequencies of 25 MHz (specifically, an SNR of 39 dB at 25 MHz). Therefore, for image formation, they utilized measured attenuation coefficients at frequencies from 6.25 MHz to 25 MHz [48].

With the knowledge of specific tissue attenuation characteristics, this system has been shown to be able to differentiate between different anatomical structures, such as renal calyces and blood vessels in a sheep kidney

phantom [48]. Zografos *et al.* were also able to identify small ( $< 15mm$ ) lesions in the human breast [141, 142].

## 2.4 Ultrasound Anisotropy

Anisotropic scattering of ultrasound can be understood as such: the scattered signal strength is dependent on the angle created between the transmit element, receive element, and the target. This can be caused by many different parameters, including the geometry, size, structural components and material components of the scatterer. For most conventional ultrasound imaging, scattering is assumed to be isotropic, however anisotropy may provide new, useful clinical information [117].

One source of anisotropy in ultrasound measurements is caused by high-scattering fibres within tissue [92]. Ultrasound will maximally scatter at orthogonal angles relative to the fibre, and will minimally scatter when the ultrasound wave travels along the fibre. Assessment of this architecture may be useful for measuring the progression of myocardial disease [92], and in measuring changes in the extracellular matrix form around aggressive tumours [75, 86]. In Chapter 5, we introduce an ultrasound tomography based anisotropic visualization system capable of detecting fibre orientations within phantoms.

Another source of anisotropy is caused by a difference in density between the scatterer and its surrounding medium. Intuitively, this can be understood thusly: When an flat ultrasound wave hits a dense scatterer, the scatterer will move back and forth in the direction of the wave. Thus, the resulting scattering wave will have the highest intensity along this axis, and the lowest intensity orthogonal to this axis. This can be compared to the signal caused by a difference in compressibility. An ultrasound wave will cause a compressible scatterer to shrink and expand. This will result in scatter that has equal intensity in all directions.

Mathematically, this can be described using ultrasound scattering theory [18]. Let us define a compressible sphere with radius  $a$ , compressibility  $\kappa_t$  and density  $\rho_t$  that is suspended in a ultrasound medium with compress-

ibility  $\kappa_0$  and density  $\rho_0$  at position  $r$  away from the transmitting transducer. The transmitted ultrasound pulse will have a wavelength  $\lambda$  and an initial pressure  $p_0$ . For a scatterer that is adequately small ( $a \ll \lambda$ ) and far enough away ( $r \gg \lambda$ ), the resulting pressure change due to scattering ( $p_s$ ) can be described as:

$$p_s(r, \theta) \approx p_{im} e^{-jkr} \frac{k^2 a^3}{3r} \left\{ \frac{\kappa_v - \kappa_0}{\kappa_0} + \frac{3(\rho_v - \rho_0)}{2\rho_v + \rho_0} \cos(\theta) \right\} \quad (2.13)$$

where  $p_{im}$  is the pressure of the transmitted pulse,  $k$  is the wavenumber of the pulse, and  $\theta$  is the angle of the scattered pulse relative to the transmitted pulse axis. From Equation 2.13, it can be seen that a scatterer's signal is comprised of two terms: one relating to the compressibility difference and one related to the density difference. The compressibility term is independent of  $\theta$ , and thus emits isotropic scattering. This term can be labeled as the monopole term. The density term is a function of  $\theta$ , and thus emits anisotropic scattering. This term can be labeled as the dipole term due to the cosine weighting.

By exploiting monopole and dipole scattering for ultrasound scatterers, images that differentiate between dense and compressible scatterers can be created [117], discussed in depth in Chapter 6. This may be useful for enhanced breast microcalcification imaging [117]. Microcalcifications in the breast are one of the earliest signs of breast cancer [84]. The shape, size, and pattern of microcalcifications in the breast can be used to determine their malignancy. Typically, x-ray mammography is used to image microcalcifications. This modality, however, relies on ionizing radiation. Due to the nonionizing nature of ultrasound, the use of ultrasound for this detection has been investigated [3, 35, 42, 43], however differentiating microcalcifications from the noisy background echo texture is difficult. Due to the high density of microcalcifications with respect to breast tissue, anisotropic visualization may provide a useful adjunct for ultrasound microcalcification imaging. In Chapter 6, we present novel reconstruction techniques applied to an ultrasound tomography system that exploits Equation 2.13 to decouple

compressibility and density components of scatterers.

## Chapter 3

# Blanket Illumination vs Scanned-Mosaicking Imaging Schemes for Wide-Area Photoacoustic Tomography

### 3.1 Introduction

Photoacoustic imaging is an emerging biomedical imaging modality that combines the spatial resolution of ultrasound with sensitivity to optical absorption fundamental to optical imaging systems [124,130,136]. Photoacoustic imaging relies on a photothermal mechanism [122,136], where optically absorbing objects expand and contract when they absorb light. This mechanism is produced by a pulsed laser illuminating chromophores, which expand and contract, sending ultrasonic waves through their respective media. These ultrasonic waves can be measured using ultrasonic transducers, and can be reconstructed into images. Photoacoustic tomography (PAT) is a photoacoustic technique similar to x-ray computer tomography, where image slices can be re-created from data collected by transducer elements that circle the imaged object [129,136] This technique has recently been used for breast

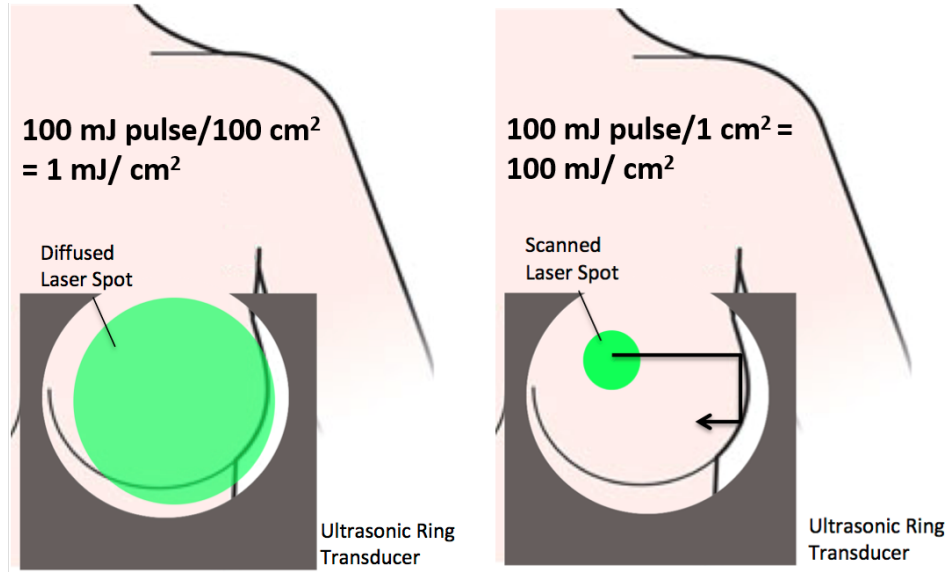


Figure 3.1: Comparing the diffused laser beam technique (left) with the scanned-mosaicked beam technique (right) for a ring transducer.

imaging [58,59], with applications for breast cancer detection.

Kruger *et al.* image the breast by diffusing a single pulsed shot from a laser over the entire area (blanket illumination), and reconstruct the tomographic image using a circular transducer [59]. Because of the limited power of these pulsed lasers, combined with the relatively large imaging area, the fluence (or energy of pulse per unit area) is much lower than what is permitted. This fluence limit is defined by the maximum permissible exposure of light and delineated by ANSI. Because fluence is directly related to signal, using a fluence much lower than the ANSI limit does not utilize the highest signal to noise ratio (SNR) available by the system.

We demonstrate a scanned approach, creating images with a small-area beam that has a fluence that can reach the ANSI limit. Because of this, these images will have a much higher SNR than the diffused beam. The small beam will then be scanned across a wide area, creating high-SNR image patches, which will be mosaicked together to create the final image. A comparison between the two light delivery techniques can be seen in Fig-

ure 3.1. This scanned mosaic (SM) light delivery technique will utilize the maximum fluence allowable by any system, and theoretically should be able to create the high SNR images faster than averaging the diffused-beam information. We first develop the theoretical background for this work, and then simulate the fluence gain for different spot sizes and depths in a scattering medium using the Monte Carlo method. Finally, we will image a tissue-mimicking phantom using both methods and measure the SNR gain.

## 3.2 Theory

Photoacoustic signals are created from thermo-elastic expansion of chromophores due to absorption of light. The pressure caused by this thermo-elastic expansion can be understood as [129, 136]

$$p(r) = \Gamma(r)\mu_a(r)\Phi(r) \quad (3.1)$$

where  $p$  is the initial pressure,  $\Gamma$  is the Grüneisen parameter (which converts energy to pressure),  $\mu_a$  is the absorption coefficient, and  $\Phi$  is the fluence of the beam. For tomographic images, the response measured from each transducer is back-projected cyclically (due to the circular propagation of the ultrasonic waves) [129]. By backprojecting the signals from transducers that circle the object, an image of the object will be formed [129]. From equation 3.1, it is clear that the initial pressure image intensity is directly proportional to the fluence  $\Phi$ . Thus, by increasing the fluence, one can increase the signal measured, and thus increase the SNR of the image.

Previously whole-breast tomography systems have used lasers with non-tunable wavelengths using pulse-energies of at most 200-300 mJ spread over the whole breast ( $>100 \text{ cm}^2$ ). Tunable lasers might give at most 100 mJ/pulse, with an average of  $\sim 1 \text{ mJ/cm}^2$  surface fluence. The ANSI limit, however, is  $20 \text{ mJ/cm}^2$  for visible light, and up to  $100 \text{ mJ/cm}^2$  for near infrared (NIR) light, which is 20-100x higher than what is being used currently. By using smaller (and variable) laser spot areas, reaching the ANSI limit is possible with any system, and thus one can utilize the highest SNR

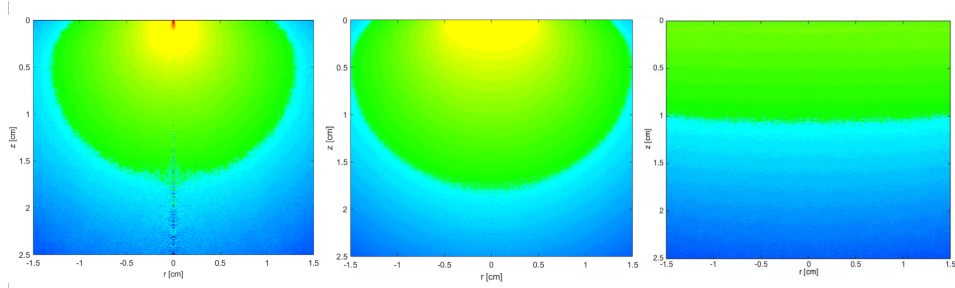


Figure 3.2: Fluence distribution for pencil beam with radii 0.01 cm (left), 0.5 cm (centre), and 2.5 (right).

available from any PAT system for any wide-area application.

Near the surface of tissue, we can characterize the SNR increase by focusing on the proportional relationship between photoacoustic signal (or initial pressure) and the fluence. For this paper, we calculate SNR as the ratio between the maximum signal produced and the standard deviation of background noise. First, let us define  $SNR_D$  as the SNR achieved using one diffused laser shot over an area. If we were to split the area into  $N$  sections and illuminate each section with its own laser shot, the fluence near the surface of the tissue will increase by  $N$ , thus the SNR for this will be  $N \times SNR_D$ . Another way to increase the image's SNR is through averaging. To match this SNR increase, however,  $N^2$  averages would have to be done. This is due to a signal increase of  $N$  times for  $N$  averages, and, respectively, a noise increasing of  $\sqrt{N}$ , thus causing an overall increase of  $\sqrt{N}$ . This shows that, although SM imaging necessitates more laser shots (and images) to create the final image, the SNR improvement using this method will be as much as  $\sqrt{N}$  times higher than averaging the same amount of diffused-light images.

### 3.3 Simulations

Although the previous example was encouraging, it ignored the scattering effects of turbid media that become important as we image deeper into tissue. To measure this effect, we used simulations based off of Monte Carlo

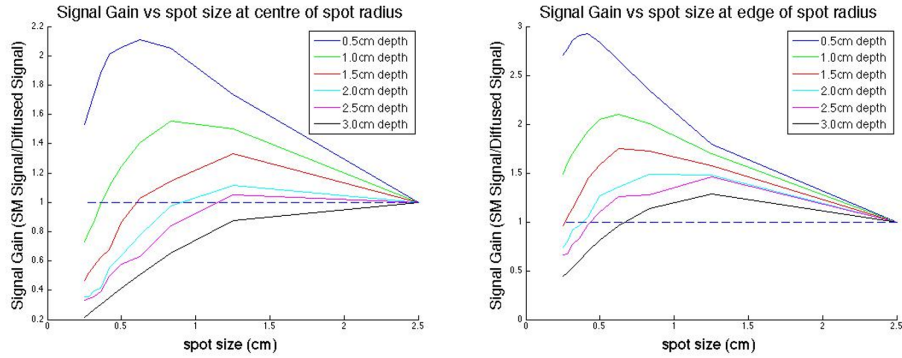


Figure 3.3: Monte-Carlo results for signal gain measured as a ratio between a small spot size vs a large spot size (2.5 cm radius). Values were measured at the edge of the small spot radius (left) and at the centre of both spot radii (right) at different depths. The dashed line denotes when the gain of the small spot size is larger than that of the large spot size

methods for photon transport [121] to measure the fluence increase as a function of spot size and depth.

For the simulations, we use an absorption coefficient of  $0.1 \text{ cm}^{-1}$ , a scattering coefficient of  $100 \text{ cm}^{-1}$ , and an anisotropy factor of 0.9. The results can be seen in Figure 3.3.

As expected, increasing depth decreased the ratio between fluences for beam spots with small and large radii. Another thing to note is the maximum spot-size for fluence gain. After this maximum, decreasing the spot size has a negative effect. Although the fluence of the beam would continue to increase, the beam area would become too small to penetrate deeply into the tissue, and thus any SNR improvement would be lost. This can be seen in Figure 3.2, where a spot radius  $50\times$  smaller than  $0.5\text{cm}$  displays a similar fluence distribution.

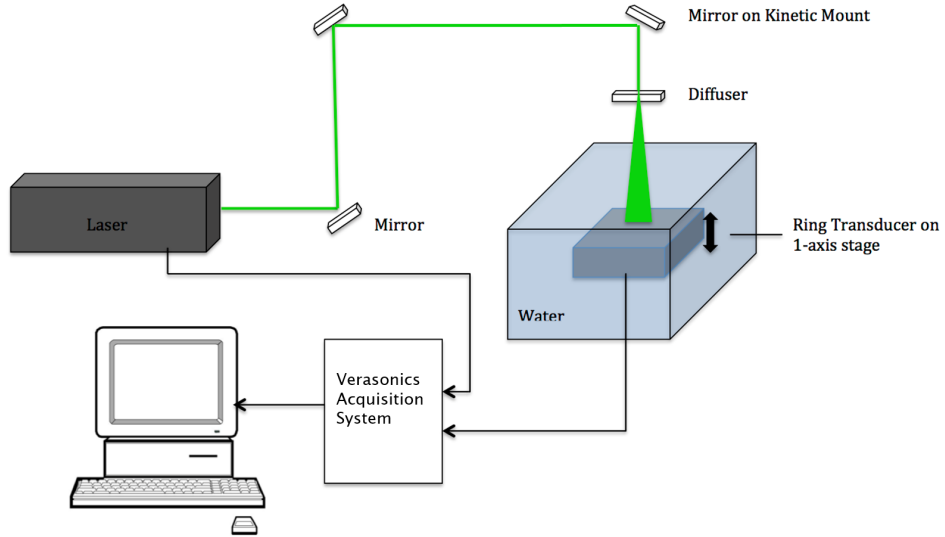


Figure 3.4: Schematic of experiment.

Table 3.1: Imasonic Ring Transducer specifications

Number of Elements	256	Elevational Acoustic Focus	37 mm
Radius of Curvature	40 mm	Element Pitch	0.7 mm
Centre Frequency	5 MHz	Kerf	0.1 mm
Fractional Bandwidth	56	Elemental Width	10 mm

## 3.4 Experimental Results

### 3.4.1 Methods and Materials

We used a 256-element,  $256^\circ$  Imasonic ring transducer (specifications can be seen in Table 3.1 in conjunction with a Verasonics 128-channel multiplex acquisition system. A 532 nm pump laser was used with an average energy of 18 mJ. A removable diffuser was used to diffuse the beam across a 5 cm diameter imaging area. The scanned mosaic beam was also measured to have a diameter of 1 cm. The scattering phantom (10% w/w gelatin, 1% w/w intralipid) was imaged. A 2 mm long hair was inserted 0.5 cm

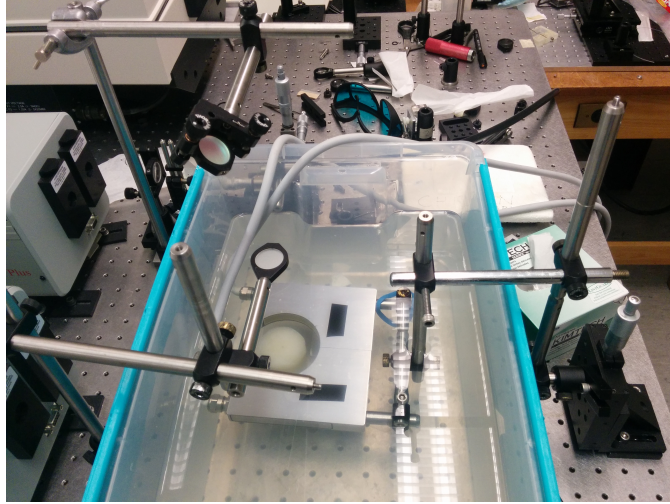


Figure 3.5: Image of transducer in use.

deep into the phantom perpendicular to the ring transducer face. A water bath was used as an ultrasound coupling medium. The phantom was moved to nine positions, gathering information from the diffused and SM imaging techniques. The resulting images were reconstructed using a filtered back-projection algorithm [120] in MATLAB.

### 3.4.2 Experimental Results

We measured an SNR gain of 2.9x between the scanned mosaicked and diffused beam. The results can be seen in Figure 3.6. This result agrees with our Monte Carlo simulations. We also measured the SNR difference between SM and diffuse beams for different depths, as seen in Figure 3.7. Finally, the SNR for a diffuse beam was measured as a function of the number of averages, and can be seen in Figure 3.8. It can be seen that SNR increase due to averaging cannot compete with SM imaging if using the same amount of averages as there are SM beams.

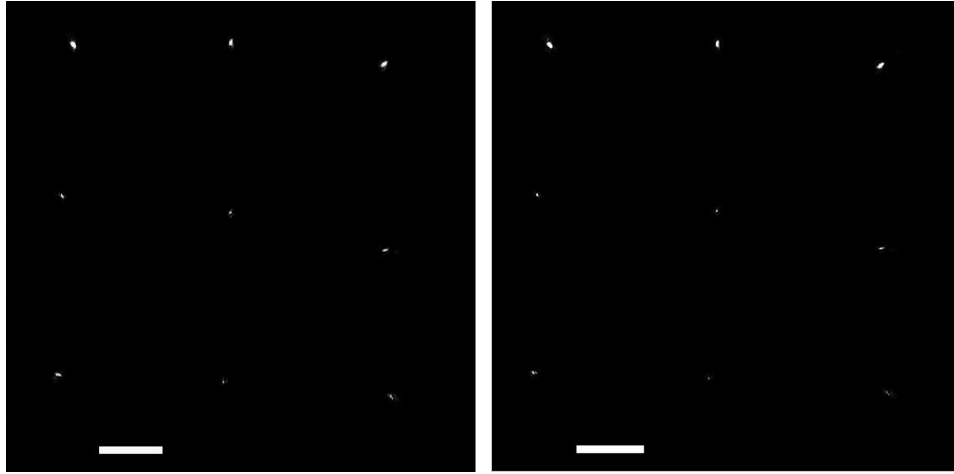


Figure 3.6: Hair phantom images with a diffuse beam (left) and SM beam (right).

### 3.5 Conclusion

We were able to verify SNR improvement in images using the SM light delivery technique, both in simulation and experimentally. This technique will increase the scalability for wide-area PAT from any laser system utilized, maximizing SNR without averaging.

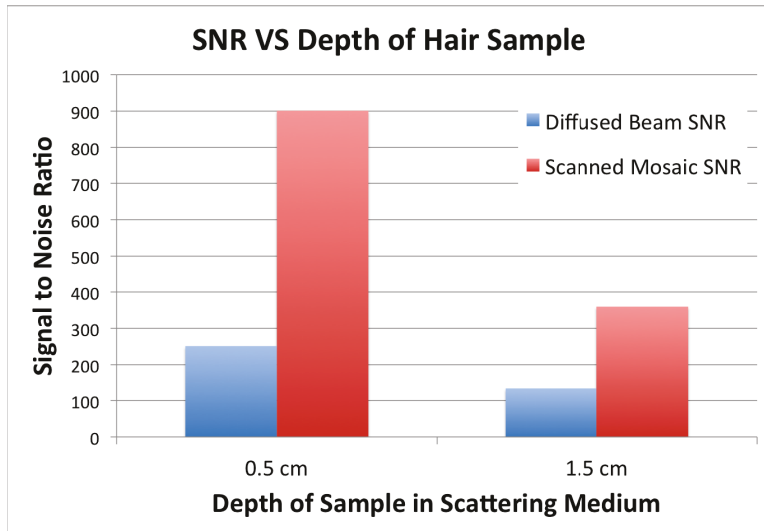


Figure 3.7: SNR comparison for diffused and SM beam at two depths.

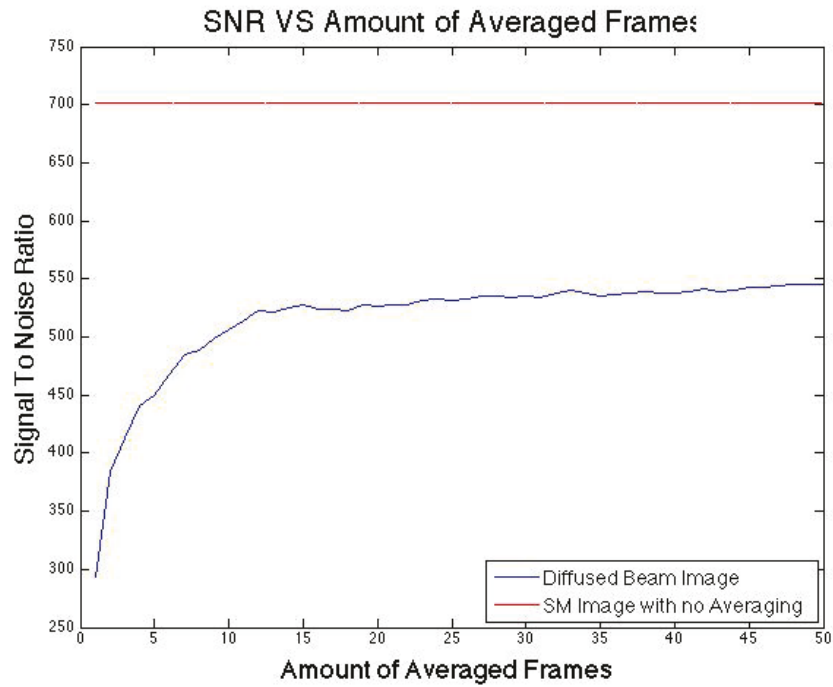


Figure 3.8: SNR for diffused beam with respect to the amount of averaging. This is compared to the unaveraged SM beam.

## Chapter 4

# S-sequence Enhanced Synthetic Aperture Ultrasound Scattering Tomography

### 4.1 Introduction

Photoacoustic Tomography (PAT) is an emerging hybrid imaging modality which provides optical absorption contrast with scalable ultrasonic spatial resolution [122, 124, 136]. Combined ultrasound and photoacoustic imaging is attractive as ultrasound provides structural context to the functional and molecular information provided by photoacoustic images [49, 54, 82, 87]. PAT has been implemented in many form factors, including linear arrays [31, 133], ring-transducer arrays [14, 30, 101, 127], and bowl-shaped detector geometries [57, 65]. Ring and bowl-shaped array geometries mitigate limited view artifacts associated with linear arrays. Despite many previous works regarding ultrasound transmission and reflection tomography [12, 22, 70, 80, 98, 103] and photoacoustic tomography [14, 38, 60, 97, 101, 124, 129], a combined system which achieves the ultrasonic diffraction limit has yet to be presented.

The goal of this paper is to introduce such a system and present an aperture encoding scheme to improve the signal-to-noise ratio of the ultrasound tomography images and automatically co-register with PAT images.

Recently high-frequency ultrasound-photoacoustic imaging systems have seen commercialization [79, 85]. Lateral and axial resolutions of  $30\mu m$  for 30-70 MHz transducers (with center frequencies around 50 MHz) provide detailed structural views for pre-clinical imaging applications [1, 64]. Tissue penetration, however, becomes much more challenging at higher frequencies. Photoacoustic-Ultrasound tomography with ring arrays has recently been introduced and promises isotropic in-plane resolution with a theoretical resolution limit of  $\sim 150\mu m$  for a 5 MHz array. This resolution is comparable to high-frequency array systems but enables deeper penetration and potentially higher sensitivity to large objects as photoacoustic signal frequency content is related to absorber size.

In the past few years, Merčep *et al.* have developed a reflection-mode, photoacoustic-ultrasound tomographic system using the synthetic transmit aperture (STA) technique with a 2-D, limited-view ring array [79, 80]. They utilized incoherent image compounding to boost their SNR, however this reduced the theoretical resolution of their system to 2x that dictated by the diffraction limit [80].

We introduce a photoacoustic-ultrasound tomography system which uses coherent, rather than incoherent, synthetic aperture compounding to meet the theoretical half-wavelength diffraction limit for ultrasound. Gemmeke and Ruiters [32] implemented such coherent STA reconstruction but did not implement photoacoustic tomography. One cost of the synthetic aperture approach, also seen in [32], is the limited signal-to-noise (SNR) ratio associated with transmitting on only one element at a time. To overcome this SNR challenge, we implement an S-Sequence aperture encoding technique previously introduced for linear arrays [39]. This technique will allow us to boost our SNR by  $\log_{10}(M + 1) - 1.5dB$  [139] without degrading our spatial resolution. In this paper, we will describe the theory and implementation of S-Sequence encoding and confirm that it will not affect the resolution of our system. Then, we will measure SNR improvement in ultrasound scattering

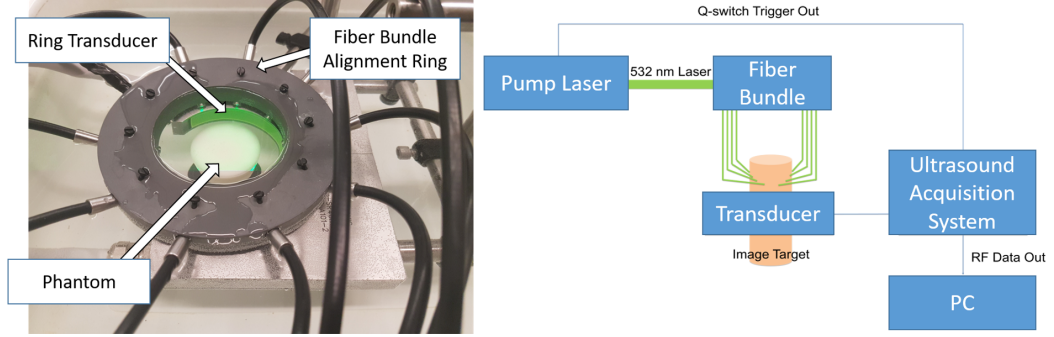


Figure 4.1: Schematic of UST and PAT system.

tomography (UST) using simple targets and tissue-mimicking phantoms. Finally, a composite PA-UST image will be presented.

## 4.2 Theory: S-Sequence Encoding

Spatial encoding for ultrasound arrays involve applying a weighting mask  $w_j^i$  on each transmitting element  $j$  for each transmit event  $i$ . After this weighting is applied for one transmit event, the observed signal  $p_k^i(t)$  can be described as:

$$\begin{bmatrix} p_1^i(t) \\ p_2^i(t) \\ \vdots \\ p_N^i(t) \end{bmatrix} = \begin{bmatrix} e_{11}(t) & e_{12}(t) & \cdots & e_{1N}(t) \\ e_{21}(t) & e_{22}(t) & \cdots & e_{2N}(t) \\ \vdots & \vdots & \ddots & \vdots \\ e_{N1}(t) & e_{N2}(t) & \cdots & e_{NN}(t) \end{bmatrix} \begin{bmatrix} w_1^i \\ w_2^i \\ \vdots \\ w_N^i \end{bmatrix} + \begin{bmatrix} n_1(t) \\ n_2(t) \\ \vdots \\ n_N(t) \end{bmatrix} \quad (4.1)$$

where  $e_{kj}(t)$  is defined as the received signal of element  $k$  from pulsing transmit element  $j$ , and  $n_k^i(t)$  is zero-mean additive noise. For M transmit events, this matrix can be expanded to:

$$\begin{aligned}
& \begin{bmatrix} p_1^1(t) & p_1^2(t) & \cdots & p_1^M(t) \\ p_2^1(t) & p_2^2(t) & \cdots & p_2^M(t) \\ \vdots & \vdots & \ddots & \vdots \\ p_N^1(t) & p_N^2(t) & \cdots & p_N^M(t) \end{bmatrix} = \\
& \begin{bmatrix} e_{11}(t) & e_{12}(t) & \cdots & e_{1N}(t) \\ e_{21}(t) & e_{22}(t) & \cdots & e_{2N}(t) \\ \vdots & \vdots & \ddots & \vdots \\ e_{N1}(t) & e_{N2}(t) & \cdots & e_{NN}(t) \end{bmatrix} \begin{bmatrix} w_1^1 & w_1^2 & \cdots & w_1^M \\ w_2^1 & w_2^2 & \cdots & w_2^M \\ \vdots & \vdots & \ddots & \vdots \\ w_N^1 & w_N^2 & \cdots & w_N^M \end{bmatrix} \\
& + \begin{bmatrix} n_1^1(t) & n_1^2(t) & \cdots & n_1^M(t) \\ n_2^1(t) & n_2^2(t) & \cdots & n_2^M(t) \\ \vdots & \vdots & \ddots & \vdots \\ n_N^1(t) & n_N^2(t) & \cdots & n_N^M(t) \end{bmatrix}
\end{aligned}$$

This can be written in matrix form:

$$\mathbf{P}(t) = \mathbf{E}(t)\mathbf{W} + \mathbf{n}(t) \quad (4.2)$$

In this context, STA imaging could be achieved if  $\mathbf{W}$  was equal to an identity matrix, in other words  $\mathbf{P}(t) = \mathbf{E}(t)$ . Thus, when using a more complex weighting matrix, STA image data can be recovered by calculating  $\hat{\mathbf{E}} = \mathbf{P}(t)\mathbf{W}^{-1}$ . By choosing a  $\mathbf{W}$  that uses transmits on more than one element per transmit event, the SNR can be increased by increasing the total energy per event. Consequently, for spatial encoding, it is important to use a  $\mathbf{W}$  that maximizes SNR improvement while minimizing error due to inversion. Suitable inversion error can be determined by finding a weighting matrix with  $\frac{\epsilon}{\sigma^2} = \text{tr}[\mathbf{W}^{-1}(\mathbf{W}^{-1})^T]$  that is as small as possible, where  $\sigma^2$  is the variance of the noise and  $\epsilon = \langle (\hat{\mathbf{E}} - \mathbf{E})(\hat{\mathbf{E}} - \mathbf{E})^T \rangle$  and  $\hat{\mathbf{E}} = \mathbf{P}(t)\mathbf{W}^{-1}$  is the recovered signal [139].

A popular weighting fitting this description is the Hadamard matrix [139]. For an  $M \times M$  Hadamard matrix  $\mathbf{H}_{2^N}$  (where  $M = 2^N$ ),  $\frac{\epsilon}{\sigma^2} = M + 1$ , which is acceptable [139]. It can be easily calculated using the Sylvester

construction technique, and easily inverted, where  $\mathbf{H}_{2^N}^{-1} = \frac{1}{2^N} \mathbf{H}_{2^N}$  [139]. The resulting noiseless SNR gain can be calculated as  $10 \log_{10}(M)$  (due to the fact that  $M$  times more transmit pulses are used per transmit event). The elements within this matrix are equal to either -1 or 1, thus it is dependent on the creation of a pulse that is an exact inverted copy of a positive pulse. In practice, this is difficult, for any inconsistencies between the inverted and positive pulses will severely degrade the efficacy of the inversion [139]. Therefore, we seek a weighting matrix that avoids the necessity of inverted pulses.

In this paper, we propose to use an S-matrix, a matrix derived from the Hadamard matrix made up of 1's and 0's. S-matrices ( $\mathbf{S}_{2^N-1}$ ) of order  $M = 2^N - 1$  are constructed by removing the first row and column of a Hadamard matrix  $\mathbf{H}_{2^N}$ , and replaces instances of 1's by 0 and instances of -1's by 1. Although this removes the necessity of inverted pulses, the non-zero elements per transmit event are halved. This will reduce the theoretical SNR improvement to  $10 \log_{10}(M+1) - 1.5dB$ , only 1.5dB less than the Hadamard. Regardless, the S-matrix inversion condition is  $\frac{\epsilon}{\sigma^2} = [2 - 2/(M+1)]^2$ , which is acceptable. It can also be easily inverted:  $\mathbf{S}_{2^N-1}^{-1} = \frac{1}{2^N} 2\mathbf{S}_{2^N-1}^T - \mathbf{J}$ , where  $\mathbf{J}$  is an appropriately sized matrix of ones.

Because the S-matrix avoids the difficulty of implementing inverted pulses with negligible SNR decrease, we opt to use this weighting matrix for our spatial encoding, which will heretofore be referred to as S-Sequence spatial encoding. This was applied by Harrison *et al.* for linear array imaging [39], but we illustrate its utility for improving SNR for UST.

### 4.3 Methods and Materials

A 5 MHz, 256-element,  $256^\circ$  ring array was used for our experiments (Imasonic SAS, France). Each element had a pitch of  $0.7mm$ , an inter-element spacing of  $0.1mm$  and a height of  $10mm$ . The bandwidth of this array was 55%, and toroidal elevation focusing has been applied. The elements themselves have been impedance matched to water. A Verasonics VDAS I ultrasound acquisition system (Verasonics Inc. Redmon, WA) was used

in conjunction with this transducer. This system can transmit on 256 elements, and receive on 128. We used a sampling rate of 20 MHz. The raw data collected was post-processed using MATLAB (The MathWorks Inc., Natick, MA). For the PA images, a 532 nm, 10 Hz laser was used (Surelite Continuum III). Light was delivered through a ten-legged fibre bundle (CeramOptec) situated around the transducer to produce a thin strip of illumination on the target. The laser fluence used in our experiments was set to  $20mJ/cm^2$ . The set-up schematic can be seen in Fig. 4.1.

To implementing S-Sequence spatial encoding, the rows of the S-matrix were used as an apodization function for the transmit elements. The resulting received signal is then decoded by multiplying it with the inverted S-matrix, recovering our STA image data. Due to issues caused by crosstalk between elements, only 63 elements were used for transmission, utilizing every fourth element in the array. Acquisition of data achieved a speed of  $\sim 150frames/s$  for both STA and S-Sequence methods when using 64 elements. For 50x averaging, acquisition of data reduced to  $1frame/sec$ . Thus, this amount of averaging can be done within a breath hold. Averaging was done before coherent compounding, but could also be done after, which may offer improved robustness to motion; a point that needs to be researched in the future. Data was transferred then decoded and reconstructed offline. An addition of parallel computing schemes and implementation of graphical processing units could allow real-time reconstruction rates, however this is left to future work [12, 56].

To reconstruct UST images, we implemented a delay-and-sum technique: distances were calculated from a receive element to the chosen pixel, and back to the transmitting element. Assuming a constant speed-of-sound, these distances were converted to time delays, allowing the appropriate signal information to be back-propagated to the respective pixel. The unscattered transmitted ultrasound signals, which propagate directly through the object, were removed from the received signal before back-propagation. The signal was then corrected for signal losses due to distance. Appropriate time gain compensation was then applied. This was repeated for each receive element, and then for each transmit event. As the reconstruction will contain

both positive and negative signals, we chose to take the magnitude of the reconstructed image for display.

A universal back-projection reconstruction algorithm was implemented [129] for photoacoustic image reconstruction. For the photoacoustic-ultrasound combined images, all 256 elements were used for receiving signals for both modalities. The Verasonics VDAS I system allows for 128-receive elements per acquisition, thus two laser pulses are necessary to receive data from 256-elements.

This PA-UST set up is similar to Merčep *et al.* [79,80], however the reconstruction techniques differ. For UST, we both implemented delay-and-sum techniques, however as stated previously, Merčep *et al.* utilized incoherent spatial-compounding, whereas we implemented S-Sequence encoding with coherent summation. For PAT, Merčep *et al.* used model-based inversion, which usually includes a deconvolution step that improves resolution. We used universal back-projection but did not include a deconvolution step.

## 4.4 Results

### 4.4.1 Resolution

#### UST Resolution

To characterize spatial resolution, an aluminum wire target (diameter =  $12.5\mu m$ , Secon Metals) was suspended in water, orthogonal to the imaging plane. Both STA and S-Sequence UST data were collected. Resolution was calculated by taking full width at half maximum (FWHM) of the wire targets at six different angles around the target. The wire was placed in seven different places within the imaging field. Close to the center, the resolution was calculated to be  $100 \pm 36\mu m$  for STA and  $119 \pm 37\mu m$  for S-Sequence imaging. As the wire moved from the center, the FWHM's increased. The average FWHM throughout the plane, however, was measured to be  $138 \pm 48\mu m$  for STA and  $139 \pm 44\mu m$  for S-Sequence, still comparable to the theoretical half-wavelength diffraction limit of our system, which is  $150\mu m$ .

To show the improvement over B-mode images, we compared the reso-

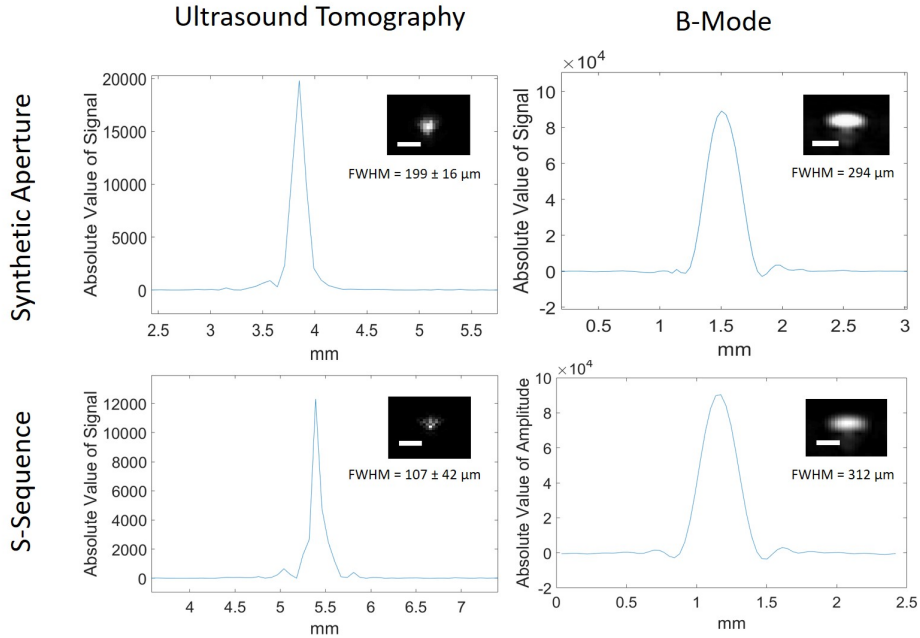


Figure 4.2: FWHM's of STA- and S-Sequence wire targets from both UST and B-Mode Linear Imaging. Scale bar is equal to 0.5 mm.

lution of our system to a 5 MHz, 128 element linear transducer (ATL L7-4, BroadSound Corporation) using both STA- and S-Sequence based imaging techniques on the same wire set-up. It can be seen in Fig 5.3 that B-mode image lateral resolution was about 2x larger than what we were able to achieve with UST, both when using STA and S-Sequence techniques.

While our UST resolutions does not quite compare to the high-frequency linear array counterparts (where they are able to achieve resolutions of  $30\mu m$  for a 50 MHz center frequency linear transducer), their penetration depth is limited owing to the high frequency attenuation. Our system, in contrast, easily images through a 5-cm tissue mimicking phantom achieving resolutions  $< 150\mu m$ .

We calculated our out-of-plane resolution by imaging a small needle lowered into the field-of-view of our system. An edge spread function was then formed, with which we calculated the out-of-plane FWHM by taking the

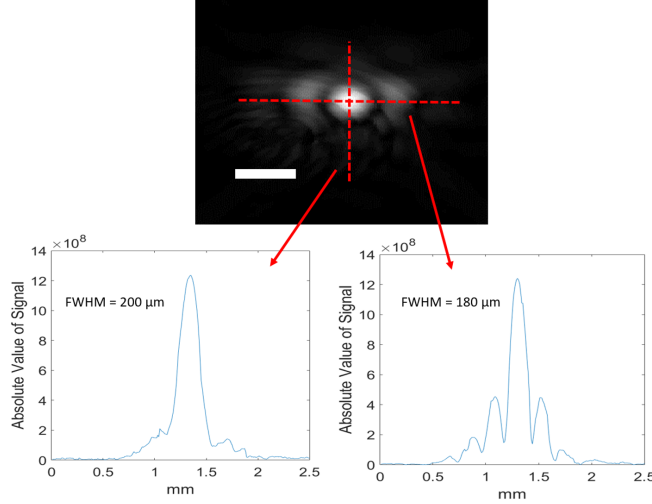


Figure 4.3: PAT resolution cross-sections with their respective point spread functions. Scale bar is equal to 0.25 mm

10% – 90% edge response. We found this to be equal to  $1.69\text{mm}$ , which is comparable to the predicted value of  $1.6\text{mm}$  (calculated as  $(1.4)(f\#)(\lambda) = (1.4)(3.7)(0.3\text{mm})$ ).

### PAT Resolution

PAT imaging resolution near the center of the imaging system was reported as  $180 \pm 32\mu\text{m}$ , comparable to a commercial counterpart [80]. FWHM's and an image of the wire target can be seen in Fig. 4.3. As with UST, PAT resolution degraded as the wire was placed farther away from the center of the transducer, with an average resolution of  $189 \pm 63\mu\text{m}$ .

#### 4.4.2 SNR improvement

To evaluate imaging performance of the UST system with STA and S-Sequence methods, three wires (diameter  $400\mu\text{m}$ ) were placed within a water bath normal to the transducer's imaging plane. These wire target images can be seen in Fig. 4.5. SNR was calculated as  $SNR = 20 \log_{10}(S_{max}/\sigma_{noise})$  where  $S_{max}$  is the maximum reconstructed signal amplitude of the wires and

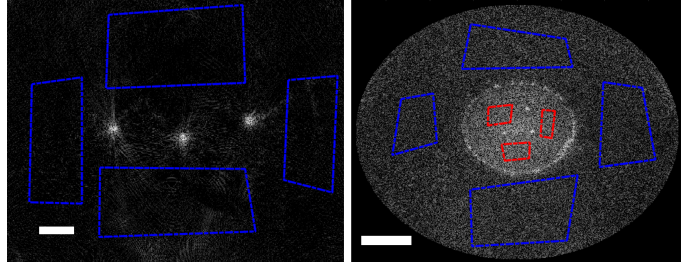


Figure 4.4: Noise kernels (blue) and CNR kernels (red) used for SNR and CNR calculation for wire experiment (left) and phantom experiment (right). Scale bar is equal to 5mm (left) and 10mm (right).

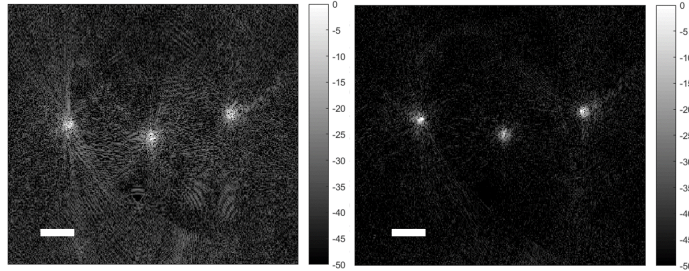


Figure 4.5: STA-UST (left) and S-Sequence UST (right) on wire targets, with a dynamic range of 50 dB for both images. Scale bar equal to 5 mm

$\sigma_{noise}$  is the standard deviation of the reconstructed noise. We used four noise kernels for SNR calculation, whose placement can be seen in Fig. 4.4. We were able to measure SNR as  $43.6 \pm 1.1dB$  for STA and  $53.2 \pm 1.3dB$  for S-Sequence, equalling an increase of  $9.6 \pm 1dB$ .

SNR improvement was also tested on issue mimicking phantoms. The phantoms consisted of three wires (diameter  $400\mu m$ ) placed within a small, 10% (w/w) cornstarch, 10% (w/w) gelatin phantom (diameter 3cm) that was placed at the center of the ring array. Clear gelatin was placed between this phantom and the ring array in order to ensure a more constant speed of sound. Salt water with a  $\sim 50g/L$  salinity could also enable this speed of sound matching [10, 52, 67]. STA-imaging and S-Sequence imaging were performed, both averaged 50x. We utilized four noise kernels and three CNR kernels, which can be seen in Fig. 4.4. Resulting images are shown with a

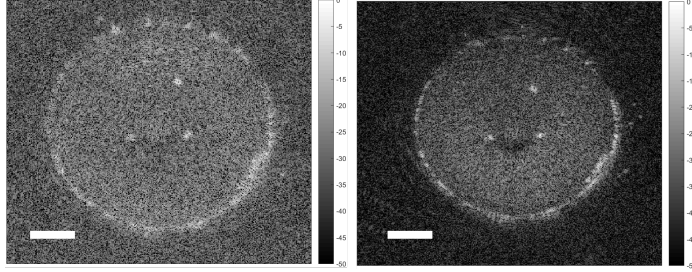


Figure 4.6: Ultrasound Tomographic images of wire phantom using (left) STA reconstruction and (right) S-Sequence reconstruction with a dynamic range of 50 dB for both images. Scale bar is equal to 5mm.

Table 4.1: CNR of red kernels in Fig. 4.4

CNR Kernel	STA	S-Sequence	Improvement
Top left	$-2.36 \pm 0.7dB$	$-0.99] \pm 0.5dB$	$1.4 \pm 0.2dB$
Bottom	$-1.86 \pm 0.6dB$	$0.67 \pm 0.3dB$	$2.5 \pm 0.4dB$
Right	$-2.4 \pm 0.7dB$	$0.0 \pm 0.4dB$	$2.4 \pm 0.4dB$

grey colormap in Figure 4.6.

For the phantom experiments, SNR was calculated as before. We were able to measure SNR as  $34 \pm 1dB$  for STA and  $45 \pm 1dB$  for S-Sequence; an SNR gain of  $11.2 \pm 0.3dB$ . We also calculated the contrast to noise ratio of both phantom images, which can be calculated as:  $CNR = |\mu_{roi1} - \mu_{roi2}| / \sqrt{\sigma_{roi1}^2 + \sigma_{roi2}^2}$ , with  $\mu_{roi1}$  signifying the mean inside of the phantom, and  $\mu_{roi2}$  the outside. The measured CNR values for the CNR kernel's seen in Fig. 4.4 can be seen in Table 4.1.

For 63 transmitting elements, the theoretical SNR improvement is calculated to be  $16.6dB$ . Similar to Harrison *et al.* [39], we were unable to achieve the theoretical S-Sequence SNR-enhancement for both the wire targets and the phantom experiment. This may be due to acoustic crosstalk (which we verified when using all elements rather than only 64). It could also partly be attributed to element-to-element pulse differences not accounted for by the S-matrix decoding steps.

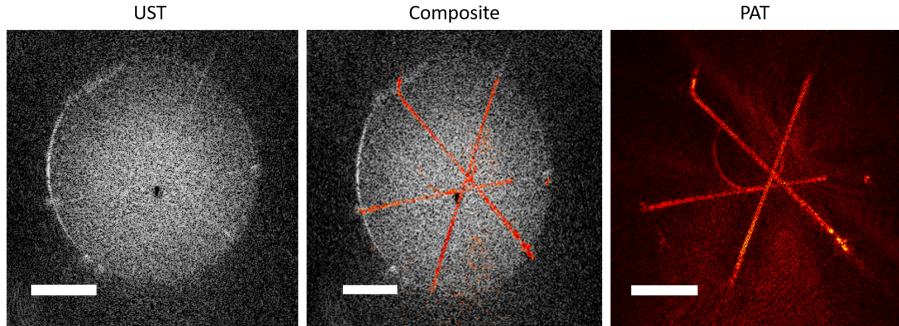


Figure 4.7: Ultrasound (left), photoacoustic (right), and photoacoustic/ultrasound (centre) composite tomographic images of hair phantom. Red colormap signifies photoacoustic data and greyscale colormap signifies ultrasound data. Scale bar equal to 5 mm.

#### 4.4.3 PAUS Composite Imaging

A tissue-mimicking hair phantom (10%w/w gelatin, 10%w/w cornstarch) was created for PAUS composite imaging using 532nm light. Previous research has shown that cornstarch phantoms act as both an optical and ultrasound scatterer, with an optical scattering coefficient of  $\mu'_s = 9.2\text{cm}^{-1}$  [50, 138]. A water bath was used as a medium. A PA-US composite image can be seen in Figure 5.5, with the photoacoustic data realized with the red colormap, and the ultrasound image consisting of a log-scale grey colormap with a dynamic range of 40dB. Both UST and PAT were averaged 50x (using 50 acquisitions for UST, and 100 pulses for PAT). It can be seen in Fig. 5.5 that the hairs are obfuscated by the scattering tissue in the UST image, but can be clearly seen in the PAT image.

### 4.5 Conclusion

In conclusion, we were able to demonstrate the proficiency of S-Sequence spatial encoding as a method to boost SNR for STA-based ultrasound tomography reconstructions. Fully-coherent STA ultrasound tomography, with and without including the spatial encoding scheme, achieved resolutions that

rivaled the theoretic diffraction limit. The combined ultrasound and photoacoustic tomography system may enable new functional and molecular imaging studies in preclinical arenas.

## Chapter 5

# Ultrasound Scattering Anisotropy Visualization with Ultrasound Tomography

### 5.1 Introduction

Ultrasound scattering can be characterized as either isotropic (where scattering signal is constant for any angle around a scatterer) or anisotropic (where this signal is a function of the angle between the transmitted pulse and the receiving angle). This anisotropy is caused by a few different parameters, including geometry, size of the scatterer, the scatterer's structural components, and the contrast of its density and compressibility versus its surroundings [18]. For most ultrasound imaging modalities, the directionality of the scattered signal is ignored during analysis, however this directionality may provide new, useful clinical information [45, 94, 113, 115]. A handful of studies have explored scattering anisotropy previously. These studies, however, implemented very limited angle spans (ranging from  $10^\circ$  [37] total to  $60^\circ$  [45] total), restraining the available anisotropic data uncovered. They also uti-

lized single element [115] or linear array transducers [37, 45], which caused the resulting images to have low lateral resolution and limited-view artefacts. Finally, studies were forced to pair their transmit and receive pulse angle, so that anisotropic scattering information from a specific transmit angle was only acquired from one specific receive angle. The information obtained is therefore restricted to a small percentage of the total anisotropic scattering profile of an ultrasound scatterer. The goal of this paper is to showcase a novel way of visualizing ultrasound scattering anisotropy by using a synthetic transmit aperture (STA) ultrasound tomography (UST) system, an ultrasound modality that has gathered a growing amount of interest in the last few decades [24, 79, 99, 103]. Our system is capable of a  $256^\circ$  view surrounding the target using a ring array, and can produce images with a resolution comparable to the half-wavelength diffraction limit. Furthermore, our system can be used to investigate scattering anisotropy and is sensitive to the scattered field from targets interrogated with a sequence of transmit angles independent of the receive-element angle. This will provide new, previously unattainable information such as anisotropic scatterer orientation at high resolution.

Vogt *et al.* analyzed a range of angular A-scans from a single-element transducer to differentiate scar tissue on skin, to visualize borders between the dermis and subcutaneous fat, and to characterize atherosclerosis [115]. Anisotropy has also been visualized by fitting backscattered linear array data onto a reflection model, albeit with limited-view artefacts [45]. Ijaz *et al.* used the Phong reflection model to separate diffuse and specular (or anisotropic) backscatter, and visualized the specular backscatter with a vector field plot [45]. Both experiments used data collected for spatial compounding purposes. Therefore, the span of angles collected ( $60^\circ$  from Vogt *et al.* and  $30^\circ$  from Ijaz *et al.* [45, 115]) was limited. Moreover, the backscattered angle received by the transducers had to match the angle of the transmitted pulse due to the fact that the transducer’s position was fixed for each acquisition. While their systems were capable of measuring structural anisotropy due to non-spherical scattering geometry, they were unable to do this with diffract-limited spatial resolution, which is possible

with our system. Additionally, inability to use different transmit and receive angles precluded measurement of scattering anisotropy from radially symmetric scatterers [18, 118], theoretically possible with our system.

Walker and McAllister investigated scattering anisotropy in order to decouple density and compressibility from radially symmetric scatterers [116]. By implementing a strategic transmit and receive apodization for a fixed transducer array, scatter anisotropy information was estimated using D-weighting, a method that involves taking the difference of an image acquired at some scattering angle (other than backscatter) from the backscatter image [116]. Although fixing the transducer simplifies the experimental set-up, the angular span attained reached only  $10^\circ$ , severely limiting the scope of the collected data [37]. Furthermore, while their approach can provide an image weighting for non-isotropic scatterers, their approach was not able to determine principal scatter orientation. Finally, this method was also unable to reach resolutions that came close to the diffraction limit [37].

Finally, Kretzek *et al.* investigated anisotropy of targets with specular reflections as a means to better increase the contrast of their 3D ultrasound tomographic images for breast evaluation [55]. By investigating the reflected ultrasound wave from each voxel and determining which angle gave the highest backscatter, they were able to use this information to increase the contrast of their images by 32%. They further state hopes to use this reflectivity information to characterize tissue in a novel way. Similar to Vogt *et al.* and Ijaz *et al.*, anisotropy was calculated by investigating the changing reflectivity of surfaces. Our approach, however, focuses on ultrasound scattering anisotropy, including targets that are equal to or smaller than the acoustic wavelength.

In this paper, anisotropic visualization using STA-UST was evaluated by imaging phantoms comprised of iron filings aligned to a magnetic field. The size of these filings range from  $20 \mu m$  to  $0.3 \text{ mm}$ , and are of random shape. This is equal to and smaller than our ultrasound wavelength (which is  $\sim 300 \mu m$  for a 5 MHz centre frequency). By measuring the scattering anisotropy through observing the ultrasound response of the iron filings for different transmit angles, we propose our reconstruction method can be used

to determine the directional orientation of these filing. We also extended this approach to visualize the direction of "wire tract" within a phantom. We are able to do this with near-diffraction limited performance and with an angular range of  $256^\circ$ , unlike previous methods.

## 5.2 Methods and Materials

A 5 MHz, 256-element,  $256^\circ$  ring array was used for our experiments (Imasonic SAS, France). Each element had a pitch of  $0.7mm$ , an inter-element spacing of  $0.1mm$  and a height of  $10mm$ . The bandwidth of this array is 55%, and toroidal elevation focusing has been applied. The elements themselves have been impedance matched to water. A Verasonics VDAS I ultrasound acquisition system (Verasonics Inc., Redmon, WA) was used in conjunction with this transducer. The raw data collected was post-processed using MATLAB (The MathWorks Inc., Natick, MA).

UST images were reconstructed using an STA delay-and-sum reconstruction approach [32, 80]. One element transmits an ultrasound pulse that is received by all elements. This is repeated until all elements have transmitted once, producing backscatter information for each receive element with respect to each transmit element. To reconstruct a scattering image for one transmit event, received signals are time-reversed through the imaging plane and corrected for distance attenuation. These images are then coherently summed over all transmit events to produce the final UST image. This allows for transmit and receive focusing, producing approximately isotropic resolutions comparable to the acoustic diffraction limit of the system. Acquisition of data achieved a speed of  $\sim 40frames/s$ . Data was transferred and reconstructed offline. With the addition of parallel computing schemes and implementation of graphical processing units, real-time reconstruction rates may be possible, although this is left to future work [12, 56].

To estimate scattering anisotropy, we evaluated angular dependence of reconstructed signals for each pixel as a function of incident transmit angle. The maximum scattering intensity associated with an incident transmit angle was used to determine the principal scattering angle for each pixel,

similar to the method done in [55]. A 4x4 median filter was then applied to the 2D map of the resulting angles associated with each principal scattering direction. After this, the filtered scattering angle map was used to delineate the direction of arrows in a vector field. The length of each arrow was determined by the difference between the maximum and the mean of the signal. Vector field images were created by using the quiver plot function in MATLAB.

This method provides an arrow for each pixel in the image, however to display this many arrows makes visualization challenging. Thus, noisy arrows from the gelatin background were removed by thresholding the vector field plot image with respect to final UST image intensity. Theoretically, magnetically-aligned iron filings will give the strongest backscatter when the transmitted wave is orthogonal to the direction of the filings. Thus, by rotating the direction of each arrow by  $90^\circ$ , the direction of the arrows should coincide with the direction of the iron filings, which should match the direction of the magnetic field lines. Fig. 5.1 displays a plot of intensity with respect to transmit angle for the iron filing experiment described below. The transmit angle for the x-axis was determined arbitrarily, however what is important to note is that for intensity measurements  $90^\circ$  away from the transmit angle corresponding to the maximum intensity (for our case,  $180^\circ$ , pictured as the 1st inlet in Fig. 5.1), we measure very low signals (pictured as the 2nd inlet in Fig. 5.1). This maximum signal was measured when the transmit angle was perpendicular to the fibre orientation.

It is also important to note that our methods are trying to approximate a three-dimensional problem within a two-dimensional scope. The following experiments limit the dimensionality into a plane (where all ultrasound targets scatter anisotropically within the 2D plane of our transducer) to maximize our results. Future work will be done to extend this method into three dimensions.

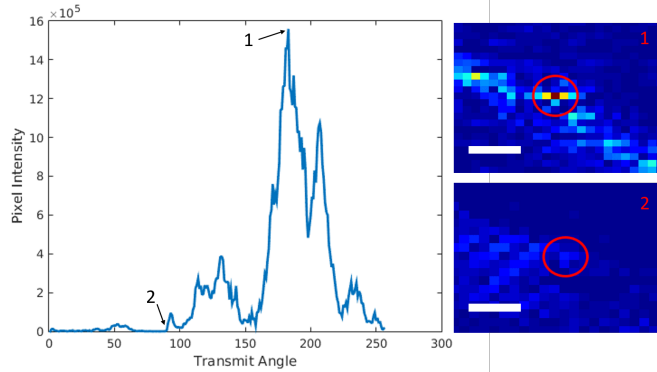


Figure 5.1: (Left) A plot of intensity with respect to transmit angle for a pixel in the iron filing experiment described below, seen in Fig 5.5. (Right) Images of the aforementioned pixel at two angles with a  $90^\circ$  difference. Length bars are 0.5 mm long.

## 5.3 Results

### 5.3.1 Resolution

To characterize spatial resolution, an aluminum wire target (diameter =  $12.5\mu m$ , Secon Metals) was suspended in water, orthogonal to the imaging plane. Resolution was calculated by taking the mean full-width at half-maximums (FWHMs) of point spread functions from six different angles around the wire image. To investigate the potential shift-variance of the point spread functions, we quantified resolution of wire targets located at various positions within the transducer's field-of-view, as seen in Fig. 5.2. The corresponding FWHMs for each wire can be seen in Table 5.1. Near the centre, we were able to achieve a resolution of  $100 \pm 36\mu m$ , but as the wire came closer to the edges, the FWHM increased. On average, resolution was measured as  $138 \pm 48\mu m$ , which closely compares to the theoretical half-wavelength resolution of  $\sim 150\mu m$ . Because we are using a limited-view ring transducer with elements that have a large area, resolution does vary within the imaging field-of-view. Model-based inversion approaches have been investigated to mitigate these problems in previous work [15, 71, 112] which could be applied in our future efforts.

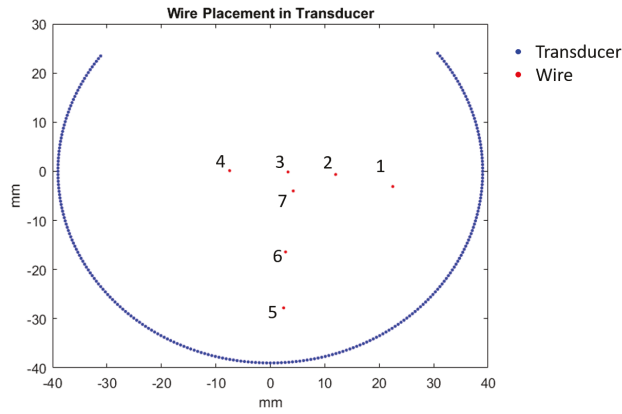


Figure 5.2: Wire Placements within the Ring Transducer for Resolution Measurement.

To understand this improvement over a linear transducer counterpart, a B-Mode image was captured with a linear transducer with a centre frequency of 5 MHz and 128 elements (ATL L7-4, Broadsound Corporation) using a synthetic-transmit aperture imaging scheme. The lateral FWHM was measured to compare with the UST result. The results in Fig. 5.3 demonstrate that, at equal frequencies, UST is able to achieve resolutions half as small that of the linear transducer.

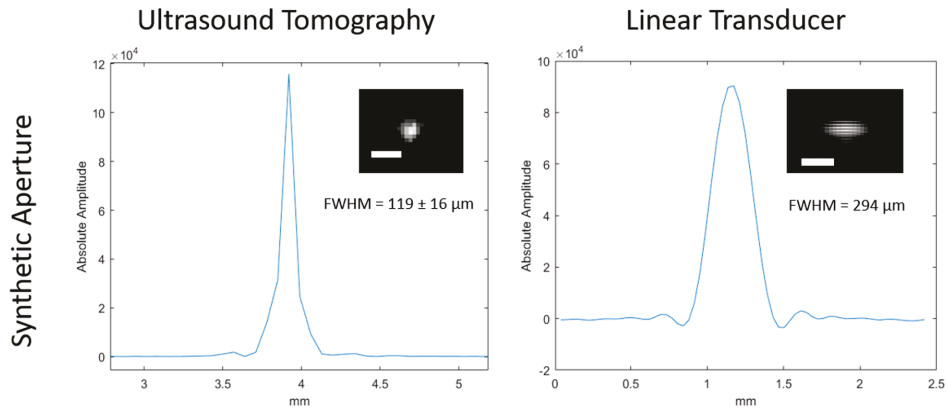


Figure 5.3: UST VS Synthetic Aperture Backscatter Image with a linear transducer. Scale bars are equal to 0.5 mm in length.

Table 5.1: FWHM in  $\mu m$  of Wires in Fig. 5.2

Wire	FWHM	Wire	FWHM
1	$209 \pm 50$	5	$167 \pm 92$
2	$95.8 \pm 26$	6	$114 \pm 53$
3	$100 \pm 36$	7	$119 \pm 16$
4	$164 \pm 64$		

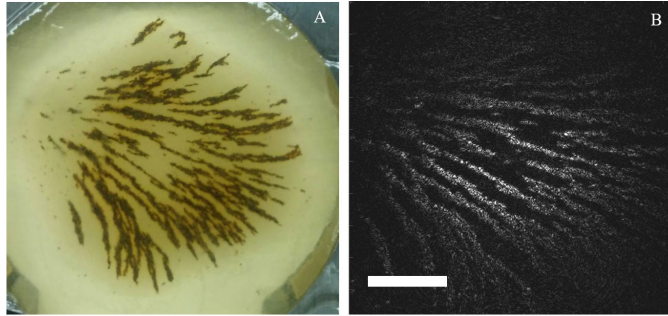


Figure 5.4: A) Iron filing phantom encased with a gelatin medium within ring-array transducer. B) UST image of iron filings. Scale bar indicates 1 cm.

### 5.3.2 Anisotropy Visualization

A 10% $w/w$  (weight gelatin by weight water) porcine skin gelatin phantom was generated. Iron filings were placed within the gelatin and aligned with a bar magnet (seen in Fig. 5.4a). Gelatin was then used as an acoustic medium between the phantom and the transducer in order to ensure a more constant speed of sound. Fig. 5.4b is the resulting UST image captured by our system.

Fig. 5.5 includes the anisotropy quiver images superimposed onto the UST image shown above. It can be seen that the arrows follow the direction of the iron filings as determined by the magnetic field.

An analysis of arrow direction was implemented where, for certain regions of interest (ROI, see Fig. 5.5), the calculated arrow direction was compared to the visible direction of the iron filings. As seen in Table 5.2, the measured directions are within error of the magnetic field lines (as delin-

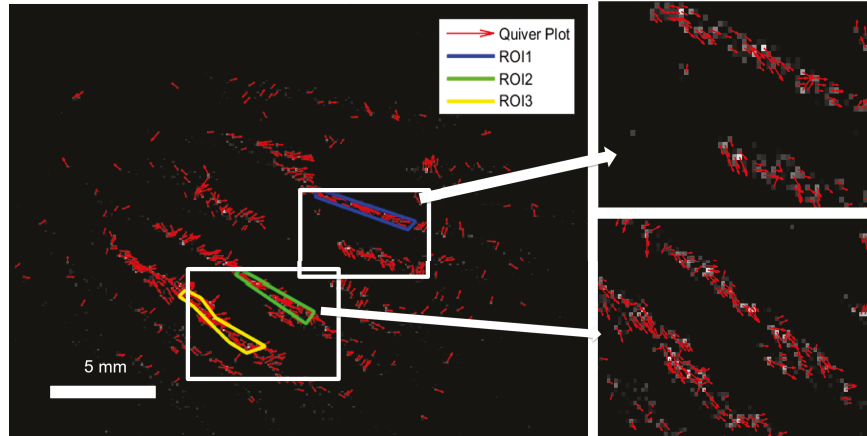


Figure 5.5: Anisotropy vector field plot image superimposed onto UST image. Scale bar indicates 5 mm.

Table 5.2: ROI Calculations for Fig. 5.5

ROI	Visual Angle	Measured Angle
ROI 1	$19.0^\circ$	$21.9^\circ \pm 3.3^\circ$
ROI 2	$31.7^\circ$	$27.0^\circ \pm 2.8^\circ$
ROI 3	$35.6^\circ$	$32.0^\circ \pm 3.1^\circ$

eated from images manually, under the heading "Visual Angle"). Standard error was used for uncertainty calculations.

To investigate whether thresholding impacted quantitative analysis of principal scattering directions, we investigated threshold levels of 30%, 50%, and 80% of our original thresholding value. We found that the mean principal scattering directions changed less than 3.5%.

Another anisotropic experiment was conducted with a curled copper wire (diameter  $400\mu m$ ) placed within a 10%w/w (weight gelatin by weight water) porcine skin gelatin phantom, which can be seen in Fig. 5.6. Vector field plots corresponding to this wire can be seen in Fig. 5.7, which displays arrows following the direction of the wire.

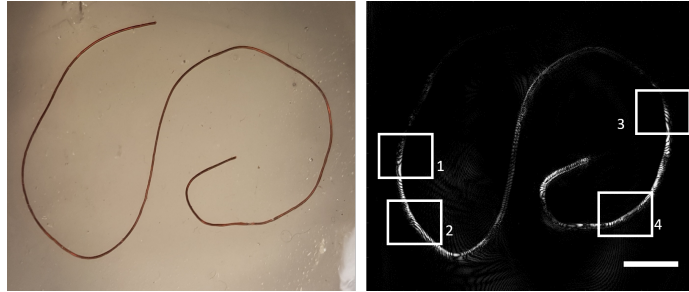


Figure 5.6: Wire target in gelatin, and the UST image corresponding to this target. Scale bar is 1 cm long. Boxed areas on the right image correspond to the zoomed in images in Fig. 5.7.

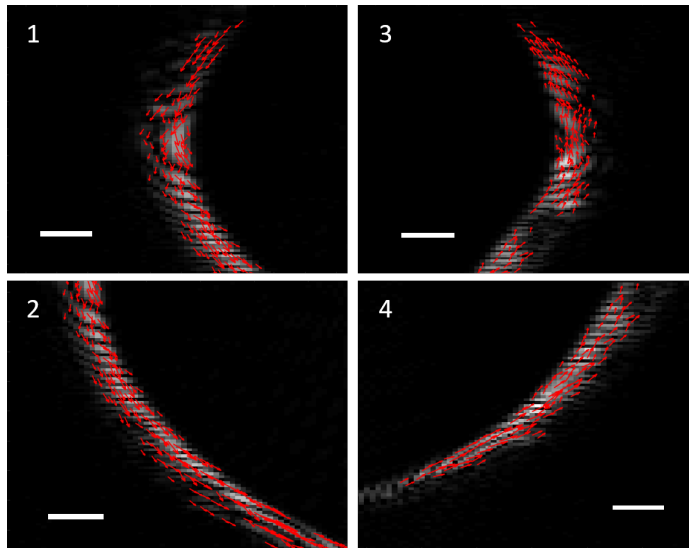


Figure 5.7: Anisotropic visualization of a Copper Wire in Gelatin. Scale bar is equal to length of 1 mm.

## 5.4 Conclusion

In this paper, we introduce a new application of ultrasound tomography imaging: the visualization of ultrasound scattering anisotropy. In most ultrasound imaging modalities, scattering anisotropy is usually ignored, however it may provide new, useful clinical information. This information may impact tissue characterization, offer stronger visualization of borders, and

improve assessment of fibre orientations, giving an ultrasonic analog to Magnetic Resonance Imaging tractography [45,115]. This paper introduces such a system capable of visualizing the direction of iron filings aligned to a magnetic field as a proof of principle. In future work, we hope to extend this research by investigating ultrasound scattering anisotropy due to differences in the density and compressibility of ultrasound scatterers, providing a new way of characterizing these parameters [118,119] and potentially providing new means of visualizing microcalcification in breast cancers.

## Chapter 6

# Compressibility and Density Weighting for Ultrasound Tomography Imaging

### 6.1 Introduction

The directionality of ultrasound scattering is often ignored in conventional ultrasound imaging. Essentially, most ultrasound imaging techniques assume all scatter to be isotropic (i.e., that the scattered signal is independent on the direction of the transmitted wave). Physically, however, this is not always the case. Anisotropic scattering (where the scattered signal is a function of the direction at which the transmitted wave hits the scatterer) may be caused by a number of physical attributes of the scatterer: its shape, its size, its structural components, and its compressibility and density contrast with the media in which it is suspended [18]. Information due to anisotropic scattering may provide new, useful clinical information [94, 115, 117], which has influenced many groups to research this phenomenon.

Many of these groups focused on measuring anisotropy through the directivity of reflected ultrasound pulses, which is mainly based on geometry and size of the imaged target. This was achieved by using single-element [115], linear array [45], and cylindrical array transducers [55], in hopes to bet-

ter visualize tissue boundaries. Methods included measuring differences in backscatter intensity at different transmit/receive angles [115], and numerical modeling of specular reflections [45]. Kretzek *et al.* developed a method of evaluating directional reflectivity for their 3D ultrasound tomography system [55] to produce higher tissue contrasts. The motivation for these groups was to improve tissue differentiation due to macroscopic structural and geometric specificities in certain tissue, and did not focus on anisotropy caused by material properties such as density and compressibility. Furthermore, these systems are intrinsically incapable, due to low resolution or transmit/receive coupling, to record anisotropy due to small, spherically symmetric scatterers.

Yamanaka *et al.* developed a point-scatter index for each pixel in a sequence of angularly compounded images. They were able to significantly suppress the anisotropic scattering signals from background tissue while enhancing microcalcification-mimicking targets [132]. Their approach, however, focused on the suppression of any signal that was not isotropic (and thus could not provide compressibility and density differentiation), and their system could not achieve diffraction-limited performance [132].

A method to visualize the anisotropy due to material properties of spherically-symmetric scatterers was proposed by Walker *et al.*, who utilized a linear array transducer and a specific transmit apodization technique to decouple density and compressibility signal in ultrasound images [117]. Their system, however, had low lateral resolution, high side-lobe artifacts, and a limit angular span [36, 117].

In this paper, we propose a novel reconstruction technique for ultrasound tomography that differentiate density and compressibility signal for the case of radially-symmetric ultrasound scatterers. This system is capable of isotropic, diffraction-limited resolution that can produce compressibility- and density-weighted images. We test the capabilities of this system with phantom experiments.

## 6.2 Theory

### 6.2.1 Compressibility and Density Decoupling

Radially-symmetric ultrasound scatterers exhibit both isotropic and anisotropic scattering when the compressibility and density of the scatterer is different than that of the surroundings. Compressibility differences give isotropic, monopole scattering. This is caused by the scatterer compressing and depressing when hit by an ultrasonic wave, producing spherical scattering waves. Density differences produce anisotropic, dipole scattering. This can be attributed to the scatterer shaking back and forth in the direction of the ultrasonic wave, producing scattering waves with a cosine weighted response, which you can see in Figure 6.1. The scattering angle - in other words, the angle made between the transmit element, the receiving element, and the scatterer (see Fig. 6.1) - will effect what information is gathered for a certain scan.

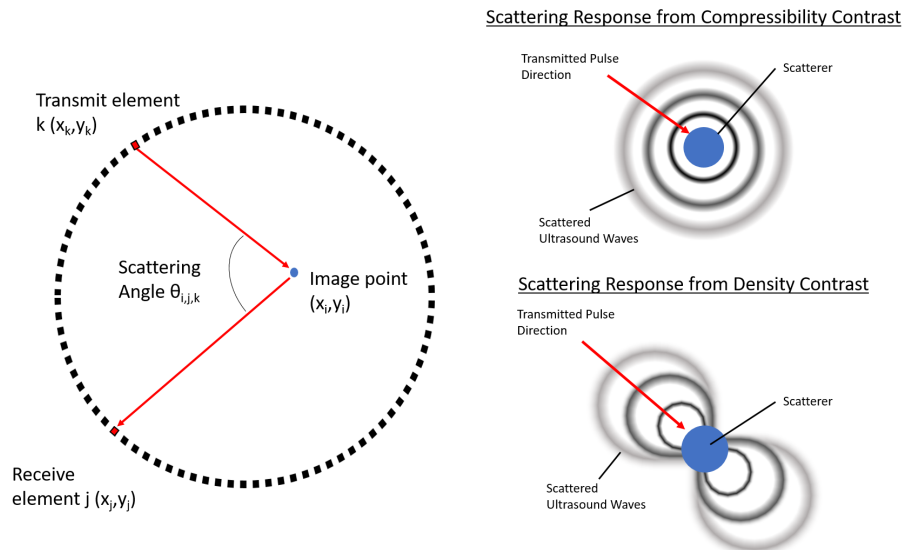


Figure 6.1: (Left) Schematic of Ring-Array Transducer. (Right) Scattering profiles of compressibility contrasted ultrasound scatterer (top), and density-weighted contrast scatterer (bottom)

Mathematically, a compressible spherical ultrasound scatterer will produce scattered pressures that can be approximated as:

$$p(r, \theta) \approx p_{im} e^{-jk_0 r} \frac{k_0^2 a^3}{3r} \left[ \frac{\kappa_v - \kappa_o}{\kappa_o} + \frac{3(\rho_v - \rho_o)}{2\rho_v + \rho_o} \cos(\theta) \right] \quad (6.1)$$

where  $p(r, \theta)$  is the pressure at distance  $r$  for scattering angle  $\theta$  with respect to the target,  $\kappa$  and  $\rho$  are the compressibility and density of either the target (delineated with subscript  $v$ ) or the surroundings (delineated with subscript  $o$ ),  $k_0$  is the wavenumber of the system,  $a$  is the radius of the scatterer, and  $p_{im}$  is an arbitrary constant. This equation assumes far field ( $k_0 r \gg 1$ ) and small scatterer ( $k_0 a \ll 1$ ) approximations.

For UST reconstruction, we implement a delay-and-sum (DAS) technique: one element is used for transmitting an ultrasound pulse and all elements are used to receive the resulting scattered signal. For transmitting element  $k$  at vector position ( $\mathbf{r}_k$ ) and receiving element  $j$  at vector position ( $\mathbf{r}_j$ ) in the image space  $I(\mathbf{r}_i)$ , the resulting A-scan for this transmit-receive pair will be labeled  $A_{k,j}(t)$ . To create a DAS image  $I(\mathbf{r})$ , A-scans are time-delayed and summed coherently for all transmit-receive pairs at every position in the image space. For a point  $\mathbf{r}_i$ , a time delay  $\tau_{i,j,k}$  for a specific transmit-receive pair ( $k, j$ ) can be calculated as

$$\tau_{i,j,k} = \frac{1}{c_0} \left( \sqrt{(x_i - x_k)^2 + (y_i - y_k)^2} + \sqrt{(x_i - x_j)^2 + (y_i - y_k)^2} \right) \quad (6.2)$$

where  $\mathbf{r}_i = x_i \hat{\mathbf{x}} + y_i \hat{\mathbf{y}}$  for a 2-D image. To calculate the value of pixel at point ( $\mathbf{r}_i$ ) in image space, the DAS algorithm can be formulated as:

$$I(\mathbf{r}_i) = \sum_k \sum_j A_{j,k}(t = \tau_{i,j,k}) \quad (6.3)$$

For a spherical ultrasound scatterer at  $\mathbf{r}_n$  in the object space, the pressure measured at receive element ( $\mathbf{r}_j$ ) can be described with equation 6.1. By applying accurate distance attenuation compensation to counteract the  $r$  dependence, equation 6.1 can be written in terms of  $\mathbf{r}_n$  (the position of

the scatterer in object space) and  $\theta_{n,j,k}$ , as seen in Figure 6.1. This pressure value determines the respective A-scan value at time delay  $\tau_{i,j,k}$ . For this scatterer, we can formulate an A-scan for a specific transmit-receive pair as:

$$A_{j,k}(t) = p(\mathbf{r}_n, \theta_{n,j,k})\delta_{n,j,k}(t - \tau_{n,j,k}) + n(t) \quad (6.4)$$

Therefore, to calculate the value of pixel ( $\mathbf{r}_i$ ) in the image space  $I$  for one scatterer, we must plug in equation 6.4 into equation 6.3:

$$I(\mathbf{r}_i) = \sum_k \sum_j p(\mathbf{r}_n, \theta_{n,j,k})\delta_{n,j,k}(\tau_{i,j,k} - \tau_{n,j,k}) + n(\tau_{i,j,k}) \quad (6.5)$$

where  $n(t)$  is zero-mean white noise. When  $\tau_{i,j,k} = \tau_{n,j,k}$ , equation 6.5 will have a nonzero value equaling  $p(\mathbf{r}_n, \theta_{n,j,k}) + n(\tau_{i,j,k})$ .

For image pixels corresponding to scatterer positions ( $\mathbf{r}_i = \mathbf{r}_n$ ),  $\tau_{i,j,k} = \tau_{n,j,k}$  for all  $j, k$  transmit-receive pairs. Therefore, the  $p_n$  values will constructively sum, leaving a high-intensity pixel. However,  $\tau_{i,j,k}$  can equal  $\tau_{n,j,k}$  even if  $\mathbf{r}_i \neq \mathbf{r}_n$  for a small number of  $j, k$  pairs. In this case, summing through all pairs will mostly be destructive, thus leaving a much lower pixel intensity. Through this process, a final DAS image is created. This allows us to image multiple scatterers - through the DAS process, positions in the image space with high intensities will correspond to scatterer positions in the object space. However, this method will cause image artifacts near the scatterer positions (as seen in CT, photoacoustic and conventional ultrasound [72, 131]). Despite this, we will assume the case of  $\mathbf{r}_i = \mathbf{r}_n$  in the image space  $I(\mathbf{r}_i)$  when  $\tau_{i,j,k} = \tau_{n,j,k}$  for the following discussion.

For UST, circular array geometries can be used. If we consider one transmit event  $k$ , it can be seen that every receiving element will correspond to a unique  $\theta_{i,j,k}$ . Furthermore, if we assume we use  $360^\circ$  circular array transducer, the receive elements will correspond to a  $\theta_{i,j,k}$  that spans  $[0, 2\pi]$ . For simplicity, if we are reconstructing at point ( $\mathbf{r}_i$ ) for transmitting element  $k$ , let us redefine  $\theta_{i,j,k}$  as  $\theta_{j|i,k}$ . Within this framework,  $\tau_{i,j,k}$  is also a function

of  $j$ , and thus can be described as a function of  $\theta_{j|i,k}$  for zero-mean noise  $n(\tau_{i,j,k})$ . When  $\tau_{i,j,k} = \tau_{n,j,k}$ , we can reformulate equation 6.5 for a single transmit event as:

$$\begin{aligned} I_{k,\kappa}(\mathbf{r}_i) &= \sum_{j=1}^M p_n(\mathbf{r}_i, \theta_{j|i,k}) + n(\theta_{j|i,k}) \\ &= \sum_{j=1}^M P_0(\mathbf{r}_i) \left[ \gamma_\kappa + \gamma_\rho \cos(\theta_{j|i,k}) \right] + n(\theta_{j|i,k}) \end{aligned} \quad (6.6)$$

where  $P_0(\mathbf{r}_i) = p_{im} e^{-jk_0 \mathbf{r}_i} k_0^2 a^3 / 3\mathbf{r}_i$ ,  $\gamma_\kappa = (\kappa_v - \kappa_o) / \kappa_o$ ,  $\gamma_\rho = 3(\rho_v - \rho_o) / (2\rho_v + \rho_o)$  and  $M$  is the number of receive transducers.

It can be seen that equation 6.6 is very mathematically similar to a Riemann Sum of  $p(\mathbf{r}_i, \theta_{j|i,k})$  over a range of  $\theta_{j|i,k}$ . Riemann Sums can be used to calculate approximate solutions for definite integrals. Therefore, for a  $\theta = [0, 2\pi]$ , equation 6.6 can be written as:

$$\begin{aligned} I_{k,\kappa}(\mathbf{r}_i) &= \int_{\theta=0}^{2\pi} [p(\mathbf{r}_i, \theta) + n(\theta)] d\theta \approx \\ &\int_{\theta=0}^{2\pi} P_0(\mathbf{r}_i) \gamma_\kappa d\theta + \int_{\theta=0}^{2\pi} P_0(\mathbf{r}_i) \gamma_\rho \cos(\theta) d\theta + \int_{\theta=0}^{2\pi} n(\theta) d\theta \\ &\approx P_0(\mathbf{r}_i) \gamma_\kappa 2\pi \end{aligned} \quad (6.7)$$

Therefore, for a ring array transducer spanning  $360^\circ$  around the object, delay-and-sum summation will produce images that are dependent on compressibility difference of spherical scatterers with their surroundings ( $\gamma_\kappa$ ) for each transmit event  $k$  at imaging point  $I(\mathbf{r}_i)$ .

To recover density differences ( $\gamma_\rho$ ), we apply a cosine-weighting to each summation term of equation 6.6. This will force the  $\gamma_\kappa$  integral to approach zero, while producing a non-zero integral term for  $\gamma_\rho$ . Specifically:

$$\begin{aligned}
I_{k,\rho}(\mathbf{r}_i) &= \sum_{j=1}^M \left( p(\mathbf{r}_i, \theta_{j|i,k}) + n(\theta_{j|i,k}) \right) \cos(\theta_{j|i,k}) \approx \\
&\sum_{j=1}^M P_0(\mathbf{r}_i) \left[ \gamma_\kappa + \gamma_\rho \cos(\theta_{j|i,k}) \right] \cos(\theta_{j|i,k}) \\
&\quad + n(\theta_{j|i,k}) \cos(\theta_{j|i,k})
\end{aligned} \tag{6.8}$$

$$\begin{aligned}
I_{k,\rho}(\mathbf{r}_i) &= \int_{\theta=0}^{2\pi} \left( p(\mathbf{r}_i, \theta) + n(\theta) \right) \cos \theta d\theta \approx \\
&\int_{\theta=0}^{2\pi} P_0(\mathbf{r}_i) \gamma_\kappa \cos \theta d\theta + \int_{\theta=0}^{2\pi} P_0(\mathbf{r}_i) \gamma_\rho \cos^2(\theta) d\theta \\
&\quad + \int_{\theta=0}^{2\pi} n(\theta) \cos \theta d\theta \approx P_0(\mathbf{r}_i) \gamma_\rho \pi
\end{aligned} \tag{6.9}$$

Therefore, this method is able to produce values with respect to density differences of spherical scatterers with their surroundings for each transmit event  $k$ .

To create the final images, each subimage formed above must be coherently summed for all transmit events  $k$ :

$$\begin{aligned}
I_\kappa(\mathbf{r}_i) &= \sum_k I_{k,\kappa}(\mathbf{r}_i) \\
I_\rho(\mathbf{r}_i) &= \sum_k I_{k,\rho}(\mathbf{r}_i)
\end{aligned} \tag{6.10}$$

### 6.2.2 Numerical Integration

The method described above relies on the fact that delay-and-sum reconstruction techniques for circular arrays is practically quite similar to applying a Riemann used for calculating the integral of the scattered pressure with respect to scattering angle. Specifically, a left Riemann Sum for a function split into  $N$  subintervals can be described as:

$$\int_a^b f(x) \approx \Delta x \sum_{k=1}^M f(x_k) \quad (6.11)$$

where  $\Delta x = \frac{b-a}{N}$ . The difference between equations 6.6 and 6.11 lies with the multiplication of  $\Delta x$  (or  $\Delta\theta$  in this case). This multiplication, however, is not trivial, as for points not at the center of the transducer will have a nonuniform  $\Delta\theta$ , where  $\Delta\theta$  is the difference of scattering angles from neighboring receiving elements. In other words, the  $\Delta\theta$  for elements farther from the point will be smaller than  $\Delta\theta$  for elements closer to the point. Therefore, when converting delay-and-sum into a numerical integration form, it is important to include this nonuniformity. This can be performed by applying a trapezoidal rule with a nonuniform grid, which can be described as:

$$\int_{\theta=0}^{2\pi} p(\mathbf{r}_i, \theta) d\theta \approx \sum_{j=1}^M \frac{p(\mathbf{r}_i, \theta_{j+1}) + p(\mathbf{r}_i, \theta_j)}{2} (\theta_{j+1} - \theta_j) \quad (6.12)$$

for  $M+1$  elements on a  $360^\circ$  circular array transducer.

### 6.2.3 Limited-view Consideration

For ring array transducers that do not span the full  $360^\circ$ , the  $\cos(\theta)$  integrals described in equations 6.7 and 6.9 will not reduce to zero. For a transducer that has an angular span of  $[0, \theta_t]$ , we can rewrite equation 6.7 as follows (we will assume all noise integrations equal zero):

$$\begin{aligned} i_{k,\kappa}(\mathbf{r}_i) &= \int_{\theta=0}^{\theta_t} p(\mathbf{r}_i, \theta) d\theta \\ &\approx \int_{\theta=0}^{\theta_t} P_0(\mathbf{r}_i) \gamma_\kappa d\theta + \int_{\theta=0}^{\theta_t} P_0(\mathbf{r}_i) \gamma_\rho \cos(\theta) d\theta \\ &\approx P_0(\mathbf{r}_i) \gamma_\kappa \int_{\theta=0}^{\theta_t} d\theta + P_0(\mathbf{r}_i) \gamma_\rho \int_{\theta=0}^{\theta_t} \cos(\theta) d\theta \\ &\approx P_0(\mathbf{r}_i) \gamma_\kappa A + P_0(\mathbf{r}_i) \gamma_\rho B \end{aligned} \quad (6.13)$$

and similarly, equation 6.9 as:

$$\begin{aligned}
i_{k,\rho}(\mathbf{r}_i) &= \int_{\theta=0}^{\theta_t} p(\mathbf{r}_i, \theta) \cos(\theta) d\theta \\
&\approx \int_{\theta=0}^{\theta_t} P_0(\mathbf{r}_i) \gamma_\kappa \cos(\theta) d\theta + \int_{\theta=0}^{\theta_t} P_0(\mathbf{r}_i) \gamma_\rho \cos^2(\theta) d\theta \\
&\approx P_0(\mathbf{r}_i) \gamma_\kappa \int_{\theta=0}^{\theta_t} \cos(\theta) d\theta + P_0(\mathbf{r}_i) \gamma_\rho \int_{\theta=0}^{\theta_t} \cos^2(\theta) d\theta \\
&\approx P_0(\mathbf{r}_i) \gamma_\kappa B + P_0(\mathbf{r}_i) \gamma_\rho C
\end{aligned} \tag{6.14}$$

where  $i_{k,\kappa}(\mathbf{r}_i)$  and  $i_{k,\rho}(\mathbf{r}_i)$  are the limited-view delay-and-sum reconstruction value and the cosine-weighted delay-and-sum reconstruction value at point  $\mathbf{r}_i$  for transmit even  $k$ , respectively, and A, B, and C equal:

$$\begin{aligned}
A &= \int_{\theta=0}^{\theta_t} \theta d\theta \\
B &= \int_{\theta=0}^{\theta_t} \cos(\theta) d\theta \\
C &= \int_{\theta=0}^{\theta_t} \cos^2(\theta) d\theta
\end{aligned} \tag{6.15}$$

By solving equations 6.13 and 6.14 in terms of  $\gamma_\kappa$  and  $\gamma_\rho$ , we can recover compressibility- and density-decoupled images for point  $\mathbf{r}_i$  in image space, weighted by the limited-view integrals. These equations are as follows (for the case  $\pi < \theta_t < 2\pi$ ):

$$\hat{I}_{k,\kappa}(\mathbf{r}_i) = P_0(\mathbf{r}_i) \gamma_\kappa = \frac{BC}{AC - B^2} \left( \frac{i_{k,\kappa}(\mathbf{r}_i)}{B} - \frac{i_{k,\rho}(\mathbf{r}_i)}{C} \right) \tag{6.16}$$

$$\hat{I}_{k,\rho}(\mathbf{r}_i) = P_0(\mathbf{r}_i) \gamma_\rho = \frac{AB}{AC - B^2} \left( \frac{i_{k,\rho}(\mathbf{r}_i)}{B} - \frac{i_{k,\kappa}(\mathbf{r}_i)}{A} \right) \tag{6.17}$$

Equations 6.16 and 6.17 assume that  $|B| \neq 0$ . Due to the nonuniformity of  $\Delta\theta$ , this assumption may not always hold. For the case that  $|B| = 0$ , equations 6.16 and 6.17 can be reformulated as:

$$\hat{I}_{k,\kappa}(\mathbf{r}_i) = P_0(\mathbf{r}_i)\gamma_\kappa = \frac{i_{k,\kappa}(\mathbf{r}_i)}{A} \quad (6.18)$$

$$\hat{I}_{k,\rho}(\mathbf{r}_i) = P_0(\mathbf{r}_i)\gamma_\rho = \frac{i_{k,\rho}(\mathbf{r}_i)}{C} \quad (6.19)$$

It is clear that for a  $360^\circ$  transducer,  $A = 2\pi$  and  $C = \pi$ , reducing equations 6.18 and 6.19 to the solutions found in equations 6.7 and 6.9, respectively.

Finally, the final limited-view compressibility- and density-weighted images can be created by summing each of the above images for all transmit events  $k$ :

$$\hat{I}_\kappa(\mathbf{r}_i) = \sum_k \hat{I}_{k,\kappa}(\mathbf{r}_i) \quad (6.20)$$

$$\hat{I}_\rho(\mathbf{r}_i) = \sum_k \hat{I}_{k,\rho}(\mathbf{r}_i) \quad (6.21)$$

### 6.3 Methods and Materials

A 5 MHz, 256-element,  $256^\circ$  ring array was used for our experiments (Imasonic SAS, France). Each element had a pitch of  $0.7mm$ , an inter-element spacing of  $0.1mm$ , and toroidal elevation focusing has been applied. The elements themselves have been impedance matched to water. A Verasonics VDAS I ultrasound acquisition system (Verasonics Inc. Redmon, WA) was used in conjunction with this transducer. This system can transmit on 256 elements, and receive on 128. We used a sampling rate of 20 MHz. The raw data collected was post-processed using MATLAB (The MathWorks Inc., Natick, MA).

To reconstruct the compressibility-weighted ultrasound scattering tomography (UST) image ( $i_{k,\kappa}(\mathbf{r}_i)$ ), we implemented a delay-and-sum technique mentioned in the last section. The result is then corrected for losses due to attenuation. The resulting image from each receive element can then be summed using the nonuniform trapezoid rule described in equation 6.12.

Density-weighted images ( $i_{k,\rho}(\mathbf{r}_i)$ ) are reconstructed using a similar delay-and-sum technique as previously described, with one difference. As discussed in the Theory section, the cosine of the angle between the transmit and received angle for each pixel will be used as a weighting factor for each transmit-receive pair. This is applied to each image formed when back-propagating signals from one receive element with respect to one transmit element. Attenuation correction and nonuniform trapezoid rule summation are carried out as before.

Using equations 6.16, 6.17, 6.18, and 6.19, final  $\hat{I}_{k,\kappa}(\mathbf{r}_i)$  and  $\hat{I}_{k,\rho}(\mathbf{r}_i)$  maps can be created for each transmit event  $k$ . This method is then repeated for all transmit events, and the resulting images are coherently summed respectively to form a final compressibility and density image (see Eqn. 6.20 and 6.21). Finally, negative pixel values are truncated for image display. We will label final compressibility images ( $\hat{I}_{\kappa}(\mathbf{r}_i)$ ) as C-WI, and final density images ( $\hat{I}_{\rho}(\mathbf{r}_i)$ ) as D-WI. All images are displayed on a linear scale.

Decoupling compressibility and density relies on accurately measuring the signal intensity with respect to scattering angle. Therefore, phase aberrations can obfuscate this intensity change, worsening the decoupling ability of the method. Phase aberrations may be caused by speed-of-sound heterogeneities [105]. This can be accounted for by measuring speed-of-sound heterogeneities using transmission-based ultrasound tomography [105] or with other A-scan pre-processing techniques [106], however this is beyond the scope of the paper. Therefore, to mitigate these phase aberration errors, we chose to do one of two things to the A-scans of our receiving elements: to reconstruct the envelope of this signal, and to reconstruct the signal where the negative values of our A-scan have been truncated.

## 6.4 Results

### 6.4.1 Simulation

A simple forward model based on equation 6.1 was implemented in MATLAB. Delta pulses were used for transmission. Reconstruction algorithms

mentioned in the previous section were implemented in MATLAB. Due to the use of delta pulses, no A-scan preprocessing was necessary.

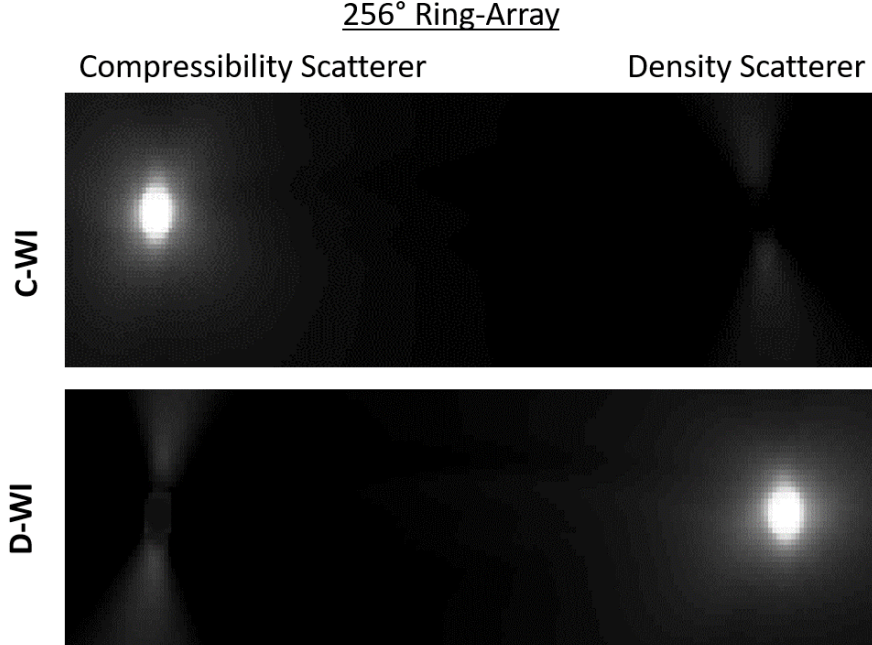


Figure 6.2: Simulation of large compressibility (left) and density scatterer (right) using a limited 256° transducer. Compressibility-weighted image is found on top, and density-weighted image is found on the bottom.

Two simulations were executed, all with a background value of  $\kappa_0 = 1$  and  $\rho_0 = 1$ . Two types of scatterers were simulated: compressibility scatterers and density scatterers. For the compressibility scatterers, we used a value of  $\kappa_v = 1.375$  and  $\rho_v = 1$ . For density scatterers we used values of  $\kappa_v = 1$  and  $\rho_v = 1.5$ . This guarantees that our  $\gamma_\kappa$  for our compressibility scatterers equals the  $\gamma_\rho$  for our density scatterers (specifically:  $\gamma_\kappa = 0.375$ ,  $\gamma_\rho = 0$  for compressibility scatterers and  $\gamma_\kappa = 0$ ,  $\gamma_\rho = 0.375$  for density scatterers).

The first simulation consisted of two large compressibility and density scatterers both with radii of  $100\mu m$ . The compressibility scatterer was

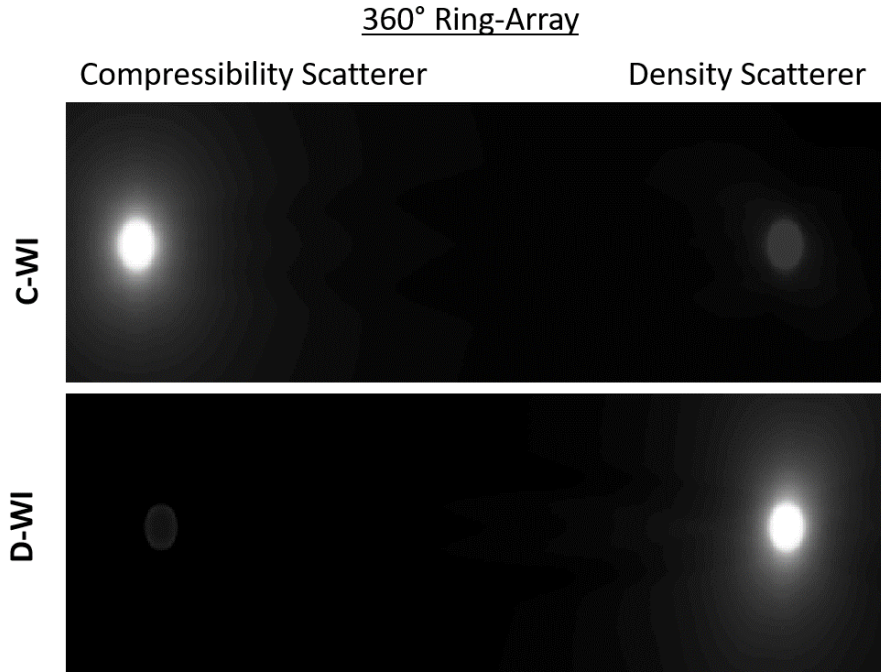


Figure 6.3: Simulation of large compressibility (left) and density scatterer (right) using a full 360° transducer. Compressibility-weighted image is found on top, and density-weighted image is found on the bottom.

placed on the left, and the density scatterer on the right. The result can be seen in Figure 6.2 using a simulated 256°, 256-element ring array transducer, similar to our experiments. This simulation was also done with a full 360°, 360-element ring array transducer in Figure 6.3. This was included to confirm that the bowtie-like artifacts in Figure 6.2 were caused by the limited angular span of our transducer and can be eliminated with full angular coverage.

Finally, the last simulation consisted of two inclusions with randomly placed scatterers within them. Compressibility scatterers were placed on the left inclusion, and density scatterers were placed on the right. This simulation was done using the 256°, 256-element ring trasducer The result can be seen in Figure 6.4.

### 256° Ring-Array

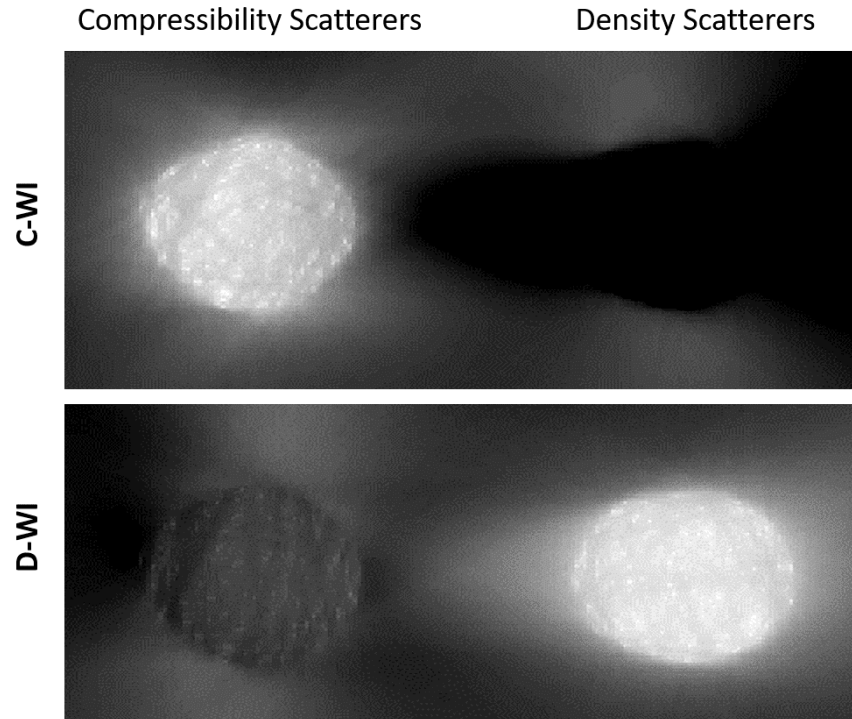


Figure 6.4: Simulation of two inclusions with randomly placed compressibility (left) and density (right) scatterers placed within each inclusion. Compressibility-weighted image is found on top, and density-weighted image is found on the bottom.

These simulations are highly idealized, however they help demonstrate the capability of these reconstruction techniques and the image artifacts systemic to the most basic tomographic reconstructions.

#### **6.4.2 Resolution**

An aluminum wire (diameter =  $12.5\mu\text{m}$ , Secon Metals) was suspended in water through the array transducer perpendicular to the imaging plane. Full-width half-maximums (FWHM) were calculated for both compressibility- and density-weighted images. This was done for both enveloped A-scans,

negative truncated A-scans, and unprocessed A-Scans (which will be referred to "full" A-scans), seen in Figure 6.5.

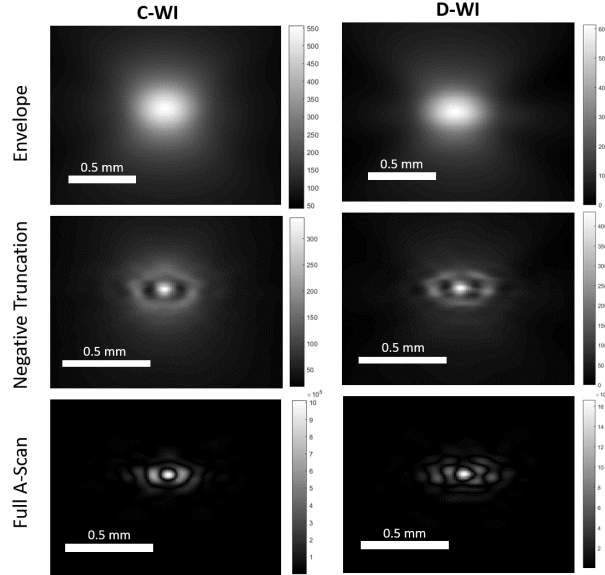


Figure 6.5: Aluminum wire imaged with compressibility-weighting (left) and density weighting (right). Scale bar is 0.5 mm

For enveloped A-scans, we were able to measure a resolution of  $437.5 \pm 15\mu m$  for C-WI and  $428.9 \pm 86\mu m$  for D-WI. Negative truncated A-scan resolutions were measured to be  $112.6 \pm 62.8\mu m$  for C-WI and  $109.5 \pm 52\mu m$  for D-WI. For full A-scan, we measured a FWHM of  $124 \pm 57\mu m$  for C-WI and  $110 \pm 50\mu m$  for D-Wi. The theoretical half-wavelength diffraction limited resolution of our system is  $\sim 150\mu m$ , which is achieved by both the negative truncated A-scan image and the full A-scans.

### 6.4.3 Wire Experiments

Three wires (steel, cotton, nylon) were suspended in a gelatin phantom (10%w/w gelatin/water) degassed for four hours. Water was used as an ultrasound medium between the phantom and the array transducer. The steel wire has an approximate density of about  $7.9 \text{ g/cm}^3$ . The cotton and

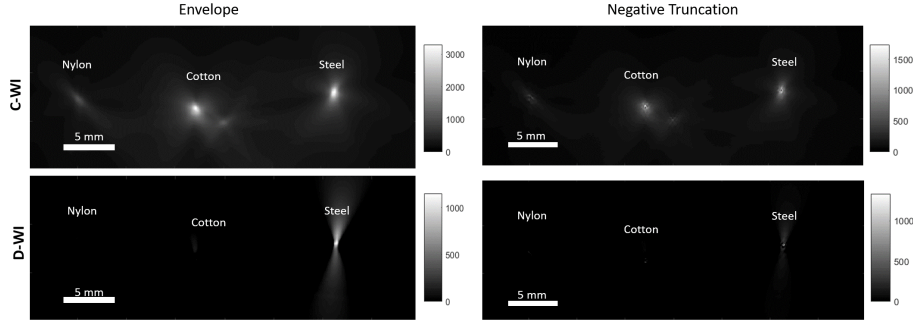


Figure 6.6: UST image of nylon (left), cotton (centre), and steel (right) wires using both compressibility weighting (top) and density weighting (bottom). Envelope-detection was implemented on A-scans. Scale bar equals 5 mm.

Table 6.1: Contrast values for Wire Experiments, see Equation 6.22

A-Scan Type	Material	C-WI	D-WI	Difference
Envelope	Steel vs Nylon	9.9 dB	35.3 dB	25.4 dB
	Steel vs Cotton	0.1 dB	22.9 dB	22.7 dB
Negative Truncation	Steel vs Nylon	9.6 dB	17.7 dB	8.1 dB
	Steel vs Cotton	-0.9 dB	9.2 dB	10.1 dB

nylon threads have an approximate density of  $1.5 \text{ g/cm}^3$  and  $1.1 \text{ g/cm}^3$  respectively [36]. All three wires have approximately the same diameter of  $100 \mu\text{m}$ . Gelatin-based phantoms have an approximate density of  $1.05 \text{ g/cm}^3$  [20]. Therefore, for our density-weighted images, we expect that the steel to be much larger than that of the cotton and nylon. The compressibility of steel is approximately two orders of magnitude lower than a gelatin phantom, and thus is expected to be seen in the compressibility-weighted images. The compressibility of cotton and nylon are difficult to measure accurately, so their visualization in the compressibility-weighted image is hard to predict.

Compressibility- and density-weighted images are shown in Figure 6.6 for enveloped A-scans and negative-truncated A-scans. It can be seen that, for our density-weighted image, the nylon wire has nearly disappeared for both images. To quantitatively assess the differentiation between the steel wire and the threads, we calculate a contrast value for C-WI, defined as:

$$C_{\kappa,s-n} = 20 \log_{10} \left( \frac{S_{\kappa,s}}{S_{\kappa,n}} \right) \quad (6.22)$$

where  $\kappa$  denotes C-WI,  $S_{\kappa,s}$  denotes the maximum signal of the steel wire for C-WI, and  $S_{\kappa,n}$  denotes the maximum signal of the nylon thread for C-WI.

It is clear that by removing phase entirely from our A-scans, decoupling between compressibility and density is improved compared to negative-truncated A-scans. This comes at a cost to resolution, as shown previously. Future work can be done to implement phase-aberration correction to our system. We believe that this implementation will remove the need to envelope or negatively-truncate our A-scans, providing strong decoupling at high resolutions.

#### 6.4.4 Phantom Experiments

The same steel and nylon wires from the previous experiment were suspended in a tissue-mimicking cornstarch/gelatin phantom (10%w/w cornstarch/water, 10%w/w gelatin/water). This phantom was placed within a water bath and imaged with the ring-array transducer described previously. The set-up can be seen in Figure 6.7.

Compressibility- and density-weighted images (C-WI and D-WI, respectively) were reconstructed using both enveloped A-Scans, negative truncated A-Scans, and unprocessed (or full) A-scans (seen in Figure 6.8). We also imaged this phantom with a 5 MHz, 128 element linear array (ATL L7-4, Broudsound Corporation) using a synthetic-aperture based beamforming technique (seen in Figure 6.8).

To quantify the differences between compressibility- and density-weighted images, we used a few different parameters. First, we use the same contrast equation from the previous section, namely equation 6.22. The results can be seen in Table 6.2 for both UST and linear-array images. We then defined a Contrast-to-Speckle Ratio (CSR) defined as follows (for a C-WI image):

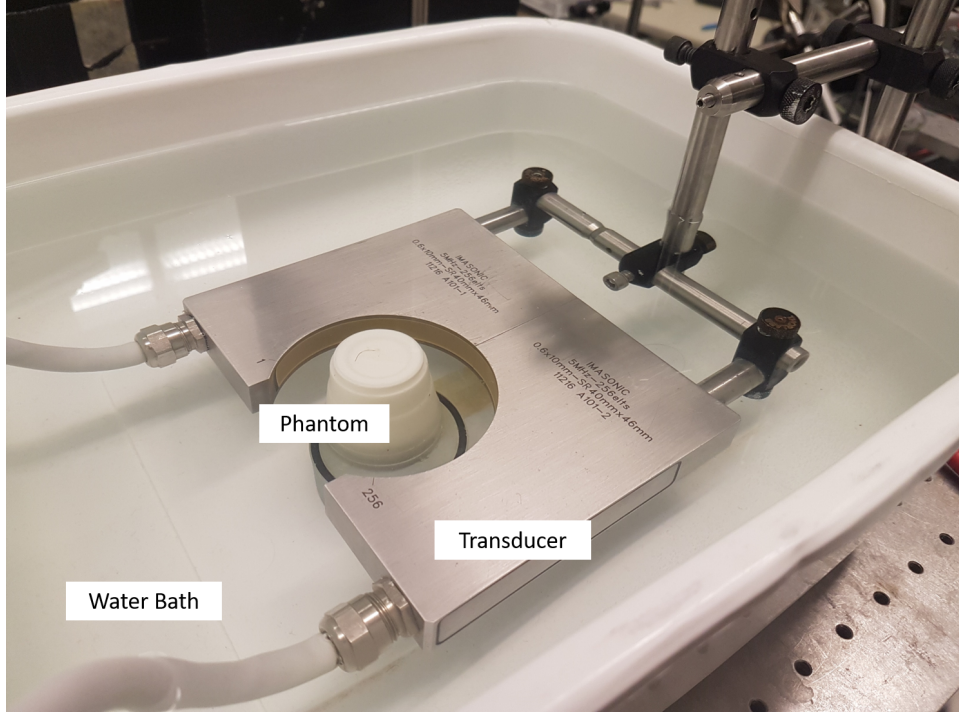


Figure 6.7: Experimental set-up with scattering phantom placed within a water bath.

$$CSR_{\kappa,s-n} = 20 \log_{10} \left( \frac{S_{\kappa,s} - S_{\kappa,n}}{\sigma_{\kappa,BG}} \right) \quad (6.23)$$

where  $\sigma_{\kappa,bg}$  is the variance of the background scattering medium (BG). These results can be seen in Table 6.3.

Another parameter we measured was a normalized contrast ratio (CN), defined as follows (for a C-WI image):

$$CN_{\kappa,s-n} = 20 \log_{10} \left( \frac{S_{\kappa,s} - S_{\kappa,n}}{\mu_{\kappa,BG}} \right) \quad (6.24)$$

where  $\mu_{\kappa,BG}$  is the mean of the background scattering medium for a large area of the phantom. These results can be seen in Table 6.4.

For all values, we calculated the difference (in dB) between those cal-

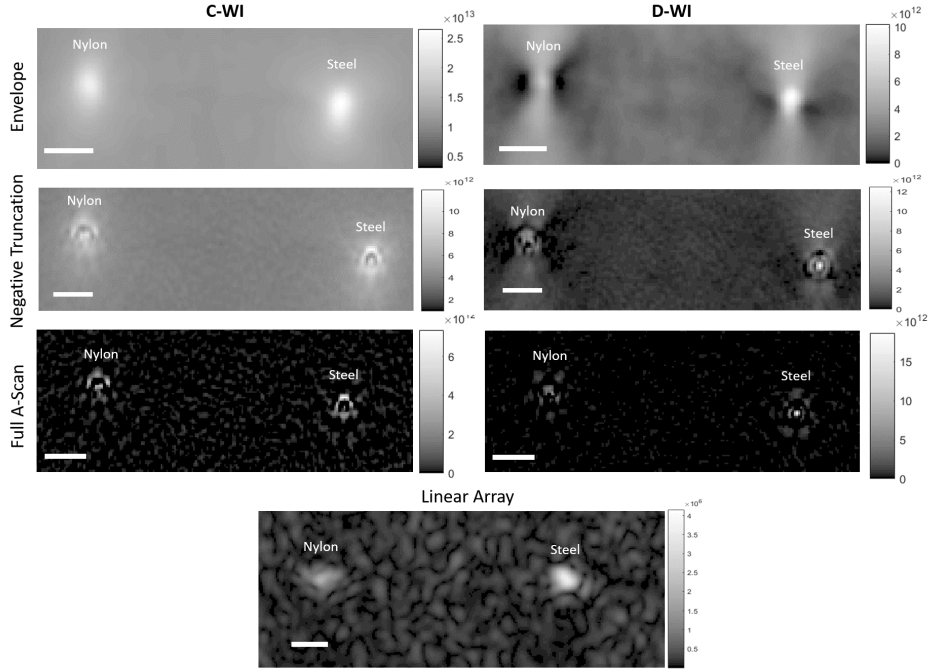


Figure 6.8: UST image of nylon (left) and steel (right) wires within a cornstarch scattering medium, with compressibility weighting (top) and density weighting (bottom) performed. Scale bar equals 1 mm.

culated for D-WI images and those calculated for C-WI images. Positive difference values denote an increase of signal between the steel wire and the nylon thread or the BG for the D-WI over the C-WI images. In other words, positive values indicate that the signal from the steel wire is easier to differentiate in the D-WI than in the C-WI with respect to both the nylon thread and the background cornstarch speckle. Moreover, we were able to measure high signal-to-noise ratio (SNR) for the wire and the thread for all images and A-scan preprocessing combinations, with values around  $100dB$  when calculating SNR for the wire (for example) as  $SNR_{\kappa,w} = \frac{S_{\kappa,w}}{\sigma_{\kappa,noise}}$  where  $\sigma_{\kappa,noise}$  is the standard deviation of the noise measured for the transducer in the water bath without any imaging target.

Table 6.2: Contrast values for scattering phantom, see Equation 6.22

Image Type	Material	C-WI	D-WI	Difference
UST: Envelope	Steel vs Nylon	0.9 dB	4.4 dB	3.5 dB
	Steel vs BG	9.9 dB	17.0 dB	7.0 dB
UST: Negative Truncation	Steel vs Nylon	2.0 dB	9.2 dB	7.2 dB
	Steel vs BG	13.0 dB	28.4 dB	15.4 dB
UST: Full A-Scan	Steel vs Nylon	4.2 dB	11.0 dB	6.8 dB
	Steel vs BG	41.8 dB	47.8 dB	5.9 dB
Linear Array	Steel vs Nylon	5.2 dB		
	Steel vs BG	26.6 dB		

Table 6.3: CSR values for scattering phantom, see Equation 6.23

A-Scan Type	Material	C-WI	D-WI	Difference
Envelope	Steel vs Nylon	8.4 dB	21.8 dB	13.4 dB
	Steel vs BG	25.2 dB	28.5 dB	3.2 dB
Negative Truncation	Steel vs Nylon	17.5 dB	35.0 dB	17.5 dB
	Steel vs BG	29.2 dB	38.4 dB	9.2 dB
Full A-Scan	Steel vs Nylon	29.7 dB	41.3 dB	11.6 dB
	Steel vs BG	38.0 dB	44.1 dB	6.1 dB
Linear Array	Steel vs Nylon	24.9 dB		
	Steel vs BG	31.5 dB		

Table 6.4: Normalized contrast values for scattering phantom, see Equation 6.24

A-Scan Type	Material	C-WI	D-WI	Difference
Envelope	Steel vs Nylon	-10.2 dB	9.0 dB	19.2 dB
	Steel vs BG	6.6 dB	15.7 dB	9.1 dB
Negative Truncation	Steel vs Nylon	-0.9 dB	24.7 dB	25.6 dB
	Steel vs BG	10.8 dB	28.1 dB	17.3 dB
Full A-Scan	Steel vs Nylon	33.5 dB	44.9 dB	11.4 dB
	Steel vs BG	41.8 dB	47.7 dB	5.9 dB
Linear Array	Steel vs Nylon	20.0 dB		
	Steel vs BG	26.5 dB		

## 6.5 Discussion

For all analysis values, seen in Tables 6.2, 6.3, and 6.4, we see large, positive differences between the wire and the thread. This difference can be seen in Figure 6.8, where the steel wire (right) is easier to differentiate from the nylon thread (left) in all three D-WI compared to the respective C-WI. For all the analysis values, the negatively truncated A-scan images outperformed the two other images. This is to be expected for the full A-scan due to the aforementioned phase aberration effects on final image quality. In addition, this observation highlights that, for enveloped scans, background speckle considerably degrades the decoupling efficacy. Regardless, the ability of the reconstruction algorithm to increase the contrast between the steel wire and nylon thread is apparent in all three images.

Another interesting effect of the D-WI images is the suppression of the background scatter compared to the C-WI images. For all methods, we saw large, positive differences between the wire and the background scatter. This effect can be qualitatively assessed in Figure 6.8, and may be useful for amplifying the signal from small, dense, specular objects suspended in soft tissue.

We also compared these values with those taken using a linear array with the same center frequency. Although they use different pre- and post-processing methods, a few interesting conclusions can be discussed. First,

the enveloped A-scan UST images were unable to match the linear array image. This is due to the fact that enveloping is done before backprojection for UST, and after beamforming for the linear array images. This preserved the constructive and destructive interference for the linear arrays, whereas these interferences is only constructive for enveloped UST. Second, we are able to see that both negative truncation and full a-scan UST outperforms the linear array image in suppression of the background signal. This may be due to two key reasons: first, the D-WI approach suppresses significant signals associated with compressibility microstructural variations, which is a major determinant of speckle in traditional B-scans; and second, our much larger angular coverage enables a high level of angular compounding which is known to reduce speckle variance.

These data show significant promise for imaging specular density targets, such as microcalcifications, with high CSR using the proposed density weighted ultrasound scattering tomography technique. Simulations indicate that the bowtie-like artifacts are attributed to the limited-view geometry of our ring array and could be mitigated with a full-view ring array.

## 6.6 Conclusion

In this paper, we develop new reconstruction techniques based off of conventional DAS algorithms to differentiate between compressibility and density for radially-symmetric scatterers. These new reconstruction techniques were tested with phantom experiments, both in clear and scattering phantom backgrounds. We were able to show that these novel reconstruction techniques allows for better differentiation between dense and compressible objects. Furthermore, we observed a decreased in background ultrasound speckle with respect to the dense object for our density-weighted images. This may provide useful for differentiating microcalcifications (dense calcium deposits) within breast tissue. Microcalcification size, shape, and pattern within the breast can be a used to diagnose early breast cancer [81], however for conventional ultrasound imaging, microcalcifications are difficult to discern from the background echo [83]. These novel reconstruction techniques

may allow ultrasound tomography to be an alternative modality to assess these microcalcifications, however future work must be done to demonstrate this.

For all reflection-based UST systems, a DAS-type algorithm is used for reconstructing morphological ultrasound images. Therefore, these systems are all capable of applying these novel reconstruction techniques. This is especially true for UST systems that have implemented phase-aberration correction [105,106]. Future work will be to include phase-aberration correction to our system. Moreover, it was shown that the limited-view ring array suffered from bowtie-like artifacts both in simulation and in the phantom experiment. Therefore, other future work will include the application of these reconstruction technique for full-view ring-array transducer. Finally, the reconstruction technique was developed for 2D UST images, however they could be extended to 3D UST systems using cylindrical or bowl-shaped transducer geometries. We hope that the inclusion of our reconstruction technique strengthens the scope of ultrasound tomography systems, adding a novel adjunct modality to this new imaging field.

## Chapter 7

# Conclusion

The main goal of this thesis was to develop a dual-modality photoacoustic-ultrasound tomography system capable of producing composite photoacoustic-ultrasound tomographic images. With this system, we were able to improve the scalability and SNR of both modalities without sacrificing imaging speed or resolution. Furthermore, novel reconstruction techniques were developed to exploit the full-view nature of ultrasound tomography with respect to anisotropic scattering. The two techniques focused on two different types of anisotropic ultrasound scattering: one focused on geometry (to image principal scattering angle), and one focused on material composition (to image differences in compressibility and density).

For photoacoustic tomography, we improved its scalability by implementing a scanned-mosaic illumination approach. This approach improved the SNR of photoacoustic images compared to a diffused (or blanket) illumination approach generally used for this type of imaging for the same imaging speed. This approach also allows the application ANSI-limited fluence over a large area regardless of the method used to produce the illumination. Therefore, any photoacoustic tomography imaging set-up could reach the laser power limits delimitated by ANSI, and thus producing images with as high an SNR available within these limits. This method also is faster than conventional averaging techniques to boost SNR, allowing faster photoacoustic imaging times for large-area targets. These SNR advantages diminished

with respect to image target depth.

For ultrasound tomography, we increased the SNR of our system by implementing an S-Sequence-based spatial encoding technique. To our knowledge, this is the first application of spatial encoding for ultrasound scattering tomography. This allowed for an increase of SNR without reducing the resolution of our system, allowing for high-SNR ultrasound tomography images that contain half-wavelength diffraction-limited resolution.

With this system, two methods of ultrasound scatter anisotropy visualization were implemented. Ultrasound tomography has a unique ability to measure ultrasound scattering for a large angular span around the target. This scattering may be anisotropic, or dependent on the angle it makes between the transmitted wave direction and the scattered wave direction. This can be caused by a number of things, such as geometric anisotropy, as you would see in long fibres, or material properties, such as compressibility and density. In this thesis, we develop novel reconstruction techniques to visualize these two different kinds of ultrasound scattering anisotropy.

The first method was able to visualize principal scattering directions of scatterers with an elongated, fibre-like shape. This shape will cause scattering to be high for transmitted wave directions orthogonal to the scatterer's geometry, and low for transmitted wave directions parallel to the scatterer's geometry. By measuring the signal change between different transmit-receive angles, we were able to visualize this difference, thus visualizing the direction of our geometrically anisotropic scatterers. We hope this new method can be applied to fibre-orientation visualization, similar to tractographic imaging of MRI. Similar principal-angle-based anisotropic ultrasound images have been previously developed in hopes to produce tissue differentiation. However, these previous approaches did not enable imaging of geometric scattering anisotropy for small scatterers, nor did they provide diffraction-limited resolution. These capabilities are demonstrated in our work for the first time. With this in mind, we hope that our novel reconstruction techniques will allow visualization of changing extracellular tissue matrices that, in theory, may change the principal scattering angles of the tissue. Extracellular tissue reorganization is caused by aggressive tumours,

and thus this technique may be impactful for measuring this effect.

The second method focused on measuring the anisotropy caused by compressibility and density contrast between spherically-symmetric scatterers and the media in which they were suspended. Compressibility contrast will produce isotropic, monopole scattering, whereas density contrast will produce anisotropic, dipole scattering. During delay-and-sum (DAS) ultrasound tomography reconstruction, scattering intensities are summed for large angle spans around the scatterer. This will cause the compressibility signal to increase, but the density signal to decrease, due to its cosine nature. By applying specific cosine weighting to each sum, the cosine weighting will substantially mitigate the contribution of the compressibility signal, whereas the density signal will be retained. Therefore, our novel reconstruction methods will be able to produce two images: a compressibility-weighted image and a density-weighted image. This was verified with simulations and phantom experiments. This novel reconstruction technique may provide better ultrasound images of microcalcifications - calcium deposits that are much denser than the surrounding tissue. Ultrasound images of breast tissue have a difficult time separating microcalcifications from the surrounding background speckle. We were able to show that density-weighted images help suppress this speckle while maintaining the signal of the high density target. Thus, we hope this reconstruction technique can provide clearer delineation of microcalcifications for ultrasound imaging of the breast. Our approach offers improved capabilities over previous attempts to decouple compressibility and density with linear array transducers, including near-diffraction-limited resolution, improved signal decoupling, and novel speckle reduction capabilities.

Future work with this system should include imaging small animal targets *in vivo*. This application will allow photoacoustic imaging of genetically encoded reporter proteins, such as photo-switchable proteins; research that is currently being done in the Zemp Lab. Another direction for future work should include the implementation of transmission-based ultrasound tomography, allowing the procurement of quantitative information such as speed-of-sound and attenuation. Not only will this provide useful,

quantitative information, it can also be used to improve the reflection-mode images. Specifically, speed-of-sound and attenuation maps can be used to avoid homogeneous tissue assumptions, and to allow for phase-aberration correction. Finally, application of our compressibility- and density-weighted imaging technique should be applied to clinical microcalcification imaging breast cancer experiments.

# Bibliography

- [1] Mx transducers. <http://www.visualsonics.com/products/vevo-3100/mx-transducers>. Accessed: 2016-11-07.
- [2] Michael P André, Helmar S Janée, Peter J Martin, Gregory P Otto, Brett A Spivey, and Douglas A Palmer. High-speed data acquisition in a diffraction tomography system employing large-scale toroidal arrays. *International Journal of Imaging Systems and Technology*, 8(1):137–147, 1997.
- [3] Sara Bahramian and Michael F Insana. Improved microcalcification detection in breast ultrasound: Phantom studies. In *Ultrasonics Symposium (IUS), 2014 IEEE International*, pages 2359–2362. IEEE, 2014.
- [4] Quinn Barber, Tyler Harrison, and Roger J Zemp. Blanket illumination vs scanned-mosaicking imaging schemes for wide-area photoacoustic tomography. In *SPIE BiOS*, pages 93232V–93232V. International Society for Optics and Photonics, 2015.
- [5] Quinn Barber and Roger J Zemp. Ultrasound scattering anisotropy visualization with ultrasound tomography. *IEEE Transactions on Ultrasonics, Ferroelectrics, and Frequency Control*, 2016.
- [6] Quinn Barber and Roger J Zemp. Photoacoustic-ultrasound tomography with s-sequence aperture encoding. *IEEE Transactions on Ultrasonics, Ferroelectrics, and Frequency Control*, 2017.

- [7] Paul Beard. Biomedical photoacoustic imaging. *Interface focus*, page rsfs20110028, 2011.
- [8] Alexander Graham Bell. On the production and reproduction of sound by light. *American Journal of Science*, (118):305–324, 1880.
- [9] Wendie A Berg, Jeffrey D Blume, Jean B Cormack, Ellen B Mendelson, Daniel Lehrer, Marcela Böhm-Vélez, Etta D Pisano, Roberta A Jong, W Phil Evans, Marilyn J Morton, et al. Combined screening with ultrasound and mammography vs mammography alone in women at elevated risk of breast cancer. *Jama*, 299(18):2151–2163, 2008.
- [10] Nykolai Bilaniuk and George SK Wong. Speed of sound in pure water as a function of temperature. *The Journal of the Acoustical Society of America*, 93(3):1609–1612, 1993.
- [11] Matthias Birk, Robin Dapp, Nicole V Ruiter, and Jürgen Becker. Gpu-based iterative transmission reconstruction in 3d ultrasound computer tomography. *Journal of Parallel and Distributed Computing*, 74(1):1730–1743, 2014.
- [12] Matthias Birk, Michael Zapf, Matthias Balzer, Nicole Ruiter, and Jürgen Becker. A comprehensive comparison of gpu-and fpga-based acceleration of reflection image reconstruction for 3d ultrasound computer tomography. *Journal of real-time image processing*, 9(1):159–170, 2014.
- [13] Jerome MG Borsboom, Chien Ting Chin, Ayache Bouakaz, Michel Versluis, and Nico de Jong. Harmonic chirp imaging method for ultrasound contrast agent. *ieee transactions on ultrasonics, ferroelectrics, and frequency control*, 52(2):241–249, 2005.
- [14] Andreas Buehler, Eva Herzog, Daniel Razansky, and Vasilis Ntzichristos. Video rate optoacoustic tomography of mouse kidney perfusion. *Optics letters*, 35(14):2475–2477, 2010.

- [15] Andreas Buehler, Amir Rosenthal, Thomas Jetzfellner, Alexander Dima, Daniel Razansky, and Vasilis Ntziachristos. Model-based optoacoustic inversions with incomplete projection data. *Medical Physics*, 38(3), 2011.
- [16] Paul L Carson, Charles R Meyer, Ann L Scherzinger, and Thomas V Oughton. Breast imaging in coronal planes with simultaneous pulse echo and transmission ultrasound. *Science*, 214(4525):1141–1143, 1981.
- [17] Amy V Chudgar and David A Mankoff. Molecular imaging and precision medicine in breast cancer. *PET clinics*, 12(1):39–51, 2017.
- [18] Richard SC Cobbold. *Foundations of biomedical ultrasound*. Oxford University Press, 2006.
- [19] James RW Conway, Neil O Carragher, and Paul Timpson. Developments in preclinical cancer imaging: innovating the discovery of therapeutics. *Nature Reviews Cancer*, 14(5):314–328, 2014.
- [20] Martin O Culjat, David Goldenberg, Priyamvada Tewari, and Rahul S Singh. A review of tissue substitutes for ultrasound imaging. *Ultrasound in medicine & biology*, 36(6):861–873, 2010.
- [21] Amy Berrington de Gonzalez and Sarah Darby. Risk of cancer from diagnostic x-rays: estimates for the uk and 14 other countries. *The lancet*, 363(9406):345–351, 2004.
- [22] Neb Duric, Peter Littrup, Cuiping Li, Olivier Roy, Steven Schmidt, Roman Janer, Xiaoyang Cheng, Jeffrey Goll, Olsi Rama, Lisa Bey-Knight, et al. Breast ultrasound tomography: bridging the gap to clinical practice. In *SPIE Medical Imaging*, pages 83200O–83200O. International Society for Optics and Photonics, 2012.
- [23] Nebojsa Duric, Peter Littrup, Lou Poulo, Alex Babkin, Roman Pevzner, Earle Holsapple, Olsi Rama, and Carri Glide. Detection of

- breast cancer with ultrasound tomography: First results with the computed ultrasound risk evaluation (cure) prototype. *Medical physics*, 34(2):773–785, 2007.
- [24] Nebojsa Duric, Peter Littrup, Erik West, Bryan Ranger, Cuiping Li, and Steven Schmidt. In-vivo imaging of breast cancer with ultrasound tomography: probing the tumor environment. In *SPIE Medical Imaging*, pages 796812–796812. International Society for Optics and Photonics, 2011.
- [25] Sergey A Ermilov, Tuenchit Khamapirad, Andre Conjusteau, Morton H Leonard, Ron Lacewell, Ketan Mehta, Tom Miller, and Alexander A Oraevsky. Laser optoacoustic imaging system for detection of breast cancer. *Journal of biomedical optics*, 14(2):024007–024007, 2009.
- [26] Kevin D Evans, Brandon Weiss, and Michael Knopp. High-intensity focused ultrasound (hifu) for specific therapeutic treatments: a literature review. *Journal of Diagnostic Medical Sonography*, 23(6):319–327, 2007.
- [27] Christopher P Favazza, Omar Jassim, Lynn A Cornelius, and Lihong V Wang. In vivo photoacoustic microscopy of human cutaneous microvasculature and a nevus. *Journal of biomedical optics*, 16(1):016015–016015, 2011.
- [28] Jacques Ferlay, Clarisse Héry, Philippe Autier, and Rengaswamy Sankaranarayanan. Global burden of breast cancer. In *Breast cancer epidemiology*, pages 1–19. Springer, 2010.
- [29] Grigory S Filonov, Arie Krumholz, Jun Xia, Junjie Yao, Lihong V Wang, and Vladislav V Verkhusha. Deep-tissue photoacoustic tomography of a genetically encoded near-infrared fluorescent probe. *Angewandte Chemie International Edition*, 51(6):1448–1451, 2012.
- [30] John Gamelin, Anastasios Maurudis, Andres Aguirre, Fei Huang, Puyun Guo, Lihong V Wang, and Quing Zhu. A real-time pho-

- toacoustic tomography system for small animals. *Optics express*, 17(13):10489–10498, 2009.
- [31] Jérôme Gateau, Miguel Ángel Araque Caballero, Alexander Dima, and Vasilis Ntziachristos. Three-dimensional optoacoustic tomography using a conventional ultrasound linear detector array: Whole-body tomographic system for small animals. *Medical physics*, 40(1), 2013.
- [32] H Gemmeke and NV Ruiter. 3d ultrasound computer tomography for medical imaging. *Nuclear Instruments and Methods in Physics Research Section A: Accelerators, Spectrometers, Detectors and Associated Equipment*, 580(2):1057–1065, 2007.
- [33] James F Greenleaf. Computerized tomography with ultrasound. *Proceedings of the IEEE*, 71(3):330–337, 1983.
- [34] James F Greenleaf, SA Johnson, and Robert C Bahn. Quantitative cross-sectional imaging of ultrasound parameters. In *Ultrasonics Symposium, 1977*, pages 989–995. IEEE, 1977.
- [35] Adriana Gregory, Mahdi Bayat, Max Denis, Mohammad Mehrmohammadi, Mostafa Fatemi, and Azra Alizad. An experimental phantom study on the effect of calcifications on ultrasound shear wave elastography. In *Engineering in Medicine and Biology Society (EMBC), 2015 37th Annual International Conference of the IEEE*, pages 3843–3846. IEEE, 2015.
- [36] DA Guenther, K Ranganathan, MJ McAllister, WF Walker, and KW Rigby. Ultrasonic synthetic aperture angular scatter imaging. In *Signals, Systems and Computers, 2004. Conference Record of the Thirty-Eighth Asilomar Conference on*, volume 1, pages 163–167. IEEE, 2004.
- [37] Drake A Guenther, Karthik Ranganathan, Michael J McAllister, KW Rigby, and William F Walker. Synthetic aperture methods for angular scatter imaging. In *Medical Imaging 2004*, pages 52–60. International Society for Optics and Photonics, 2004.

- [38] Christoph Haisch. Quantitative analysis in medicine using photoacoustic tomography. *Analytical and bioanalytical chemistry*, 393(2):473–479, 2009.
- [39] Tyler Harrison, Alexander Sampaleanu, and Roger J Zemp. S-sequence spatially-encoded synthetic aperture ultrasound imaging [correspondence]. *IEEE transactions on ultrasonics, ferroelectrics, and frequency control*, 61(5):886–890, 2014.
- [40] QiuHong He, Ray Z Xu, Pavel Shkarin, Giuseppe Pizzorno, Carol H Lee-French, Douglas L Rothman, Dikoma C Shungu, and Hyunsuk Shim. Magnetic resonance spectroscopic imaging of tumor metabolic markers for cancer diagnosis, metabolic phenotyping, and characterization of tumor microenvironment. *Disease markers*, 19(2, 3):69–94, 2004.
- [41] N Lynn Henry and Daniel F Hayes. Cancer biomarkers. *Molecular oncology*, 6(2):140–146, 2012.
- [42] Lianjie Huang, Yassin Labyed, Kenneth Hanson, Daniel Sandoval, Jennifer Pohl, and Michael Williamson. Detecting breast microcalcifications using super-resolution ultrasound imaging: A clinical study. In *SPIE Medical Imaging*, pages 86751O–86751O. International Society for Optics and Photonics, 2013.
- [43] Lianjie Huang, Yassin Labyed, Youzuo Lin, Zhigang Zhang, Jennifer Pohl, Daniel Sandoval, and Michael Williamson. Detection of breast microcalcifications using synthetic-aperture ultrasound. In *SPIE Medical Imaging*, pages 83200H–83200H. International Society for Optics and Photonics, 2012.
- [44] Kullervo Hynynen, Nathan McDannold, Nickolai A Sheikov, Ferenc A Jolesz, and Natalia Vykhodtseva. Local and reversible blood–brain barrier disruption by noninvasive focused ultrasound at frequencies suitable for trans-skull sonications. *Neuroimage*, 24(1):12–20, 2005.

- [45] Umer Zeeshan Ijaz, R James Housden, Graham M Treece, Richard W Prager, and Andrew H Gee. Multidirectional scattering models for 3-dimensional ultrasound imaging. *Journal of Ultrasound in Medicine*, 32(4):699–714, 2013.
- [46] American National Standards Institute. *American National Standard for Safe Use of Lasers*. Laser Institute of America, 2007.
- [47] Amit P Jathoul, Jan Laufer, Olumide Ogunlade, Bradley Treeby, Ben Cox, Edward Zhang, Peter Johnson, Arnold R Pizzey, Brian Philip, Teresa Marafioti, et al. Deep in vivo photoacoustic imaging of mammalian tissues using a tyrosinase-based genetic reporter. *Nature Photonics*, 2015.
- [48] Jeong-Won Jeong, Tae-Seong Kim, Dae C Shin, Synho Do, Manbir Singh, and Vasilis Z Marmarelis. Soft tissue differentiation using multi-band signatures of high resolution ultrasonic transmission tomography. *IEEE transactions on medical imaging*, 24(3):399–408, 2005.
- [49] Andrei B Karpiouk, Salavat R Aglyamov, Srivalleesha Mallidi, Jignesh Shah, W Guy Scott, Jonathan M Rubin, and Stanislav Y Emelianov. Combined ultrasound and photoacoustic imaging to detect and stage deep vein thrombosis: phantom and ex vivo studies. *Journal of biomedical optics*, 13(5):054061–054061, 2008.
- [50] Chulhong Kim, Alejandro Garcia-Urbe, Sri-Rajasekhar Kothapalli, and Lihong V Wang. Optical phantoms for ultrasound-modulated optical tomography. In *Biomedical Optics (BiOS) 2008*, pages 68700M–68700M. International Society for Optics and Photonics, 2008.
- [51] Tae-Seong Kim, Syn-Ho Do, and Vasilis Z Marmarelis. Multiband tissue differentiation in ultrasonic transmission tomography. In *Proceedings of SPIE*, volume 5035, pages 41–48, 2003.
- [52] SJ Kleis and LA Sanchez. Dependence of sound velocity on salinity and temperature in saline solutions. *Solar Energy*, 46(6):371–375, 1991.

- [53] Luděk Klimeš. Grid travel-time tracing: Second-order method for the first arrivals in smooth media. In *Seismic Waves in Laterally Inhomogeneous Media Part II*, pages 539–563. Springer, 1996.
- [54] Roy GM Kolkman, Peter J Brands, Wiendelt Steenbergen, and Ton G van Leeuwen. Real-time in vivo photoacoustic and ultrasound imaging. *Journal of biomedical optics*, 13(5):050510–050510, 2008.
- [55] Ernst Kretzek, Patrick Hucker, Michael Zapf, and Nicole V Ruiter. Evaluation of directional reflectivity characteristics as new modality for 3d ultrasound computer tomography. In *Ultrasonics Symposium (IUS), 2015 IEEE International*, pages 1–4. IEEE, 2015.
- [56] Ernst Kretzek, Michael Zapf, Matthias Birk, Hartmut Gemmeke, and Nicole V. Ruiter. Gpu based acceleration of 3d usct image reconstruction with efficient integration into matlab. volume 8675, pages 86750O–86750O–10, 2013.
- [57] Robert Kruger, Daniel Reinecke, Gabe Kruger, Michael Thornton, Paul Picot, Timothy Morgan, Keith Stantz, and Charles Mistretta. Hypr-spectral photoacoustic ct for preclinical imaging. In *Proc. SPIE*, volume 7177, page 71770F, 2009.
- [58] Robert A Kruger, Cherie M Kuzmiak, Richard B Lam, Daniel R Reinecke, Stephen P Del Rio, and Doreen Steed. Dedicated 3d photoacoustic breast imaging. *Medical physics*, 40(11), 2013.
- [59] Robert A Kruger, Richard B Lam, Daniel R Reinecke, Stephen P Del Rio, and Ryan P Doyle. Photoacoustic angiography of the breast. *Medical physics*, 37(11):6096–6100, 2010.
- [60] Geng Ku, Xueding Wang, George Stoica, and Lihong V Wang. Multiple-bandwidth photoacoustic tomography. *Physics in medicine and biology*, 49(7):1329, 2004.

- [61] Geng Ku, Xueding Wang, Xueyi Xie, George Stoica, and Lihong V Wang. Imaging of tumor angiogenesis in rat brains in vivo by photoacoustic tomography. *Applied optics*, 44(5):770–775, 2005.
- [62] Peter Kuchment and Leonid Kunyansky. Mathematics of thermoacoustic tomography. *European Journal of Applied Mathematics*, 19(02):191–224, 2008.
- [63] Christiane K Kuhl, Simone Schradang, Claudia C Leutner, Nuschin Morakkabati-Spitz, Eva Wardelmann, Rolf Fimmers, Walther Kuhn, and Hans H Schild. Mammography, breast ultrasound, and magnetic resonance imaging for surveillance of women at high familial risk for breast cancer. *Journal of clinical oncology*, 23(33):8469–8476, 2005.
- [64] Minalini Lakshman and Andrew Needles. Screening and quantification of the tumor microenvironment with micro-ultrasound and photoacoustic imaging. *Nature Methods*, 12(4), 2015.
- [65] Richard B Lam, Robert A Kruger, Daniel R Reinecke, Stephen P DelRio, Michael M Thornton, Paul A Picot, and Timothy G Morgan. Dynamic optical angiography of mouse anatomy using radial projections. In *BiOS*, pages 756405–756405. International Society for Optics and Photonics, 2010.
- [66] Jan Laufer, Peter Johnson, Edward Zhang, Bradley Treeby, Ben Cox, Barbara Pedley, and Paul Beard. In vivo preclinical photoacoustic imaging of tumor vasculature development and therapy. *Journal of biomedical optics*, 17(5):0560161–0560168, 2012.
- [67] Claude C Leroy, Stephen P Robinson, and Mike J Goldsmith. A new equation for the accurate calculation of sound speed in all oceans. *The Journal of the Acoustical Society of America*, 124(5):2774–2782, 2008.
- [68] Changhui Li and Lihong V Wang. Photoacoustic tomography and sensing in biomedicine. *Physics in medicine and biology*, 54(19):R59, 2009.

- [69] Cuiping Li, Neb Duric, and Lianjie Huang. Clinical breast imaging using sound-speed reconstructions of ultrasound tomography data. In *Medical Imaging*, pages 692009–692009. International Society for Optics and Photonics, 2008.
- [70] Cuiping Li, Gursharan S Sandhu, Olivier Roy, Neb Duric, Veerendra Allada, and Steven Schmidt. Toward a practical ultrasound waveform tomography algorithm for improving breast imaging. In *SPIE Medical Imaging*, pages 90401P–90401P. International Society for Optics and Photonics, 2014.
- [71] Meng-Lin Li, Yi-Chieh Tseng, and Chung-Chih Cheng. Model-based correction of finite aperture effect in photoacoustic tomography. *Opt. Express*, 18(25):26285–26292, Dec 2010.
- [72] Fredrik Lingvall. *Time-domain Reconstruction Methods for Ultrasonic Array Imaging*. PhD thesis.
- [73] Dong-Lai Liu and Robert C Waag. Propagation and backpropagation for ultrasonic wavefront design. *IEEE transactions on ultrasonics, ferroelectrics, and frequency control*, 44(1):1–13, 1997.
- [74] R Liu, NV Ruiter, GF Schwarzenberg, M Zapf, R Stotzka, and H Gemmeke. 2j-2 3d ultrasound computer tomography: Results with a clinical breast phantom. In *Ultrasonics Symposium, 2006. IEEE*, pages 989–992. IEEE, 2006.
- [75] Pengfei Lu, Valerie M Weaver, and Zena Werb. The extracellular matrix: a dynamic niche in cancer progression. *J Cell Biol*, 196(4):395–406, 2012.
- [76] VZ Marmarelis, J Jeong, DC Shin, and S Do. High-resolution 3-d imaging and tissue differentiation with transmission tomography. In *Acoustical imaging*, pages 195–206. Springer, 2007.

- [77] Konstantin Maslov, Gheorghe Stoica, and Lihong V Wang. In vivo dark-field reflection-mode photoacoustic microscopy. *Optics letters*, 30(6):625–627, 2005.
- [78] Konstantin Maslov, Hao F Zhang, Song Hu, and Lihong V Wang. Optical-resolution photoacoustic microscopy for in vivo imaging of single capillaries. *Optics letters*, 33(9):929–931, 2008.
- [79] Elena Merčep, Neal C Burton, Jing Claussen, and Daniel Razansky. Whole-body live mouse imaging by hybrid reflection-mode ultrasound and optoacoustic tomography. *Optics letters*, 40(20):4643–4646, 2015.
- [80] Elena Mercep, Gency Jeng, Stefan Morscher, Pai-Chi Li, and Daniel Razansky. Hybrid optoacoustic tomography and pulse-echo ultrasonography using concave arrays. *IEEE transactions on ultrasonics, ferroelectrics, and frequency control*, 62(9):1651–1661, 2015.
- [81] Barbara S Monsees. Evaluation of breast microcalcifications. *Radiologic Clinics of North America*, 33(6):1109–1121, 1995.
- [82] Leonardo G Montilla, Ragnar Olafsson, Daniel R Bauer, and Russell S Witte. Real-time photoacoustic and ultrasound imaging: a simple solution for clinical ultrasound systems with linear arrays. *Physics in medicine and biology*, 58(1):N1, 2012.
- [83] Woo Kyung Moon, Jung-Gi Im, Young Hwan Koh, Dong-Young Noh, and In Ae Park. Us of mammographically detected clustered microcalcifications 1. *Radiology*, 217(3):849–854, 2000.
- [84] Yojana Nalawade. Evaluation of breast calcifications. *Indian Journal of radiology and imaging*, 19(4):282–282, 2009.
- [85] Andrew Needles, Andrew Heinmiller, John Sun, Catherine Theodoropoulos, David Bates, Desmond Hirson, Melissa Yin, and F Stuart Foster. Development and initial application of a fully integrated photoacoustic micro-ultrasound system. *IEEE transactions on ultrasonics, ferroelectrics, and frequency control*, 60(5):888–897, 2013.

- [86] Paolo A Netti, David A Berk, Melody A Swartz, Alan J Grodzinsky, and Rakesh K Jain. Role of extracellular matrix assembly in interstitial transport in solid tumors. *Cancer research*, 60(9):2497–2503, 2000.
- [87] Joël J Niederhauser, Michael Jaeger, Robert Lemor, Peter Weber, and Martin Frenz. Combined ultrasound and optoacoustic system for real-time high-contrast vascular imaging in vivo. *IEEE transactions on medical imaging*, 24(4):436–440, 2005.
- [88] Vasilis Ntziachristos and Daniel Razansky. Molecular imaging by means of multispectral optoacoustic tomography (msot). *Chemical reviews*, 110(5):2783–2794, 2010.
- [89] AC O’farrell, SD Shnyder, G Marston, PL Coletta, and JH Gill. Non-invasive molecular imaging for preclinical cancer therapeutic development. *British journal of pharmacology*, 169(4):719–735, 2013.
- [90] Elizabeth Am O’flynn, Jeremie Fromageau, Araminta E Ledger, Alessandro Messa, Ashley D’aquino, Minouk J Schoemaker, Maria Schmidt, Neb Duric, Anthony J Swerdlow, and Jeffrey C Bamber. Ultrasound tomography evaluation of breast density. *Investigative Radiology*, 2017.
- [91] Neslihan Ozmen, Robin Dapp, Michael Zapf, Hartmut Gemmeke, Nicole V Ruiter, and Koen WA van Dongen. Comparing different ultrasound imaging methods for breast cancer detection. *IEEE transactions on ultrasonics, ferroelectrics, and frequency control*, 62(4):637–646, 2015.
- [92] Clement Papadacci, Mickael Tanter, Mathieu Pernot, and Mathias Fink. Ultrasound backscatter tensor imaging (bti): analysis of the spatial coherence of ultrasonic speckle in anisotropic soft tissues. *IEEE transactions on ultrasonics, ferroelectrics, and frequency control*, 61(6):986–996, 2014.

- [93] Morten H Pedersen, Thanassis X Misaridis, and Jørgen A Jensen. Clinical evaluation of chirp-coded excitation in medical ultrasound. *Ultrasound in medicine & biology*, 29(6):895–905, 2003.
- [94] E Picano, L Landini, A Distanti, M Salvadori, F Lattanzi, M Masini, and A L’abbate. Angle dependence of ultrasonic backscatter in arterial tissues: a study in vitro. *Circulation*, 72(3):572–576, 1985.
- [95] Christian Plathow and Wolfgang A Weber. Tumor cell metabolism imaging. *Journal of Nuclear Medicine*, 49(Suppl 2):43S–63S, 2008.
- [96] R Gerhard Pratt, Lianjie Huang, Neb Duric, and Peter Littrup. Sound-speed and attenuation imaging of breast tissue using waveform tomography of transmission ultrasound data. In *Medical Imaging*, pages 65104S–65104S. International Society for Optics and Photonics, 2007.
- [97] Justin Rajesh Rajian, Gandikota Girish, and Xueding Wang. Photoacoustic tomography to identify inflammatory arthritis. *Journal of biomedical optics*, 17(9):0960131–0960136, 2012.
- [98] Bryan Ranger, Peter Littrup, Neb Duric, Cuiping Li, Steven Schmidt, Jessica Lupinacci, Lukasz Myc, Amy Szczepanski, Olsi Rama, and Lisa Bey-Knight. Breast imaging with ultrasound tomography: a comparative study with mri. In *Proceedings of SPIE*, volume 7629, pages 762906–1, 2010.
- [99] Bryan Ranger, Peter J Littrup, Nebojsa Duric, Priti Chandiwala-Mody, Cuiping Li, Steven Schmidt, and Jessica Lupinacci. Breast ultrasound tomography versus magnetic resonance imaging for clinical display of anatomy and tumor rendering: Preliminary results. *AJR. American journal of roentgenology*, 198(1):233, 2012.
- [100] Daniel Razansky, Andreas Buehler, and Vasilis Ntziachristos. Volumetric real-time multispectral optoacoustic tomography of biomarkers. *Nature protocols*, 6(8):1121–1129, 2011.

- [101] Daniel Razansky, Andreas Buehler, and Vasilis Ntziachristos. Volumetric real-time multispectral optoacoustic tomography of biomarkers. *Nature protocols*, 6(8):1121–1129, 2011.
- [102] Amir Rosenthal, Daniel Razansky, and Vasilis Ntziachristos. Fast semi-analytical model-based acoustic inversion for quantitative optoacoustic tomography. *IEEE transactions on medical imaging*, 29(6):1275–1285, 2010.
- [103] Nicole V Ruiter, Michael Zapf, Torsten Hopp, Robin Dapp, and Hartmut Gemmeke. Phantom image results of an optimized full 3d usct. In *SPIE Medical Imaging*, pages 832005–832005. International Society for Optics and Photonics, 2012.
- [104] Nicole V Ruiter, Michael Zapf, Torsten Hopp, Robin Dapp, Ernst Kretzek, Matthias Birk, Benedikt Kohout, and Hartmut Gemmeke. 3d ultrasound computer tomography of the breast: A new era? *European Journal of Radiology*, 81:S133–S134, 2012.
- [105] NV Ruiter, R Schnell, M Zapf, and H Gemmeke. P3d-2 phase aberration correction for 3d ultrasound computer tomography images. In *Ultrasonics Symposium, 2007. IEEE*, pages 1808–1811. IEEE, 2007.
- [106] NV Ruiter, GF Schwarzenberg, M Zapf, and H Gemmeke. Improvement of 3d ultrasound computer tomography images by signal pre-processing. In *Ultrasonics Symposium, 2008. IUS 2008. IEEE*, pages 852–855. IEEE, 2008.
- [107] NV Ruiter, GF Schwarzenberg, M Zapf, R Stotzka, and H Gemmeke. P3a-2 resolution assessment of a 3d ultrasound computer tomograph using ellipsoidal backprojection. In *Ultrasonics Symposium, 2006. IEEE*, pages 1979–1982. IEEE, 2006.
- [108] Jacob Staley, Patrick Grogan, Abbas K Samadi, Huizhong Cui, Mark S Cohen, and Xinmai Yang. Growth of melanoma brain tumors monitored by photoacoustic microscopy. *Journal of biomedical optics*, 15(4):040510–040510, 2010.

- [109] Rainer Stotzka, Nicole V Ruiter, Tim O Müller, Rong Liu, and Hartmut Gemmeke. High resolution image reconstruction in ultrasound computer tomography using deconvolution. In *Medical Imaging*, pages 315–325. International Society for Optics and Photonics, 2005.
- [110] Rainer Stotzka, Jan Wuerfel, Tim O Mueller, and Hartmut Gemmeke. Medical imaging by ultrasound computer tomography. In *Medical Imaging 2002*, pages 110–119. International Society for Optics and Photonics, 2002.
- [111] Mickael Tanter and Mathias Fink. Ultrafast imaging in biomedical ultrasound. *IEEE transactions on ultrasonics, ferroelectrics, and frequency control*, 61(1):102–119, 2014.
- [112] Chao Tao and Xiaojun Liu. Reconstruction of high quality photoacoustic tomography with a limited-view scanning. *Opt. Express*, 18(3):2760–2766, Feb 2010.
- [113] Torfinn Taxt. Separation of the diffuse, specular and quasiperiodic signal components in medical ultrasound images. In *Ultrasonics Symposium, 1994. Proceedings., 1994 IEEE*, volume 3, pages 1639–1644. IEEE, 1994.
- [114] Madeleine Tilanus-Linthorst, Leon Verhoog, Inge-Marie Obdeijn, Karina Bartels, Marian Menke-Pluymers, Alexander Eggermont, Jan Klijn, Hanne Meijers-Heijboer, Theo van der Kwast, and Cecile Brekelmans. A brca1/2 mutation, high breast density and prominent pushing margins of a tumor independently contribute to a frequent false-negative mammography. *International journal of cancer*, 102(1):91–95, 2002.
- [115] Michael Vogt, Jorn Opretzka, and Helmut Ermert. Parametric imaging of specular reflections and diffuse scattering of tissue from multi-directional ultrasound echo signal data. In *2008 IEEE Ultrasonics Symposium*, pages 1963–1966. IEEE, 2008.

- [116] WF Walker and MJ McAllister. Angular scatter imaging: Clinical results and novel processing. In *Ultrasonics Symposium, 2002. Proceedings. 2002 IEEE*, volume 2, pages 1565–1569. IEEE, 2002.
- [117] William F Walker. C-and d-weighted ultrasonic imaging using the translating apertures algorithm. *IEEE transactions on ultrasonics, ferroelectrics, and frequency control*, 48(2):452–461, 2001.
- [118] William F Walker and M Jason McAllister. C-and d-weighted imaging: theory and simulation. In *Ultrasonics Symposium, 1999. Proceedings. 1999 IEEE*, volume 2, pages 1557–1561. IEEE, 1999.
- [119] William F Walker and M Jason McAllister. Angular scatter imaging in medical ultrasound. In *Signals, Systems and Computers, 2002. Conference Record of the Thirty-Sixth Asilomar Conference on*, volume 1, pages 931–935. IEEE, 2002.
- [120] Kun Wang and Mark A Anastasio. A simple fourier transform-based reconstruction formula for photoacoustic computed tomography with a circular or spherical measurement geometry. *Physics in medicine and biology*, 57(23):N493, 2012.
- [121] Lihong Wang and Steven L Jacques. Monte carlo modeling of light transport in multi-layered tissues in standard c. *The University of Texas, MD Anderson Cancer Center, Houston*, pages 4–11, 1992.
- [122] Lihong V Wang. Prospects of photoacoustic tomography. *Medical physics*, 35(12):5758–5767, 2008.
- [123] Lihong V Wang. Tutorial on photoacoustic microscopy and computed tomography. *IEEE Journal of Selected Topics in Quantum Electronics*, 14(1):171–179, 2008.
- [124] Lihong V Wang and Song Hu. Photoacoustic tomography: in vivo imaging from organelles to organs. *Science*, 335(6075):1458–1462, 2012.

- [125] Lihong V Wang and Hsin-i Wu. *Biomedical optics: principles and imaging*. John Wiley & Sons, 2012.
- [126] E Warner, DB Plewes, RS Shumak, GC Catzavelos, LS Di Prospero, MJ Yaffe, V Goel, E Ramsay, PL Chart, DEC Cole, et al. Comparison of breast magnetic resonance imaging, mammography, and ultrasound for surveillance of women at high risk for hereditary breast cancer. *Journal of Clinical Oncology*, 19(15):3524–3531, 2001.
- [127] Jun Xia, Muhammad R Chatni, Konstantin Maslov, Zijian Guo, Kun Wang, Mark Anastasio, and Lihong V Wang. Whole-body ring-shaped confocal photoacoustic computed tomography of small animals in vivo. *Journal of biomedical optics*, 17(5):0505061–0505063, 2012.
- [128] Minghua Xu and Lihong V Wang. Analytic explanation of spatial resolution related to bandwidth and detector aperture size in thermoacoustic or photoacoustic reconstruction. *Physical Review E*, 67(5):056605, 2003.
- [129] Minghua Xu and Lihong V Wang. Universal back-projection algorithm for photoacoustic computed tomography. *Physical Review E*, 71(1):016706, 2005.
- [130] Minghua Xu and Lihong V Wang. Photoacoustic imaging in biomedicine. *Review of scientific instruments*, 77(4):041101, 2006.
- [131] Yuan Xu, Lihong V Wang, Gaik Ambartsoumian, and Peter Kuchment. Reconstructions in limited-view thermoacoustic tomography. *Medical physics*, 31(4):724–733, 2004.
- [132] Kazuhiro Yamanaka, Takahide Terada, Takashi Maruoka, Yushi Tsubota, Wenjing Wu, and Ken-ichi Kawabata. Method for extracting microcalcifications with analysis of isotropy of scattered acoustic signals in ring-array transducer system. In *Ultrasonics Symposium (IUS), 2016 IEEE International*, pages 1–4. IEEE, 2016.

- [133] Diwu Yang, Da Xing, Sihua Yang, and Liangzhong Xiang. Fast full-view photoacoustic imaging by combined scanning with a linear transducer array. *Optics express*, 15(23):15566–15575, 2007.
- [134] Da-Kang Yao, Konstantin Maslov, Kirk K Shung, Qifa Zhou, and Lihong V Wang. In vivo label-free photoacoustic microscopy of cell nuclei by excitation of dna and rna. *Optics letters*, 35(24):4139–4141, 2010.
- [135] Junjie Yao, Chih-Hsien Huang, Lidai Wang, Joon-Mo Yang, Liang Gao, Konstantin I Maslov, Jun Zou, and Lihong V Wang. Wide-field fast-scanning photoacoustic microscopy based on a water-immersible mems scanning mirror. *Journal of biomedical optics*, 17(8):0805051–0805053, 2012.
- [136] Junjie Yao and Lihong V Wang. Photoacoustic tomography: fundamentals, advances and prospects. *Contrast media & molecular imaging*, 6(5):332–345, 2011.
- [137] Junjie Yao and Lihong V Wang. Photoacoustic microscopy. *Laser & photonics reviews*, 7(5):758–778, 2013.
- [138] Roger J. Zemp, Chulhong Kim, and Lihong V. Wang. Ultrasound-modulated optical tomography with intense acoustic bursts. *Appl. Opt.*, 46(10):1615–1623, Apr 2007.
- [139] Roger J Zemp, Alexander Sampaleanu, and Tyler Harrison. S-sequence encoded synthetic aperture b-scan ultrasound imaging. In *2013 IEEE International Ultrasonics Symposium (Ius)*, pages 593–595. IEEE, 2013.
- [140] Chi Zhang, Konstantin Maslov, and Lihong V Wang. Subwavelength-resolution label-free photoacoustic microscopy of optical absorption in vivo. *Optics letters*, 35(19):3195–3197, 2010.
- [141] G Zografos, D Koulocheri, P Liakou, M Sofras, S Hadjiagapis, M Orme, and V Marmarelis. Novel technology of multimodal ul-

trasound tomography detects breast lesions. *European radiology*, 23(3):673–683, 2013.

- [142] G Zografos, P Liakou, D Koulocheri, I Liovarou, M Sofras, S Hadjiagapis, M Orme, and V Marmarelis. Differentiation of birads-4 small breast lesions via multimodal ultrasound tomography. *European radiology*, 25(2):410–418, 2015.